

Electronic Theses and Dissertations, 2004-2019

2005

Discrete Wave Propagation In Quadratically Nonlinear Media

Robert Iwanow
University of Central Florida

 Part of the [Electromagnetics and Photonics Commons](#), and the [Optics Commons](#)
Find similar works at: <https://stars.library.ucf.edu/etd>
University of Central Florida Libraries <http://library.ucf.edu>

This Doctoral Dissertation (Open Access) is brought to you for free and open access by STARS. It has been accepted for inclusion in Electronic Theses and Dissertations, 2004-2019 by an authorized administrator of STARS. For more information, please contact STARS@ucf.edu.

STARS Citation

Iwanow, Robert, "Discrete Wave Propagation In Quadratically Nonlinear Media" (2005). *Electronic Theses and Dissertations, 2004-2019*. 338.
<https://stars.library.ucf.edu/etd/338>

**DISCRETE WAVE PROPAGATION
IN QUADRATICALLY NONLINEAR MEDIA**

by

ROBERT IWANOW
M.S. Technical University of Szczecin, 1997
M.S. University of Central Florida, 2001

A dissertation submitted in partial fulfillment of the requirements
for the degree of Doctor of Philosophy
in the College of Optics and Photonics
at the University of Central Florida
Orlando, Florida

Spring Term
2005

Major Professor: George I. Stegeman

© 2005 Robert Iwanow

ABSTRACT

Discrete models are used in describing various microscopic phenomena in many branches of science, ranging from biology through chemistry to physics. Arrays of evanescently coupled, equally spaced, identical waveguides are prime examples of optical structures in which discrete dynamics can be easily observed and investigated. As a result of discretization, these structures exhibit unique diffraction properties with no analogy in continuous systems. Recently nonlinear discrete optics has attracted a growing interest, triggered by the observation of discrete solitons in AlGaAs waveguide arrays reported by Eisenberg et al. in 1998. So far, the following experiments involved systems with third order nonlinearities.

In this work, an experimental investigation of discrete nonlinear wave propagation in a second order nonlinear medium is presented. This system deserves particular attention because the nonlinear process involves two or three components at different frequencies mutually locked by a quadratic nonlinearity, and new degrees of freedom enter the dynamical process.

In the first part of dissertation, observation of the discrete Talbot effect is reported. In contrast to continuous systems, where Talbot self-imaging effect occurs irrespective of the pattern period, in discrete configurations this process is only possible for a specific set of periodicities.

The major part of the dissertation is devoted to the investigation of soliton formation in lithium niobate waveguide arrays with a tunable cascaded quadratic nonlinearity. Soliton species with different topology (unstaggered – all channels in-phase, and staggered – neighboring

channels with a π relative phase difference) are identified in the same array. The stability of the discrete solitons and plane waves (modulational instability) are experimentally investigated.

In the last part of the dissertation, a phase-insensitive, ultrafast, all-optical spatial switching and frequency conversion device based on quadratic waveguide array is demonstrated. Spatial routing and wavelength conversion of milliwatt signals is achieved without pulse distortions.

Dedicated to my parents,
Jadwiga and Ryszard Iwanow

ACKNOWLEDGMENTS

I would not have been able to complete this thesis without the support of numerous people. In fact, the number is so great that I fear I may fail to recognize all who have contributed.

I consider myself very fortunate to work under the supervision of Professor George Stegeman. I have been given opportunity to conduct an independent research knowing that he was always around ready to help if I encountered any difficulties. His optimism and excitement for the work was very stimulating. I am indebted to Professor Roland Schiek for spending countless hours in the lab teaching me how to prepare and run experiments. I am also grateful to Professor Demetrios Christodoulides for invaluable discussions which influenced my understanding of physics. All of you changed my life but each in his own unique way.

I am grateful to my collaborators: Professor Falk Lederer and Dr. Thomas Pertsch for their theoretical support and Professor Wolfgang Sohler and Dr. Yoohong Min for fabrication excellent quality samples.

I would like to express my sincere appreciation to Professor Ewa Weinert-Rączka for introducing me to an exciting world of optics.

During the studies at University of Central Florida I had an opportunity to meet many friends who I will always remember: Bojan, Erdem, Ferenc, Fumiyo, Jim, Joachim, Ladislav, Sergey, Te-Yuan and Waleed.

And finally I would like to thank my family and particularly my parents – their unconditional support has been invaluable in my life and I believe it is going to continue.

TABLE OF CONTENTS

LIST OF FIGURES	ix
LIST OF TABLES	xvi
LIST OF ABBREVIATIONS	xvii
CHAPTER ONE: INTRODUCTION	1
CHAPTER TWO: THEORY OF DISCRETE QUADRATIC OPTICS	6
2.1. Physics of cascaded quadratic nonlinearity	6
2.2. Quasi phase-matching	13
2.3. Wave propagation in channel dielectric waveguides	14
2.4. Quadratically nonlinear directional coupler	18
2.5. Waveguide arrays	21
2.5.1. Linear properties of discrete arrays	24
2.5.2. Nonlinear properties and discrete quadratic solitons	27
CHAPTER THREE: SAMPLES	32
3.1. Introduction	32
3.2. Fabrication	33
3.3. Characterization	43
CHAPTER FOUR: EXPERIMENTAL SYSTEM	52
4.1. Sources	52
4.1.1. Tunable Agilent HP81680A CW diode laser	52
4.1.2. Burleigh FC-120 Color Center Laser	53

4.1.3. Fiber-based system.....	54
4.1.4. Ekspla PG501VIR OPG-OPA system	65
4.2. Power Measurements	66
4.2.1. CW and high repetition rate systems	66
4.2.2. Low repetition rate system.....	67
4.3. Cameras.....	67
CHAPTER FIVE: DISCRETE TALBOT EFFECT	69
5.1. Overview of Talbot effect in continuous media	69
5.2. Theory of discrete Talbot effect.....	73
5.3. Setup and experimental results	78
CHAPTER SIX: QUADRATIC SOLITONS.....	83
6.1. Introduction.....	83
6.2. Weakly localized solitons	84
6.3. Strongly localized solitons.....	94
CHAPTER SEVEN: MODULATION INSTABILITY	101
7.1. Introduction.....	102
7.2. Setup and experimental results	103
CHAPTER EIGHT: PARAMETRIC SWITCHING.....	107
8.1. Introduction.....	108
8.2. Setup and experimental results	111
CHAPTER NINE: CONCLUSIONS.....	117
LIST OF REFERENCES.....	120

LIST OF FIGURES

Figure 2.1 Schematic diagram showing the physical origin of the nonlinear phase shift due to cascading. Note that the regenerated FH is out of phase with the original FH so that the total FH is shifted in phase.....	10
Figure 2.2 Variation in the nonlinear phase shift $\Delta\phi^{\text{NL}}$ with propagation distance (left-hand-side) and input intensity (right-hand-side) for various phase-mismatches.....	11
Figure 2.3 Simple waveguide geometry under consideration.....	16
Figure 2.4 Nonlinear directional coupler geometry.....	19
Figure 2.5 Waveguide array geometry.....	22
Figure 2.6 Cross-sectional cut of the PPLN waveguide array sample used in the transverse y - z plane showing the channel index profile, and the overlapped FH ($\hat{E}_{FH}^0(y, z)$) fields and SH ($\hat{E}_{SH}^0(y, z)$) fields. Note the tight confinement of SH causing $C_{SH} \approx 0$	23
Figure 2.7 Angular dispersion in the coupled array induced propagation wavevector, $\Delta k_x = k_x - \beta$ vs. k_y in a waveguide array.....	26
Figure 2.8 Discrete diffraction pattern for single channel excitation.....	27
Figure 2.9 FH envelope field distribution for different kinds of bright solitons.....	30
Figure 3.1 Fabrication steps to obtain a periodically poled channel waveguide.....	33
Figure 3.2 Geometry of the sample relative to the crystal axes.....	35
Figure 3.3 Typical refractive index distribution for a Ti in-diffused channel waveguide.....	35
Figure 3.4 Calculated FH fundamental TM_{00} mode intensity.....	36

Figure 3.5 Calculated SH TM mode intensities: a) TM_{00} , b) TM_{01} , c) TM_{10} , d) TM_{02} .	37
Figure 3.6 Wavelengths for phase-matching between the FH TM_{00} and different SH TM modes for a QPM grating with $\Lambda = 16.751 \mu\text{m}$ (at room temperature) for $T_0 = 220^\circ\text{C}$.	39
Figure 3.7 Phase-mismatch $\Delta\beta L$ between the FH and the SH TM_{00} modes for a QPM grating with $\Lambda = 16.751 \mu\text{m}$ (at room temperature) versus temperature and wavelength for a 5 cm long sample.	40
Figure 3.8 Calculated coupling length versus channel-to-channel separation.	42
Figure 3.9 Typical sample layout.	44
Figure 3.10 The measured discrete diffraction pattern (solid line) for array # 2 with coupling length $L_c = 15.74 \text{ mm}$ in the sample Pb381z for comparison with the best theoretical fit from which the coupling constants were obtained.	45
Figure 3.11 Comparison of the measured coupling lengths of the Pb344z and Pb381z samples with calculated ones based on design.	46
Figure 3.12 Measured coupling constants (on the left) and coupling lengths (on the right) for the Pb381z sample. Each curve represents one array on the sample.	46
Figure 3.13 Measured dispersion relations for the lowest band for array # 2 in the sample Pb381z with a coupling length $L_c = 15.74 \text{ mm}$.	47
Figure 3.14 Dependence of the SH power versus the FH input wavelength and tilt of FH input beam for Pb344z sample.	48
Figure 3.15 SH tuning curves for the edge witness channels for the two best samples: Pb344z and Pb381z at temperature of $T = 195^\circ\text{C}$.	49

Figure 3.16 Geometry of the spatial resolved SHG experiment (on the left) and result of two measurements taken for two diffractionless angles ($-\pi/2$ and $\pi/2$) for the Pb381z sample at room temperature.	50
Figure 4.1 Large core Erbium doped fiber amplifier characterization setup.	55
Figure 4.2 Spectral broadening at the output of the amplifier due to self phase modulation: before (on the left) and after (on the right) shortening the output fiber as a function of pumping diode current. 2.75 A corresponds to 2.5 kW optical peak power at the output.	56
Figure 4.3 Application of Chirped Pulse Amplification technique to the fiber based system.	57
Figure 4.4 Characterization of reflection of chirped fiber Bragg grating: setup (on the left) and results for inputs into both ends (on the right).	57
Figure 4.5 Second order dispersion characterization setup.	58
Figure 4.6 Input and output spectra for an initially negatively chirped pulse.	59
Figure 4.7 Compressor layout based on the Spectra-Physics design with the beam output at various positions shown.	59
Figure 4.8 Efficiency of coupling to the first diffracted order as a function of the angular deviation from the Littrow angle.	60
Figure 4.9 SHG frequency resolved optical gating setup used to characterize pulses from the fiber based system.	62
Figure 4.10 SHG frequency resolved optical gating traces for two different settings of pumping currents of booster stage diode: $I_{d2} = 1.0$ A on the left and $I_{d2} = 5.0$ A on the right.	62
Figure 4.11 The retrieved pulse amplitudes and phases for two different settings of the diode's pumping current (booster stage diode): $I_{d2} = 1.0$ A on the left and $I_{d2} = 5.0$ A on the right.	63

Figure 4.12 Comparison of measured (green) with calculated from the retrieved pulses (blue) autocorrelation (first row) and power spectrum (second row) for two different settings of the pumping currents of the booster stage diode $I_{d2} = 1.0$ A (on the left) and $I_{d2} = 5.0$ A (on the right).....	64
Figure 5.1 One-dimensional fractional Talbot patterns for: a) $x = 0$ or $2x_T$, b) $x = x_T/4$ or $7/4x_T$, c) $x = x_T/2$ or $3/2x_T$, d) $x = 3/4x_T$ or $5/4x_T$, e) $x = x_T$	72
Figure 5.2 Talbot intensity "carpets" for input field pattern $[1, 0, 1, 0, \dots]$ and different Bloch momentum ϕ : a) 0, b) $\pi/4$, c) $\pi/2$	77
Figure 5.3 Talbot intensity "carpets" for different in-phase input field patterns: a) $[1, 0, 0, 1, 0, 0, \dots]$ and b) $[1, 0, 0, 0, 1, 0, 0, 0, \dots]$	78
Figure 5.4 Experimental setup.....	79
Figure 5.5 Experimentally observed Talbot revivals for the input field pattern $[1, 0, 1, 0, \dots]$ and different Bloch momentum ϕ : a) 0, b) $\pi/4$, c) $\pi/2$.a).....	81
Figure 5.6 Experimentally observed Talbot revivals for in-phase input field patterns: a) $[1, 0, 0, 1, 0, 0, \dots]$ and b) $[1, 0, 0, 0, 1, 0, 0, 0, \dots]$ excitations.....	82
Figure 6.1 Experimental setup for the excitation of weakly localized solitons.....	85
Figure 6.2 The FH energy distribution output from the array as a function of the input peak power for an array with the coupling length $L_c = 9.53$ mm for a positive wavevector mismatch.....	86
Figure 6.3 Spatial pulsed energy profile of the two nonlinearly coupled frequency components of an unstaggered odd discrete soliton ($\Delta\beta L = 140\pi$, $L_c = 15.74$ mm, FH input peak power of 500 W). Dotted lines and open circles show the low power FH diffracted beam, solid lines and circles show the soliton. Circles identify theoretical data.....	87

Figure 6.4 Soliton peak power versus $\Delta\beta L$ for arrays with different coupling lengths L_c 88

Figure 6.5 (a) Simulated evolution of the transverse energy (time integrated) spatial profile of beams excited by a FH input ($\Delta\beta L = 140\pi$, $L_c = 15.74$ mm, FH input peak power of 442 W). (b) Spatio-temporal output distribution of the simulation in (a)..... 89

Figure 6.6 FH output energy distribution as a function of input peak power for an array with the coupling length $L_c = 9.53$ mm, negative wavevector mismatch and unstaggered excitation. 90

Figure 6.7 FH output energy distribution as a function of input peak power for an array with the coupling length $L_c = 15.74$ mm, for a negative wavevector mismatch and for staggered excitation..... 91

Figure 6.8 Nonlinearly reinforced beam broadening for in-phase excitation for $\Delta\beta L = -50\pi$, $L_c = 12.16$ mm, FH input peak power of 870 kW) (on the left); Staggered soliton profile ($\Delta\beta L = -16\pi$, $L_c = 15.74$ mm, input peak power of 150 W) (on the right). Solid and empty circles identify the high and low power theoretical data, respectively..... 92

Figure 6.9 Time sequence of FH output energies, sampled at intervals of 200 ms, from waveguides in the soliton center as indicated in the insets ($L_c = 15.7$ mm, $\Delta\beta L = 140\pi$). (a) Stable output for odd soliton excitation. b) Unstable output for even excitation. 93

Figure 6.10 Numerical simulations for CW propagation of the FH (on the left) and SH (on the right) with input conditions of $P_{FH} = 560$ W, $P_{SH} = 0$ W, and $\Delta\beta L = 106\pi$. Only the FH is input. 95

Figure 6.11 Numerical simulations of the CW propagation in an array of the FH (on the left) and SH (on the right) with input conditions associated with an in-phase eigenmode of an isolated channel. Here $P_{FH} = 525$ W, $P_{SH} = 35$ W, and $\Delta\beta L = 106\pi$ 96

Figure 6.12 Numerical simulations of the array output versus relative phase difference between FH (on the left) and SH seed (on the right) pulses, assumed to be 7.65 ps. Input powers for FH and SH are 400 W and 7 W, mismatch $\Delta\beta L = 90\pi$ 97

Figure 6.13 Experimental setup for the excitation of strongly localized discrete quadratic solitons. 98

Figure 6.14 Experimental FH (on the left side) and SH (on the right side) output power distribution vs. input relative phase difference, for the following input conditions: $P_{FH} = 400$ W, $P_{SH} = 7$ W, $\Delta\beta L = 90\pi$ 99

Figure 7.1 Experimental setup. 104

Figure 7.2 Distribution across the array of the fundamental beam output power from the array for normal incidence as a function of the input pulse energy: positive wavevector mismatch $\Delta\beta L = 170\pi$ (on the left) and negative wavevector mismatch $\Delta\beta L = -40\pi$ (on the right). Note the different behavior of the two defect-created “hot spots” at the positions 200 and 250. 105

Figure 7.3 Distribution across the array of the fundamental beam output power from the array as a function of the relative input phase between adjacent channels: positive wavevector mismatch $\Delta\beta L = 170\pi$ (on the left) and negative wavevector mismatch $\Delta\beta L = -40\pi$ (on the right). The input pulse energy was 0.27 μ J. 106

Figure 8.1 Geometry of the all-optical switching and frequency conversion scheme. 109

Figure 8.2 Simulated propagation of the signal and idler beams for the all-optical switching and frequency conversion scheme.....	110
Figure 8.3 Experimental layout.....	112
Figure 8.4 Geometry of the experiment (on the left) and spatial-spectral scan of the output of a waveguide array after parametric interaction of a signal beam ($\lambda_s = 1550.7$ nm, $P_s = 13$ mW, input centered at guide 12) and a control beam ($\lambda_p = 1550.7$ nm, $P_{peak} = 10.7$ W, input centered at guide 1) which generates an idler ($\lambda_i = 1546.7$ nm).....	113
Figure 8.5 a) Output spectral density from waveguide 15 for a control input with $P_{peak} = 3.8$ (red) and 10.7 W (blue), $P_s = 19$ mW. The control spectrum is also shown (black). b) Peak power of the idler ($\lambda_i = 1546.7$ nm) at the output for $P_{peak} = 10.7$ W, $P_s = 19$ mW. Dashed lines and circles show theory.....	115
Figure 8.6 a) Spatial output distribution of the deflected idler for different positions of the control beam. b) Spectral density of the deflected signal and idler in waveguide 15 for a number of different signal wavelengths, $P_{peak} = 10.7$ W, $P_s = 19$ mW.....	116

LIST OF TABLES

Table 3.1 Effective mode indices at $T_0 = 220^\circ\text{C}$ for FH and SH modes.....	38
Table 3.2 Taylor series expansion coefficients for FH and SH TM_{00} modes for $\lambda_0 = 1550$ nm for the FH and $\lambda_0 = 775$ nm for the SH at $T_0 = 220^\circ\text{C}$	38
Table 3.3 Coupling integrals $K^{(2)}$ and SHG efficiencies for different FH-SH resonances for a 5 cm long sample.	41
Table 3.4 Summary of the experimentally measured basic parameters for the Pb344z sample...	51
Table 3.5 Summary of the experimentally measured basic parameters for the Pb381z sample...	51
Table 4.1 Main parameters of HP 81680A diode laser.....	53
Table 4.2 Main parameters of Burleigh FC-120 color center laser.	53
Table 4.3 Main parameters of the Pritel picosecond fiber laser.	61
Table 4.4 Main parameters of fiber based system.	64
Table 4.5 Main parameters for the Ekspla OPG-OPA system.....	65
Table 7.1 Conditions for existence of the modulational instability in the quadratic discrete system.	106

LIST OF ABBREVIATIONS

CCL	color center laser
CFBG	chirped fiber Bragg grating
CME	coupled mode equations
CMT	coupled mode theory
CPA	chirped pulse amplification
CW	continuous wave
EDFA	Erbium doped fiber amplifier
Er	Erbium
FH	fundamental harmonic
FWHM	full-width at half maximum
Ge	Germanium
GVD	group velocity dispersion
KTP	potassium titanyl phosphate
MI	modulation instability
MO	microscope objective
PM	phase-matching
PPKTP	periodically poled potassium titanyl phosphate
PPLN	periodically poled lithium niobate
QPM	quasi phase-matching
Si	Silicon

SH	second harmonic
SHG	second harmonic generation
SPM	self phase modulation
SVEA	slowly varying amplitude approximation
Ti	Titanium

CHAPTER ONE: INTRODUCTION

Stanisław Ulam, the celebrated Polish mathematician and godfather of the field now known as nonlinear science, famously remarked that using term “nonlinear science” was like “calling the bulk of zoology the study of non-elephants”. He meant that linear processes are the exception rather than the rule; that most phenomena are inherently nonlinear; and that the effects of nonlinearity are apparent everywhere in nature, from the synchronized flashing of fireflies through clear-air turbulence to tornadoes and tsunamis [1]. Therefore experimental investigations of nonlinear processes, which at first look seem to be very academic and not applicable to anything real, are attracting growing attention.

On the other hand, classical physics, developed over thousands of years, treats phenomena occurring in nature in a continuous manner. However it can only represent average behavior of many microscopic interactions between smaller entities, i.e. electrons, molecules, organized in larger scale structures. The dynamics of the structures can be described using discrete models, under the assumption that energy is localized in discrete points in space and the forces governing the interactions between the entities are dissociated from them. The investigation of the interactions is a hot topic currently in physics. The year 1939 witnessed the origin of the study of dynamics in discrete systems when Frenkel and Kontorova [2] used a discrete model to describe the propagation of dislocations inside a crystal. Fifteen years later Fermi, Pasta and Ulam [3] reported, in their seminal paper, the observation of recurrence phenomenon in a nonlinear lattice. Discrete nonlinear models were used to explain vibration in

crystals [4, 5] and the dynamics of crystals exhibiting structural phase transitions [6]. Within the last three decades nonlinear localization phenomena in lattices has attracted a steadily growing interest, and their existence has been predicted in a wide range of systems (in molecular chains [7], atomic lattices [8, 9], hydrocarbon structures [10, 11], Josephson-junction ladders [12, 13] and electrical transmission lines [14] to mention just a few). Quite recently, nonlinearly self-trapped states in arrays of Bose-Einstein condensates were predicted using a discrete Schrödinger model and observed experimentally [15, 16]. The diversity of these phenomena and their richness compared to those in continuous systems stems essentially from the mutual interplay of the peculiar transport properties (diffusion, diffraction, dispersion, tunneling) coupled with the specific nonlinearity of the lattices. In particular, the differences to continuous systems are significant if the lattice topology is such that the excitation dynamics may be described by the linear interaction of many nonlinear, but fairly simple unit cells. In this particular case the lattice is frequently termed a discrete system. Consequently, the respective localized structures are called discrete breathers or discrete solitons.

Because of the geometrical dimensions involved, the approaches to experimental observations in the above mentioned cases are limited. However it is often possible to develop discrete models of a macroscopic phenomenon. In optics, weakly coupled waveguide arrays [17], chains of coupled microresonators [18] and photonic crystals [19] are prime examples of structures where discrete dynamics can be observed and investigated. The linear properties of one-dimensional waveguide chains were first theoretically addressed in 1965 by Jones [20] and experimentally verified a few years later [17]. The idea that light could trap itself and form a soliton due to the Kerr nonlinear effect in optical waveguide arrays was suggested by Christodoulides and Joseph in 1988 [21]. Their work was followed by theoretical studies of

discrete optical systems with other kinds of nonlinearities, i.e. quadratic [22, 23], photorefractive [24] and recently dissipative systems [25, 26]. To date the experimental studies are restricted to frequency degenerate effects in media with Kerr [27, 28], photorefractive [29, 30] and orientational nonlinearities [31] where various discrete solitons associated with a diversity of linear diffraction properties have been observed. But because the very interplay between these linear transport phenomena and the nonlinearity govern the localization process, it is challenging to study localization phenomena for other more diverse nonlinearities. In this respect quadratic nonlinearities deserve particular attention because the interaction process involves two or three components at different frequencies and new degrees of freedom enter the dynamical process.

The main goal of the work presented in this dissertation was to experimentally verify theoretical predictions about discrete soliton formation, properties and stability (namely conditions for existence of modulation instability) in a quadratically nonlinear medium in degenerate configuration. Two additional experiments were performed, the Talbot effect illustrating a discrete analog of the effect occurring in continuous media and parametric switching utilizing the linear and nonlinear properties of the quadratic waveguide arrays.

In Chapter 2 the theoretical basics of the physical phenomena necessary for understanding wave propagation in discrete quadratic medium are presented. The governing equations are derived based on coupled mode theory. The linear and nonlinear properties of quadratic arrays are discussed in detail.

Chapter 3 is dedicated to the description of the design, fabrication and characterization of the lithium niobate samples used in the experiments presented in this dissertation. Based on group experience with lithium niobate over the last 15 years, the sample design methodology is described in detail. New linear and nonlinear methods of characterization of the samples, which

were developed in the lab during the work on the project, are presented. Results of characterization studies are compared with simulations based on the design.

The apparatus used in the experiments is presented in Chapter 4. Most of the chapter is devoted to a fiber-based high power laser system build especially for the project to match the requirements set by the samples.

The Talbot effect being a direct result of Fresnel diffraction belongs to the most basic phenomena in optics. So far, it has only been investigated in continuous systems either in the space or time domain. Because of the unique properties of the diffraction relations in discrete arrays, the question arises if this fundamental process exists in these systems. In Chapter 5 the first observation of the discrete Talbot effect is presented together with analytical analysis and discussion [32].

In Chapter 6 the existence of staggered and unstaggered quadratic discrete solitons is demonstrated. They are found to exist only for certain combinations of diffraction and nonlinearity. Two different cases are considered: weakly localized [33], where 4-5 channels are excited and strongly localized [34] where most of the power is guided in one channel. The quadratic nature of the solitons is confirmed by the soliton power dependence on the wavevector mismatch in the second harmonic process. Nonlinearly enhanced beam broadening is demonstrated for complimentary combinations of diffraction and nonlinearity.

Modulational instability refers to the instability of a plane wave propagating in a nonlinear medium in the presence of noise perturbations. If the perturbations grow exponentially on propagation, the wave is called modulationally unstable. In Chapter 7 the conditions for stable propagation of wide beams in quadratic waveguide arrays is investigated [35].

In Chapter 8 the demonstration of a phase-insensitive, ultrafast, all-optical switching and frequency conversion scheme based on quadratically nonlinear arrays is presented [36, 37]. Routing of milliwatt signals with wavelengths in the communication band is achieved without pulse distortions by parametric interaction.

In Chapter 9 major contributions of the thesis are summarized.

CHAPTER TWO: THEORY OF DISCRETE QUADRATIC OPTICS

2.1. Physics of cascaded quadratic nonlinearity

When light passes through matter, it interacts with individual atoms or molecules of the material and induces dipole moments. The average of these dipole moments is called polarization. When the beam intensity is small, the response of atoms or molecules is linear to the applied optical field. However if the electric field strength of the incident light is comparable with the electric fields binding electrons to a nucleus, the response is no longer linear. Mathematically, the polarization in this case can be described as a power series in the electric field as

$$\vec{P} = \epsilon_0 \left(\vec{\chi}^{(1)} \vec{E} + \vec{\chi}^{(2)} \vec{E} \vec{E} + \vec{\chi}^{(3)} \vec{E} \vec{E} \vec{E} + \dots \right) \quad (2.1)$$

where \vec{P} and \vec{E} are the polarization and the total electric field respectively [38]. The terms associated with the first, second and third order susceptibilities $\vec{\chi}^{(1)}$, $\vec{\chi}^{(2)}$ and $\vec{\chi}^{(3)}$ are the linear, second and third order contributions to the total polarization, respectively. In general the susceptibilities are tensors whose rank increases as the order of the nonlinear interaction increases. Molecular, amorphous and crystal structures can be classified into two broad categories: those with a center of symmetry (centrosymmetric) and those without (non-centrosymmetric) [39]. Because of symmetry reasons, quadratic terms can exist only in a non-centrosymmetric medium. On the other hand, the third order term (cubic nonlinearity) has no

such limitations and is always non-zero. Because the strength of the nonlinear polarization induced usually decreases as the order increases, typically for a non-centrosymmetric material the second order response is much stronger than the third order one. As most of the work presented in this thesis was done close to a phase-matching condition for second harmonic generation (SHG), the higher order terms (starting from the cubic one) will be neglected in the derivations presented in this chapter.

When light propagates through matter, the evolution of the electric field of the light can be described by a wave equation which can be derived from Maxwell's equations [40].

$$\nabla^2 \vec{E} - \frac{n^2}{c^2} \frac{\partial^2 \vec{E}}{\partial t^2} = \mu_0 \frac{\partial^2 \vec{P}^{NL}}{\partial t^2} \quad (2.2)$$

where \vec{P}^{NL} is the second order polarization. In more detail, the second order polarization can be expressed as,

$$P_i = \epsilon_0 \sum_{j,k} \chi_{ijk}^{(2)} E_j E_k. \quad (2.3)$$

In general a second order process involves three beams coupled by the susceptibility $\chi^{(2)}$ which is a third rank tensor. Therefore the resulting nonlinear polarization depends not only on the magnitude of the incident fields but also on their polarization directions. Although the discussion can be easily extended to other parametric processes such as sum-frequency generation etc., in the derivations in this chapter the focus will be put on the SHG process that involves two waves – a fundamental (FH) at frequency ω and a second harmonic (SH) at frequency 2ω . This typically requires either Type I or QPM phase-matching.

First, the slowly varying envelope approximation (SVEA) for plane waves is applied,

$$\begin{aligned}
E_{\omega}(x, t) &= \frac{1}{2} A_{\omega}(x) e^{i(k_{\omega}x - \omega t)} + c.c. \\
E_{2\omega}(x, t) &= \frac{1}{2} A_{2\omega}(x) e^{i(k_{2\omega}x - 2\omega t)} + c.c.
\end{aligned} \tag{2.4}$$

which assumes that the propagating field envelopes $A_{\omega}(x)$ and $A_{2\omega}(x)$ change slowly with propagation distance x . A_{ω} and $A_{2\omega}$ are the slowly varying amplitudes of the plane wave fields at the FH and SH frequencies. The appropriate nonlinear polarizations which generate fields at 2ω and ω respectively are

$$\begin{aligned}
P_{2\omega} &= \varepsilon_0 d_{eff} A_{\omega}^2 \\
P_{\omega} &= 2\varepsilon_0 d_{eff} A_{2\omega} A_{\omega}^*
\end{aligned} \tag{2.5}$$

and the effective nonlinear coefficient d_{eff} is defined as [41]

$$d_{eff} = \frac{1}{2} \hat{e}(2\omega) \times \vec{\chi}^{(2)}(2\omega; \omega, \omega) \times \hat{e}(\omega) \hat{e}(\omega). \tag{2.6}$$

Inserting equation (2.4) into (2.2) and assuming slow changes of amplitude over a wavelength during propagation

$$\left| \frac{d^2 A}{dx^2} \right| \ll k \left| \frac{dA}{dx} \right| \tag{2.7}$$

gives the well-known coupled mode equations.

$$\begin{aligned}
\frac{dA_{\omega}}{dx} &= i \frac{\omega d_{eff}}{n_{\omega} c} A_{2\omega} A_{\omega}^* e^{-i\Delta k x} \\
\frac{dA_{2\omega}}{dx} &= i \frac{\omega d_{eff}}{n_{2\omega} c} A_{\omega}^2 e^{i\Delta k x}.
\end{aligned} \tag{2.8}$$

These equations describe the change in the amplitude and phase of the FH and SH fields along the propagation co-ordinate x . The first equation describes down-conversion (by which the FH is generated), and the second up-conversion (by which the SH is generated). The wavevector mismatch Δk is defined as

$$\Delta k = 2k_{\omega} - k_{2\omega} = \frac{4\pi}{\lambda}(n_{\omega} - n_{2\omega}) \quad (2.9)$$

and depends on wavelength and refractive index, and therefore on material temperature, polarization and direction of propagation in the material. It is important to note that Kleinman's symmetry [39] of the susceptibility tensor $\vec{\chi}^{(2)}$ was used to derive the expression in (2.8).

The wavevector mismatch Δk plays a crucial role in any second order nonlinear process. For a non-zero wavevector mismatch, the SH which is generated earlier in the sample will be out of phase with that generated at a longer distance from the input. Due to this destructive interference the SH will be converted back to the fundamental. The distance after which the relative phase between the FH and SH fields changes by π is defined as the coherence length L_{coh} , and is given by the formula

$$L_{coh} = \frac{\pi}{\Delta k} = \frac{\lambda}{4(n_{\omega} - n_{2\omega})}. \quad (2.10)$$

After propagation of two coherence lengths the FH is fully restored and SH starts to build again.

It is possible to derive an analytical solution for SHG in the so-called low depletion regime when the amount of generated SH is much smaller than the FH. Mathematically, negligible contribution of down-conversion is assumed. In this case, the generated SH intensity is given by

$$I_{2\omega}(\Delta k, x) = \frac{2\omega^2 d_{eff}^2}{n_{2\omega} n_{\omega}^2 c^3 \epsilon_0} x^2 I_{\omega}^2 \text{Sinc}^2\left(\frac{\Delta k x}{2}\right). \quad (2.11)$$

Therefore, if the wavevector mismatch Δk is zero the intensity of the generated SH grows quadratically with the propagation distance x . For the oscillatory behavior ($\Delta k \neq 0$), the larger Δk , the smaller the period of the power oscillations and the smaller the peak SH power reached.

Although $\chi^{(2)}$ processes are normally associated with frequency conversion, it turns out that nonlinear (cascading) phase shifts also occur. The physics of the cascaded second order nonlinearity is rooted in the second harmonic generation process itself. The simple explanation of how the FH wave can obtain a nonlinear phase shift during the second order process is shown in Figure 2.1.

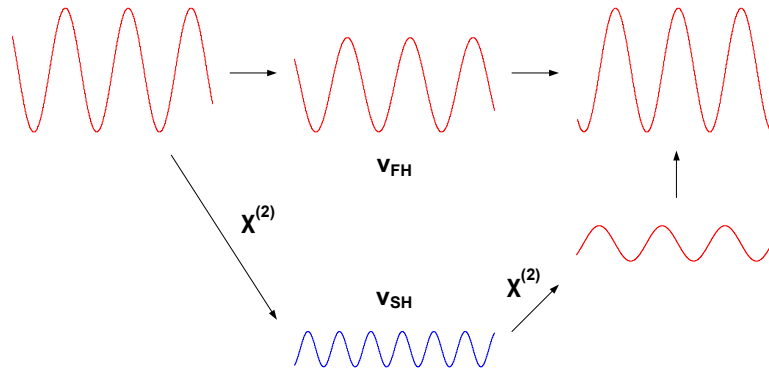


Figure 2.1 Schematic diagram showing the physical origin of the nonlinear phase shift due to cascading. Note that the regenerated FH is out of phase with the original FH so that the total FH is shifted in phase.

When an intense FH beam propagates through a quadratically nonlinear medium, part of it is always converted to SH. If there is a finite wavevector mismatch Δk , the SH so generated will also travel in the medium, but with a phase velocity v_{SH} different to that of the FH, v_{FH} . After some distance, typically of order of the coherence length L_{coh} , the SH will be down converted back to the FH. Because of the phase velocity difference between the two waves, the returning FH wave has a different phase from the original FH beam that was not converted to SH. The phase shift from the down-converted FH beam changes the overall phase of the FH. As a result, the more of the SH that is generated, the larger the net FH phase shift that can be achieved, i.e. it

is nonlinear phase shift and the process is known as the cascaded nonlinearity. Therefore a good material for SHG is also a good candidate for the cascaded nonlinearity. It is important to note that the cascading nonlinearity is a non-local process. Even though SHG itself is a local process, one should remember that to gain a phase shift requires some propagation distance.

The variation in the nonlinear phase shift with propagation distance and input FH intensity is now well-known and understood [42]. The cascaded phase shift increases with propagation distance in a stair-case fashion as shown in Figure 2.2a. Note that for large enough phase-mismatch ($|\Delta kL| > \pi$ where L is the sample length), the nonlinear phase shift becomes approximately linear with distance.

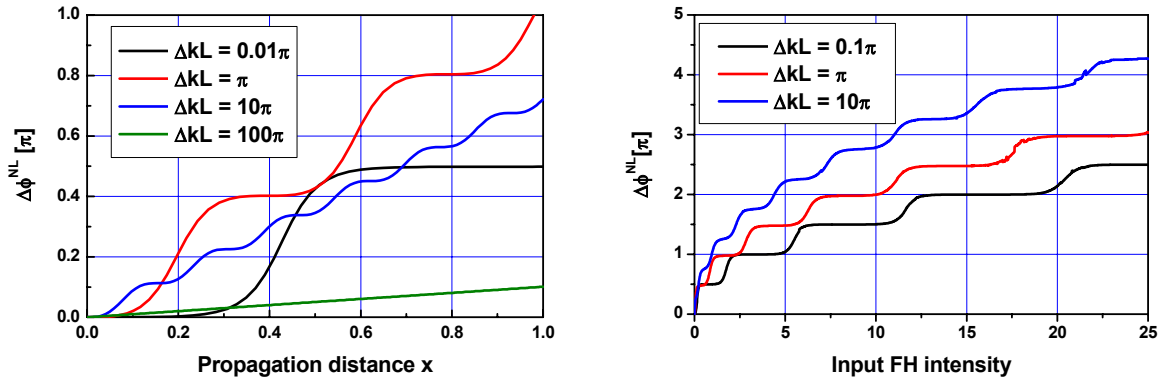


Figure 2.2 Variation in the nonlinear phase shift $\Delta\phi^{NL}$ with propagation distance (left-hand-side) and input intensity (right-hand-side) for various phase-mismatches.

Furthermore, for small intensities, $\Delta\phi^{NL}$ is linear with input intensity but becomes sub-linear when the phase shifts exceeds π because its origin is due to $\chi^{(2)}$ and not $\chi^{(3)}$ for which the nonlinear phase shift remains linear with intensity [42].

The regions of linear response correspond to small or negligible fundamental depletion during propagation. In this limit it is possible to obtain a simple analytical formula for the effective cascading n_2, n_{2eff} , where $\Delta n = n_2 |A_\omega|^2$ where n_2 is the nonlinear intensity dependent index coefficient associated with $\chi^{(3)}(-\omega, \omega, -\omega, \omega)$. If it is assumed that there is no depletion in the FH beam, the second equation in (2.8) can be integrated directly resulting in

$$A_{2\omega} = -\frac{\omega d_{eff} A_\omega^2}{n_{2\omega} c} \frac{e^{-i\Delta kx}}{\Delta k} + \frac{\omega d_{eff} A_\omega^2}{n_{2\omega} c} \frac{1}{\Delta k} \quad (2.12)$$

which can be inserted into the first equation in (2.8) giving

$$\frac{dA_\omega}{dx} = i \frac{\omega^2 d_{eff}^2}{n_\omega n_{2\omega} c^2} \frac{e^{i\Delta kx} - 1}{\Delta k} |A_\omega|^2 A_\omega. \quad (2.13)$$

By comparing this equation with the equivalent equation for a third order nonlinear process [43] gives an expression for an effective nonlinear refractive index coefficient n_{2eff} due to cascading as

$$n_{2eff} = \frac{2\omega d_{eff}^2}{n_{2\omega}^2 n_\omega c^2 \varepsilon_0 \Delta k} [1 - \cos(\Delta kx)] \quad (2.14)$$

For large Δkx , $[1 - \cos(\Delta kx)]$ averages to 1 and a space averaged \bar{n}_{2eff} can be written as

$$\bar{n}_{2eff} = \frac{2\omega d_{eff}^2}{n_{2\omega}^2 n_\omega c^2 \varepsilon_0 \Delta k}. \quad (2.15)$$

It is important to note that in contrast to the Kerr nonlinearity where n_2 is strictly a material constant, the cascading induced \bar{n}_{2eff} depends also on the wavevector mismatch. Thus it is possible to control both the strength and the sign of the effective nonlinearity by varying Δk . Therefore, if one operates far from the phase-matching (\bar{n}_{2eff} was derived under assumption of low FH depletion) the system behaves like a Kerr medium with a tunable nonlinear coefficient.

2.2. Quasi phase-matching

As discussed in detail in the previous section, phase-matching is a very important variable in quadratic nonlinear processes. Because of a material's refractive index dispersion with wavelength, phase-matching cannot be achieved for two interacting co-polarized waves. Birefringent phase-matching [41, 44] is a commonly used approach, where the effective indices of the interacting waves having different polarizations in a birefringent medium can result in $\Delta k = 0$ at some well-defined wavelength. However this approach is very limited in the range of potentially phase-matchable wavelengths.

Yet another phase-matching option is a very powerful technique called quasi-phase-matching (QPM) whereby materials can be engineered to phase-match any parametric process involving frequencies for which the material is transparent. The technique was first suggested in 1962 [45], at the time of the initial discovery of SHG. However because of fabrication problems, the method was the first realized efficiently in 1980s [46]. This method involves reversal of the sign of the nonlinear coefficient with propagation distance every time the accumulated phase difference reaches π . Hence the period of the QPM reversal grating Λ is double the coherence length L_{coh} . The QPM sign reversal at each multiple of L_{coh} prevents down conversion and results in continuous SH grow. However, because the growth occurs under conditions of phase-mismatch $-\pi/2 \leq \Delta kx \leq \pi/2$, the overall efficiency is less than for a perfectly phase-matched process with the same value of material nonlinearity. It is also important to note that this approach allows the FH and SH waves to be co-polarized so that diagonal elements of the susceptibility tensor, which are frequently the largest, can be used.

The periodic variation of the nonlinear coefficient produced by the QPM grating can be represented by the following Fourier series [46, 47]

$$g(x) = \sum_{m=-\infty}^{\infty} G_m \exp(iK_m x) \quad (2.16)$$

where the wavevector of the m -th spatial harmonic is given by

$$K_m = \frac{2\pi m}{\Lambda} \quad (2.17)$$

and the Fourier amplitude for a square wave of duty cycle D is

$$G_m = \frac{2}{m\pi} \sin(m\pi D) \quad (2.18)$$

The effective nonlinear coefficient is given then by

$$d'_{eff} = d_{eff} G_m \quad (2.19)$$

For a first order ($m = 1$) QPM grating, the optimum duty cycle is $D = 50\%$, such that

$$d'_{eff} = \frac{2d_{eff}}{\pi} \quad (2.20)$$

The effective nonlinear second order susceptibility is reduced by factor of $2/\pi$. In this case, the modified wavevector mismatch becomes

$$\Delta k' = \Delta k - K_1 = 2k_{\omega} - k_{2\omega} + \frac{2\pi}{\Lambda}. \quad (2.21)$$

For QPM, $\Delta k'$ replaces Δk in equations (2.8) to (2.15).

2.3. Wave propagation in channel dielectric waveguides

It was shown in equation (2.11) that the larger the fundamental intensity, the more efficient the conversion to SH becomes. Since intensity is power per unit area, the smaller the beam cross-sectional area, the more efficient the SH generation. The confinement of an optical beam inside a dielectric waveguide to dimensions of the order of the wavelength of light is possible due to a combination of total internal reflection and constructive interference. This

can be achieved by an index difference between the guiding, high index region and its lower index surroundings. Using such a waveguide allows the light to remain confined without diffraction, hence providing high intensities for long propagation distances, optimum conditions for highly efficient nonlinear interactions. Since all of the experiments described in this dissertation were performed in waveguides, in this section the basic properties of channel waveguide will be reviewed and the well-known coupled mode equations governing the evolution of 2D guided waves in a quadratically nonlinear medium derived. For a detailed derivation see reference [48].

Consider the simple embedded channel geometry, shown in Figure 2.3, where a transverse refractive index profile

$$n(y, z) = \sqrt{\varepsilon(y, z)} \quad (2.22)$$

is independent of the x (propagation) coordinate. This structure has modal solutions (eigenvalues) $\hat{E}_m(y, z)$, which can be found by solving Maxwell's equations [40]

$$\begin{aligned} \nabla \times \vec{E} &= -\mu_0 \frac{\partial \vec{H}}{\partial t} \\ \nabla \times \vec{H} &= \varepsilon \frac{\partial \vec{E}}{\partial t} \\ \nabla \cdot \varepsilon \vec{E} &= 0 \\ \nabla \cdot \mu_0 \vec{H} &= 0 \end{aligned} \quad (2.23)$$

where the dielectric media are assumed to be non-magnetic materials, i.e. $\mu_r = 1$. Here the parameter m which describes the mode is in fact a combination of two integers p and q usually written as (p, q) with each identifying the number of zeros in the field distribution across the transverse (y, z) dimensions of the waveguide. For example, $(0, 1)$ would indicate no field zeros in the y -dimension and one in the z -dimension.

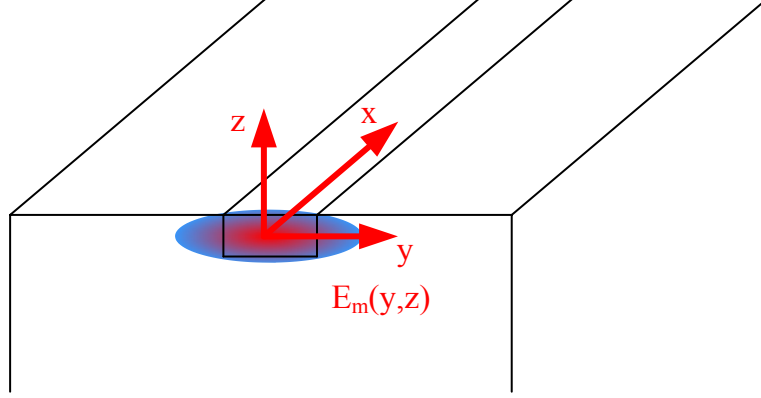


Figure 2.3 Simple waveguide geometry under consideration.

Propagating solutions to Maxwell's equations are assumed to take the form

$$\begin{aligned}\vec{E} &= \frac{1}{2} \hat{E}_m(y, z) e^{i(\beta^m x - \omega t)} + c.c. \\ \vec{H} &= \frac{1}{2} \hat{H}_m(y, z) e^{i(\beta^m x - \omega t)} + c.c.\end{aligned}\quad (2.24)$$

where \hat{E}_m and \hat{H}_m are the electric and magnetic field distributions for the m -th (p , q -th) mode and β^m is the corresponding modal wavevector. Therefore, Maxwell's equations in the frequency domain can be written in form

$$\begin{aligned}\nabla \times \vec{E}(\vec{r}, \omega) &= i\omega\mu_0 \vec{H}(\vec{r}, \omega) \\ \nabla \times \vec{H}(\vec{r}, \omega) &= -i\omega\varepsilon \vec{E}(\vec{r}, \omega).\end{aligned}\quad (2.25)$$

Taking the curl of both sides of equations (2.25) yields

$$\begin{aligned}\nabla^2 \vec{E} + \omega^2 \varepsilon \mu_0 \vec{E} - \nabla(\nabla \cdot \vec{E}) &= 0 \\ \nabla^2 \vec{H} + \omega^2 \varepsilon \mu_0 \vec{H} + \frac{\nabla \varepsilon}{\varepsilon} \times (\nabla \times \vec{H}) &= 0.\end{aligned}\quad (2.26)$$

These are the principle equations, subject to the continuity of the usual tangential fields across the dielectric interfaces, that need to be solved for the modal field distribution and effective mode index. They can be solved with the help of numerical methods, i.e. finite difference or

finite element methods or using approximate solutions of simplified models, i.e. the effective index method. In the case of the in-diffused waveguides used in the experiments presented in this dissertation and described in the next chapter, a weakly guiding approximation can be assumed. It implies an existence of two types of orthogonal modes: transverse electric (TE) with a dominant E_{ym} field component and transverse magnetic (TM) with a dominant H_{ym} field. It can be easily shown that the TM mode has a dominant electric field component in the z direction, E_{zm} , and it is of course this component that enters the nonlinear polarization equations. In further derivations, a scalar approach which utilizes only the dominant electric field is used.

In order to derive the nonlinear coupling between the FH and SH interacting modes one can represent their fields in the form

$$\begin{aligned} E_{FH} &= \frac{1}{2} \hat{E}_{FH}^m(y, z) u^{FH}(x) e^{i(\beta_{FH}^m x - \omega t)} + c.c. \\ E_{SH} &= \frac{1}{2} \hat{E}_{SH}^n(y, z) u^{SH}(x) e^{i(\beta_{SH}^n x - 2\omega t)} + c.c. \end{aligned} \quad (2.27)$$

where \hat{E}_{FH}^m and \hat{E}_{SH}^n are the FH and SH transverse mode profiles, $u^{FH}(x)$ and $u^{SH}(x)$ are the complex field amplitudes normalized so that $|u^{FH}(x)|^2$ and $|u^{SH}(x)|^2$ give the guided wave power in Watts and β_{FH}^m and β_{SH}^n are the FH and SH modal propagation wavevectors. Using standard couple mode theory [48, 49],

$$\frac{du}{dx} = -\frac{i\omega}{4} \int_{-\infty}^{\infty} \int_{-\infty}^{\infty} P^{pert} \hat{E}^* e^{i(\beta - \beta_{pert})x} dy dz \quad (2.28)$$

where P^{pert} represents the perturbation polarization described by equation (2.5) appropriate to guided waves, the resulting coupled mode equations are

$$\begin{aligned}\frac{du^{FH}}{dx} &= -\frac{i\omega d_{\text{eff}} \varepsilon_0 K^{(2)}}{2} u^{FH*} u^{SH} e^{-i\Delta\beta x} = -i\gamma u^{FH*} u^{SH} e^{-i\Delta\beta x} \\ \frac{du^{SH}}{dx} &= -\frac{i\omega d_{\text{eff}} \varepsilon_0 K^{(2)}}{2} u^{FH} u^{FH} e^{i\Delta\beta x} = -i\gamma u^{FH} u^{FH} e^{i\Delta\beta x}\end{aligned}\quad (2.29)$$

where the overlap integral $K^{(2)}$ is defined as

$$K^{(2)} = \int_{-\infty}^{\infty} \int_{-\infty}^{\infty} \hat{E}_{SH}^{n*} \hat{E}_{FH}^m \hat{E}_{FH}^m dydz = \int_{-\infty}^{\infty} \int_{-\infty}^{\infty} \hat{E}_{SH}^n \hat{E}_{FH}^{m*} \hat{E}_{FH}^{m*} dydz, \quad (2.30)$$

and $\Delta\beta = 2\beta_m^{FH} - \beta_n^{SH}$. Equation (2.29) is the guided wave equivalent to the coupled mode equations (2.8). For the waveguide case, the effective indices of the modes should be considered rather than the bulk refractive indices when calculating wavevector mismatch ($\Delta\beta$ instead of Δk). Also the efficiency of SHG can be changed dramatically according to the value of the overlap integral. If indeed either the FH or the SH field distributions have zeros, interference effects in the overlap integral can significantly reduce the net SH efficiency. As a result, it is usually advantageous to work with the zero order modes, $p = q = 0$. In the experiments, $p = q = 0$ always for the FH modes and the values for the SH will depend on the detailed phase-matching conditions so henceforth the use of subscripts to describe the mode numbers will be dropped.

2.4. Quadratically nonlinear directional coupler

When two waveguides are placed in close proximity (see Figure 2.4) and their modal profiles overlap, a directional coupler is formed. The energy can be transferred from one channel to another due to the tunneling effect via the evanescent field of the first channel overlapping the second guide, and vice versa [49, 50]. The efficiency of this energy transfer mechanism depends on the separation between the guides, the size of modes and the propagation constants of both

channels. When only one channel is excited, a periodic power exchange between the two channels occurs.

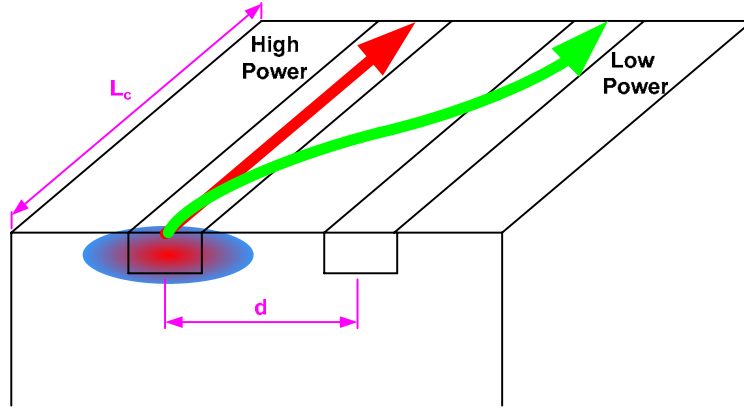


Figure 2.4 Nonlinear directional coupler geometry.

This situation is somewhat analogous to the power transfer between the FH and SH for finite wavevector mismatch described in the previous chapter. Actually the strength of the coupling can be derived using the same coupled mode theory given in equation (2.28). In this case the perturbation polarization produced in the second channel by the field in the first channel is defined as

$$P_2^{pert} = \Delta\epsilon\epsilon_0\hat{E}_1 \quad (2.31)$$

where $\Delta\epsilon$ is the change in the relative permittivity introduced by the presence of the second guide and \hat{E}_1 is the unperturbed field of the first waveguide. This results in coupled mode equations [51]

$$\begin{aligned} \frac{du_1^{FH}}{dx} &= -\frac{i\omega\epsilon_0 K^{(1)}}{4} u_2^{FH} e^{i\Delta\kappa x} \\ \frac{du_2^{FH}}{dx} &= -\frac{i\omega\epsilon_0 K^{(1)}}{4} u_1^{FH} e^{-i\Delta\kappa x} \end{aligned} \quad (2.32)$$

where u_1^{FH} and u_2^{FH} are the FH complex amplitudes of the fields propagating in channels 1 and 2 respectively. The mismatch between the propagation constants of the two channels (to be distinguished from the wavevector mismatch $\Delta\beta$ between the FH and SH) is $\Delta\kappa = \beta_2^{FH} - \beta_1^{FH}$. Note that the subscripts on β which previously referred to mode numbers now refer to the channels and that as stated previously it is implicitly assumed that the FH mode is the lowest order mode. The choice of only the FH and the neglect of coupling between the SH in adjacent waveguides will be discussed later. For two identical waveguides with the same propagation constants ($\Delta\kappa = 0$) equation (2.32) simplifies to an expression of the form

$$\begin{aligned}\frac{du_1^{FH}}{dx} &= -\frac{i\omega\varepsilon_0 K^{(1)}}{4} u_2^{FH} = -iC_{FH} u_2^{FH} \\ \frac{du_2^{FH}}{dx} &= -\frac{i\omega\varepsilon_0 K^{(1)}}{4} u_1^{FH} = -iC_{FH} u_1^{FH}\end{aligned}\quad (2.33)$$

where

$$K^{(1)} = \int_{-\infty}^{\infty} \int_{-\infty}^{\infty} 2n_1 \Delta n_1 \hat{E}_2 \hat{E}_1^* dydz = \int_{-\infty}^{\infty} \int_{-\infty}^{\infty} 2n_2 \Delta n_2 \hat{E}_1 \hat{E}_2^* dydz \quad (2.34)$$

and C_{FH} is the coupling constant between adjacent channels.

The distance required for complete energy transfer from one (the input) channel (usually called the bar channel) to another (cross channel) is defined as a half-beat coupling length and it can be expressed as

$$L_c = \frac{\pi}{2C_{FH}}. \quad (2.35)$$

This is one of the most important parameters, both for a directional coupler, and the arrays to be discussed later in this chapter.

A nonlinear device (either Kerr or cascaded second order nonlinearity) with a length equal to the coupling length L_c is called a nonlinear directional coupler (NLDC). In the cascading case, the nonlinearity introduces additional nonlinear phase shifts which affect the wavevector matching condition. At sufficiently high powers, the input channel is detuned from the adjacent channel so that energy transfer between channels is inhibited [52] (as shown in red in Figure 2.4). Combining now both the linear and nonlinear effects, the equations governing a cascading NLDC are

$$\begin{aligned}
i \frac{du_1^{FH}}{dx} &= C_{FH} u_2^{FH} + \gamma u_1^{FH*} u_1^{SH} e^{-i\Delta\beta x} & i \frac{du_2^{FH}}{dx} &= C_{FH} u_1^{FH} + \gamma u_2^{FH*} u_2^{SH} e^{-i\Delta\beta x} \\
i \frac{du_1^{SH}}{dx} &= C_{SH} u_2^{SH} + \gamma u_1^{FH} u_1^{FH} e^{i\Delta\beta x} & i \frac{du_2^{SH}}{dx} &= C_{SH} u_1^{SH} + \gamma u_2^{FH} u_2^{FH} e^{i\Delta\beta x}
\end{aligned} \tag{2.36}$$

It will be argued in the next section that the coupling between the SH fields of the adjacent channels can be neglected so that $C_{SH} \approx 0$.

NLDC's have been extensively studied previously, both theoretically [53-55] and experimentally [56-58] utilizing Kerr and cascaded second order nonlinearities. However practical applications in signal processing have been restricted by the high powers required for operation.

2.5. Waveguide arrays

Waveguide arrays consist of equally spaced, parallel, weakly coupled, channel waveguides. They are a natural extension of directional couplers with now every channel flanked by two channels [17]. Let us assume an infinitely wide array in the y direction (see Figure 2.5).

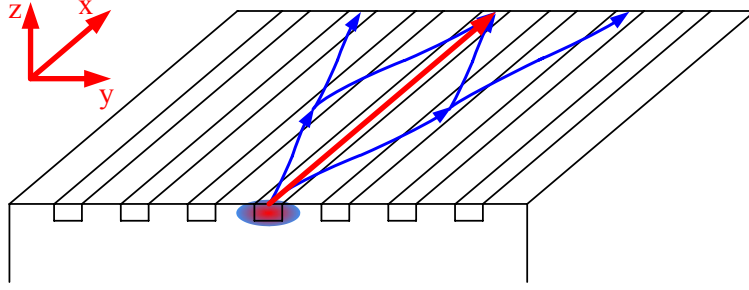


Figure 2.5 Waveguide array geometry.

The propagation of the envelopes of the complex amplitude fields in the individual channels, specifically channel n , is governed by the same kind of coupled equations as for the NLDC,

$$\begin{aligned}
 i \frac{du_n^{FH}}{dx} &= C_{FH} (u_{n-1}^{FH} + u_{n+1}^{FH}) + \gamma u_n^{FH*} u_n^{SH} e^{-i\Delta\beta x} \\
 i \frac{du_n^{SH}}{dx} &= C_{SH} (u_{n-1}^{SH} + u_{n+1}^{SH}) + \gamma u_n^{FH} u_n^{FH} e^{i\Delta\beta x}
 \end{aligned}
 \tag{2.37}$$

where both linear (constants C_{FH} and C_{SH}) and nonlinear (constant γ) couplings are included. Equations (2.37) are a discrete version of the well-known coupled equations describing SHG in a bulk medium. Note that the field in the n -th channel is coupled to the fields in both neighboring channels $n+1$ and $n-1$. For the SH case it can be assumed that $C_{SH} \approx 0$. This can be easily seen in Figure 2.6 which shows the PPLN samples used and the associated modal fields. The field overlap is effectively zero for the SH in any two adjacent channels.

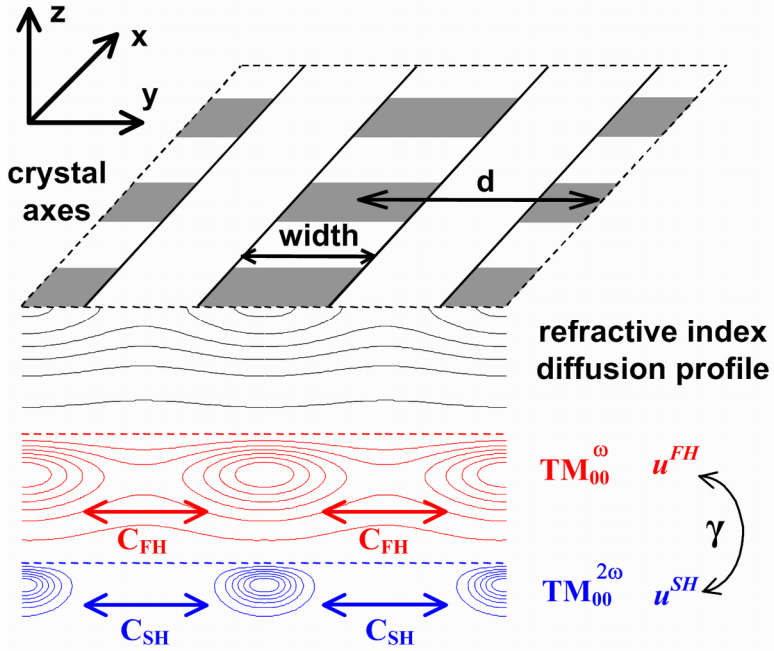


Figure 2.6 Cross-sectional cut of the PPLN waveguide array sample used in the transverse y - z plane showing the channel index profile, and the overlapped FH ($\hat{E}_{FH}^0(y, z)$) fields and SH ($\hat{E}_{SH}^0(y, z)$) fields. Note the tight confinement of SH causing $C_{SH} \approx 0$.

It is straightforward to show that these equations for the envelope FH fields reduce, in the appropriate limit of small waveguide spacing relative to the beam width, to the continuum coupled mode equations. (The SH fields do not couple between channels.) After a simple transformation

$$u_n^{FH} = \tilde{u}_n^{FH} e^{-i2C_{FH}x} \quad (2.38)$$

the linear FH part becomes

$$i \frac{d\tilde{u}_n^{FH}}{dx} = C_{FH} (\tilde{u}_{n-1}^{FH} - 2\tilde{u}_n^{FH} + \tilde{u}_{n+1}^{FH}) \quad (2.39)$$

where the nonlinear part has been temporarily dropped for convenience. The term $\tilde{u}_{n-1}^{FH} - 2\tilde{u}_n^{FH} + \tilde{u}_{n+1}^{FH}$ can be recognized as the discrete approximation of the second derivative

operator $\partial^2 \tilde{u}^{FH} / \partial y^2$ where $y = nd$ (d is a separation between adjacent channels). Thus in the continuum approximation, when an input beam excites many channels, equation (2.39) can be approximated by

$$i \frac{d\tilde{u}_n^{FH}}{dx} = C_{FH} d^2 \frac{\partial^2 \tilde{u}_n^{FH}}{\partial y^2}. \quad (2.40)$$

In contrast to the continuous case where the diffraction coefficient is a constant and equal to $1/2k$, the discrete diffraction coefficient is adjustable by varying the coupling constant C_{FH} and channel separation d .

However for the case when only few or just a single channel is excited, the discreteness of the system plays a very important role. The linear and nonlinear properties of quadratic waveguide arrays in the discrete regime are discussed in next two sections.

Finally, it is noteworthy that the coupled mode approach used here just gives the lowest order band of this periodic structure. A more rigorous analysis using Bloch waves would predict additional higher order bands [59, 60]. These in fact do appear in the experimental results, but principally as spurious effects and will be noted when appropriate.

2.5.1. Linear properties of discrete arrays

For beam propagation in a continuous medium, the standard approach used to derive the dispersion relation between \vec{k} and ω is to assume plane wave solutions and substitute them into Maxwell's equations. For example, in an one dimensional isotropic medium, this yields $k_x^2 + k_y^2 = n^2 k_0^2$, i.e. the modulus of the wavevector is a constant. The equivalent procedure is now used to derive a relation between k_x and k_y in an array. The propagation of a discrete "plane wave" in the coupled mode approximation consists of setting the envelope fields evaluated at the

center of each waveguide u_n equal to the complex value u_0 . Taking into account the spatial periodicity of the array, the “plane wave” field in one transverse dimension is written as

$$u_n^{FH} = u_0 e^{i(\Delta k_x x + n k_y d)}. \quad (2.41)$$

Here Δk_x is the additional longitudinal wavevector contribution to the single channel propagation constant β , i.e. $k_x = \beta + \Delta k_x$ due to the inter-channel coupling and $k_y d$ represents the relative phase difference between neighbor channels which occurs when the “plane wave” travels transversely across the array. (This phase difference is achieved in an array simply by tilting the input beam in the x-y plane about the z-axis.) Substituting the “plane wave” ansatz (2.41) into the first equation of (2.37) with the nonlinear term set to zero one can find the linear relation between Δk_x and $k_y d$ to be [21]

$$\Delta k_x = 2C_{FH} \cos(k_y d). \quad (2.42)$$

This functional relation is shown in Figure 2.7. Thus the magnitude of the longitudinal propagation constant in the array becomes

$$k_x = \beta + 2C \cos(k_y d). \quad (2.43)$$

When compared to the angular dependence of the propagation wavevector in a continuous system, it is clear that the discrete system shows some unique properties. The “discrete diffractive” properties, i.e. beam spreading due to inter-channel transfer, can be obtained by analogy again to the continuous medium case. Two quantities are defined based on the two lowest order spatial derivatives

$$G = \frac{\partial k_x}{\partial k_y} \quad (2.44)$$

$$D = \frac{\partial^2 k_x}{\partial k_y^2}$$

where G is called a “group” velocity and represents the transverse angular displacement of the beam, and D is a diffraction parameter describing angular spread of the beam. The angular dispersion is periodic with a periodicity of 2π in $k_y d$, so that the analysis can be restricted to the first Brillouin zone of this periodic system, i.e. to $|k_y d| \leq \pi$ without loss of generality.

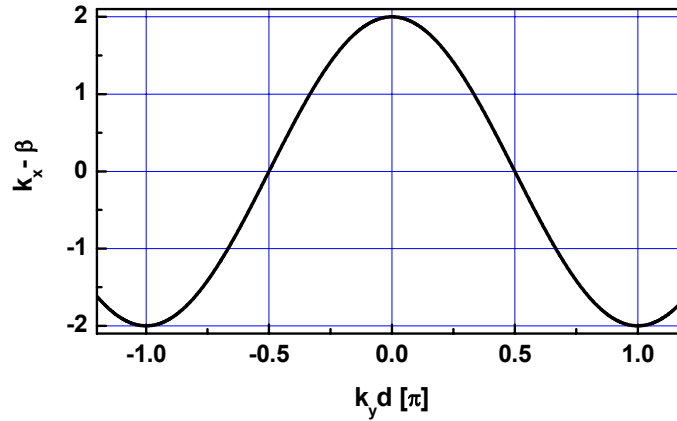


Figure 2.7 Angular dispersion in the coupled array induced propagation wavevector, $\Delta k_x = k_x - \beta$ vs. k_y in a waveguide array.

The “discrete dispersion” relation exhibits two curvatures with inflection points located at $|k_y d| = \pi/2$. In the first region $|k_y d| \leq \pi/2$, where the diffraction parameter D is negative, it resembles the diffraction properties of a continuous system and hence is called “normal diffraction”. In the second region $\pi/2 \leq |k_y d| \leq \pi$, the diffraction parameter D changes its sign and becomes positive. In analogy to pulse propagation i.e. in fibers [43], this region exhibits so-called “anomalous diffraction” which does not exist in continuous system in the spatial domain and is a unique feature of the discrete properties of the system.

Knowing this angular dispersion relation, one can find the impulse response of the system, i.e. when only one channel is excited. The exact solution is given by [17, 21]

$$u_n^{FH}(x) = (i)^n J_n(2Cx) \quad (2.45)$$

and is shown in Figure 2.8 where J_n is the n -th order Bessel function. The discrete diffraction pattern exhibits a preferential power flow from the initially excited channel towards the outermost wings of the input. Most of the power is concentrated there. This is in contrast to the “bell-shaped distribution associated with continuous media which maintains a peak centered on the transverse position of the input. These two lobes travel with the maximum group velocity $G_{\max} = 2Cd$.

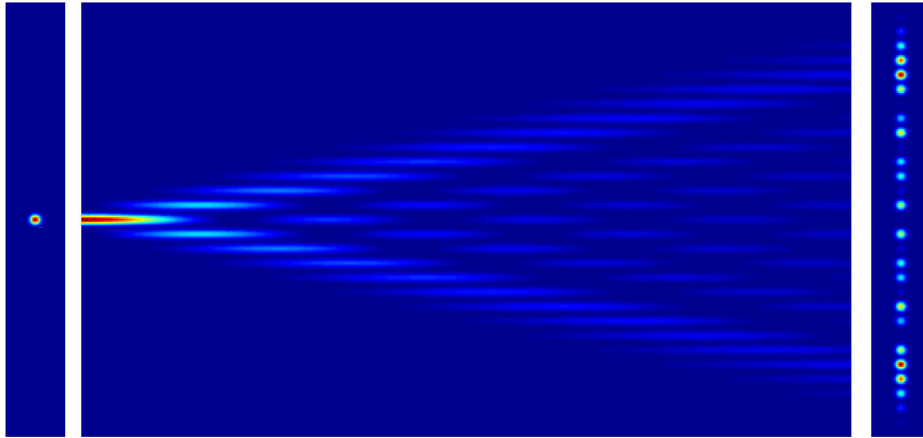


Figure 2.8 Discrete diffraction pattern for single channel excitation.

2.5.2. Nonlinear properties and discrete quadratic solitons

Discrete diffraction can be reduced and even canceled by nonlinear effects, just as in the continuous media case. (This of course implies that spatial solitons are possible in discrete

systems.) In the simplest case, a high intensity beam can utilize the Kerr nonlinearity to change locally the refractive index and hence the propagation constants of the array's channels. The resulting mismatch in the propagation constants will detune the synchronous linear coupling due to the tunneling effect between the channels, an effect well-known in NLDCs. Solitons are the self-trapped, non-diffracting beams that can propagate in the medium without change in amplitude profile. Before the work described in this dissertation, the experimental studies of discrete solitons were restricted primarily to frequency degenerate effects in media with Kerr [27, 61], photorefractive [29, 62], and orientational nonlinearities [31] where various discrete solitons associated with diverse linear diffraction properties have been observed. But because the very interplay between these linear transport phenomena and the nonlinearity governs the localization process, it is challenging to study localization phenomena for other more diverse nonlinearities. In this respect quadratic nonlinearities deserved particular attention because the interaction involves two or three components at different frequencies and new degrees of freedom enter the dynamical process.

In the case of quadratically nonlinear media, the strong interaction between the FH and SH waves produces nonlinear (cascading) phase shifts which are equivalent to changes in refractive index, thus potentially arresting diffraction. Quadratic solitons are the stationary solutions to the FH-SH coupled wave equations and have indeed been observed in a variety of $\chi^{(2)}$ -active continuous media near the phase-matching condition for second harmonic generation. These solitons consist of both an in-phase FH and SH field component, with the amplitude ratio and total power determined by the wavevector mismatch. There is already a rich literature on these solitons [63].

By analogy, discrete quadratic solitons in the lowest order band of this periodic structure are stationary solutions of coupled mode equations (2.37). Under appropriate conditions they can propagate in a limited range of directions (k_x, k_y) down and across the array although the details of the field structure can be different in different regions of discrete diffraction. Six different bright soliton solutions have been predicted [22, 23], depending on the sign of nonlinearity (or wavevector mismatch $\Delta\beta$), sign of the diffraction coefficient D , symmetry of the excited guides and position of the field maximum in respect to the guides (see Figure 2.9). If the soliton's envelope maximum is centered on one of the guides the soliton is called odd (or on-site), if the maximum occurs between waveguides the soliton is called even (or inter-site). Only the odd solitons are stable and robust to small perturbations. The even ones, under any perturbation, try to evolve on propagation into one of the stable odd solutions. Special cases are twisted solutions which resembles even solitons with a π phase jump in the center of symmetry of the field.

The distinction between the staggered and unstaggered families comes from location of the soliton in the Brillouin zone. The unstaggered solitons (all channels excited in-phase) are located in the middle of the zone ($k_y d = 0$), while the staggered ones (π phase shift between neighbor channels) are located at the edge of the zone ($k_y d = \pi$). To support the solitons, the correct combination of diffraction and nonlinearity has to be met. Unstaggered bright solitons exist only for the positive nonlinearity (wavevector mismatch $\Delta\beta > 0$). On the other hand, staggered ones exist only for the negative nonlinearity ($\Delta\beta < 0$). The wrong combination of signs for the diffraction coefficient and nonlinearity leads to enhanced diffraction. This would occur for D negative and $\Delta\beta < 0$, as well as for D positive and $\Delta\beta > 0$.

At intensities far above soliton threshold, discrete solitons can no longer slide across the array and they become “locked” into their incidence channels. This is a consequence of an

increased decoupling between adjacent channels with increasing intensity, i.e. the field distributions become narrower and are no longer given by the modal ones associated with the individual waveguides.

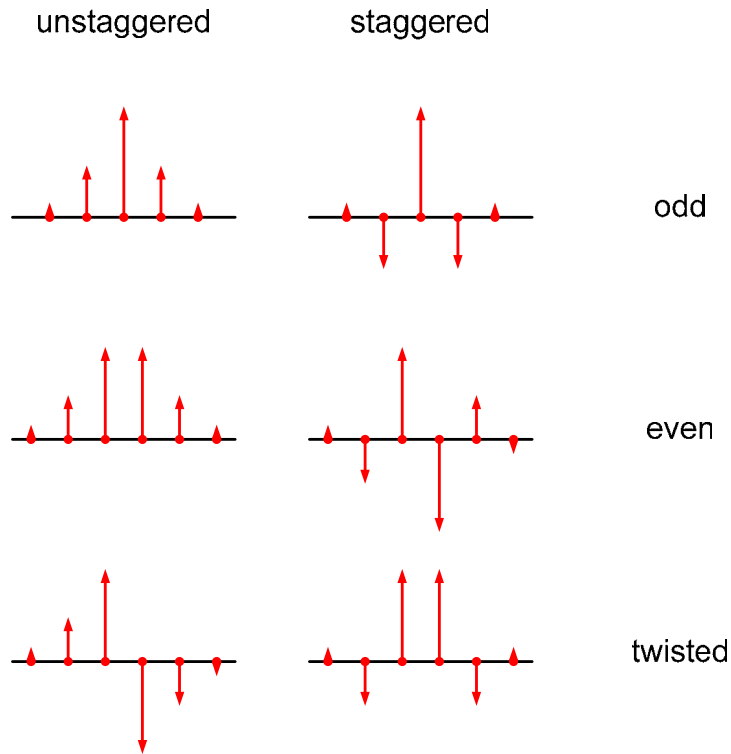


Figure 2.9 FH envelope field distribution for different kinds of bright solitons.

A computer program based on the coupled equations was developed and made available by the collaborating group of Dr. Falk Lederer at the Friedrich Schiller University in Jena, Germany. Temporal effects like group velocity dispersion (GVD) and pulse walk-off, and spatial variations of wavevector mismatch due to temperature profile were included. For degenerate case, i.e. SHG, the following system of equations was solved numerically

$$\begin{aligned}
i \frac{\partial u_n^{FH}}{\partial x} - \frac{\beta_2^{FH}}{2} \frac{\partial^2 u_n^{FH}}{\partial t^2} - C(u_{n+1}^{FH} + u_{n-1}^{FH}) + i \frac{\alpha^{FH}}{2} u_n^{FH} &= \gamma u_n^{FH*} u_n^{SH} e^{i\Delta\beta x} \\
i \frac{\partial u_n^{SH}}{\partial x} - \frac{\beta_2^{SH}}{2} \frac{\partial^2 u_n^{SH}}{\partial t^2} + i\delta \frac{\partial u_n^{SH}}{\partial t} + i \frac{\alpha^{SH}}{2} u_n^{SH} &= \gamma u_n^{FH} u_n^{FH} e^{-i\Delta\beta x}
\end{aligned} \tag{2.46}$$

where β_2^{FH} and β_2^{SH} are GVD parameters, α^{FH} and α^{SH} the linear losses for the FH and SH fields respectively and δ is a walk-off parameter defined as

$$\delta = \frac{\partial \beta^{SH}}{\partial \omega} - \frac{\partial \beta^{FH}}{\partial \omega} \tag{2.47}$$

These programs were used to simulate many of the experiments described later in this dissertation.

CHAPTER THREE: SAMPLES

3.1. Introduction

Many factors were considered during choosing lithium niobate (LiNbO_3) as the sample material. It is a ferroelectric, uniaxial oxide which has many attractive properties. Its large piezoelectric coefficient has led to its extensive use in radio frequency acoustic wave devices [64]. Lithium niobate also has a large electro-optic coefficient which is used in guided wave interferometry [65]. These and other applications have led to a large-scale production of quality lithium niobate substrates.

Lithium niobate is also a very attractive nonlinear optical material with a relatively large nonlinear coefficient ($d_{33} = 22.7 \text{ pm/V}$ for congruent LiNbO_3). Recent development of QPM technology enables, by accessing this coefficient, an efficient Second harmonic Generation (SHG). Its transparency range spans from ultraviolet to mid-infrared (325 – 4500 nm) [66].

Various approaches to waveguide fabrication in lithium niobate have been investigated over the past thirty years, including in-diffusion of titanium [67, 68], zinc [69] and protons [70]. Among these methods, titanium in-diffusion exhibits the best linear properties. Typical loss measured experimentally in SHG experiments at 1550 nm was in order of $0.15 \div 0.20 \text{ dB/cm}$ for the fundamental wave (FH) and $0.30 \div 0.40 \text{ dB/cm}$ for the second harmonic (SH). Homogeneity of the sample, both transverse and longitudinal, was excellent.

3.2. Fabrication

Samples for the experiments shown in this dissertation were fabricated at University of Paderborn in Dr. Wolfgang Sohler's group. Figure 3.1 schematically shows the fabrication steps. Congruent Z-cut LiNbO_3 wafers of 4 inch diameter and 0.5 mm thickness from Crystal Technology Inc. were used as substrates. A 98 nm thick titanium layer was vacuum deposited by electron beam evaporation on the (-Z)-surface of the LiNbO_3 substrate. Using photolithography 7 μm wide channels were defined (see Figure 3.1a). The titanium was in-diffused into the surface region for 7.5 hours at 1060 $^\circ\text{C}$ in an argon atmosphere, followed by one hour post-diffusion at 1060 $^\circ\text{C}$ in oxygen (see Fig. 2.1b). During the Ti in-diffusion, a shallow domain inverted layer is formed on the (+Z)-face (see Figure 3.1b). Since this layer prohibits electric field poling it is removed by careful grinding (see Figure 3.1c). Domain inversion always starts from the (+Z)-face. Therefore, it is advantageous to have the waveguides and the periodic electrode structure on the (+Z)-face in order to obtain the best definition of the QPM grating in the waveguide.

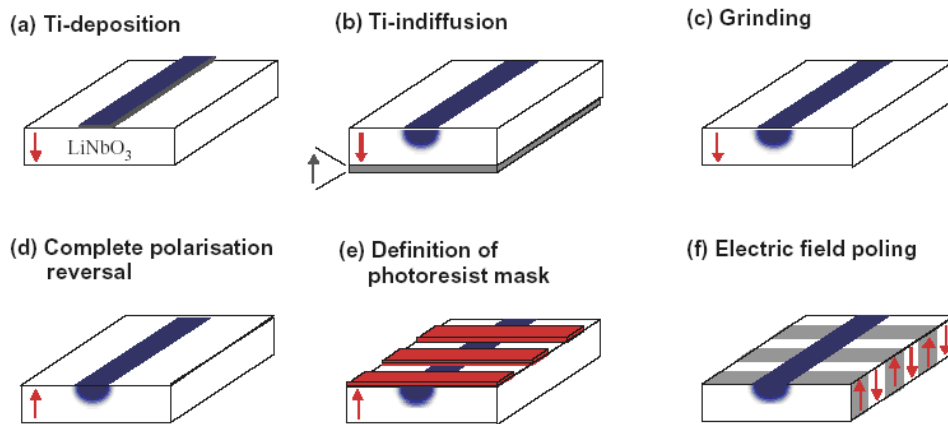


Figure 3.1 Fabrication steps to obtain a periodically poled channel waveguide.

The next fabrication step is a homogeneous polarization reversal of the whole sample (see Figure 3.1d). Thereafter, the periodic micro-domain structure was fabricated by using the electric field poling method with the structured electrolyte electrode on the (+Z)-side (see Figure 3.1e). The poling conditions including time, voltage, current and total charge were optimized in order to obtain a 50/50 duty cycle of the grating and a good homogeneity. The substrate was diced and both end faces were polished (see Figure 3.1f).

The sample waveguides and periodic poling were designed based on the Sellmeier equation published in [71] which defines the dispersion in the refractive index. The refractive index change is determined by the local Ti concentration $c(y, z)$ investigated in [72, 73]

$$c(y, z) = c_0 f(u) g(s) \quad (3.1)$$

where

$$u = \frac{z}{D_{\parallel Z}}, \quad s = \frac{2y}{W} \quad (3.2)$$

$$f(u) = \exp(-u^2) \quad (3.3)$$

$$g(s) = \frac{\operatorname{erf}\left[\frac{W}{2D_{\perp Z}}(1+s)\right] + \operatorname{erf}\left[\frac{W}{2D_{\perp Z}}(1-s)\right]}{2} \quad (3.4)$$

and y and z are the lateral and the depth coordinates in a plane perpendicular to the waveguide propagation axis X (see Figure 3.2). W is the Ti-strip width and $D_{\parallel Z}$, $D_{\perp Z}$ are the diffusion constants parallel and perpendicular to axis Z respectively. The following values of the diffusion depth constants were assumed, based on previous work done by Schiek in [74] and [68]: $D_{\parallel Z} = 5.78 \mu\text{m}$ and $D_{\perp Z} = 4.5 \mu\text{m}$ and c_0 is given by the Ti strip thickness, $\tau = 98 \text{ nm}$, before in-diffusion

$$c_0 = 6.412 \times 10^{22} \text{ cm}^{-3} \frac{\tau}{D_{\parallel Z}} \quad (3.5)$$

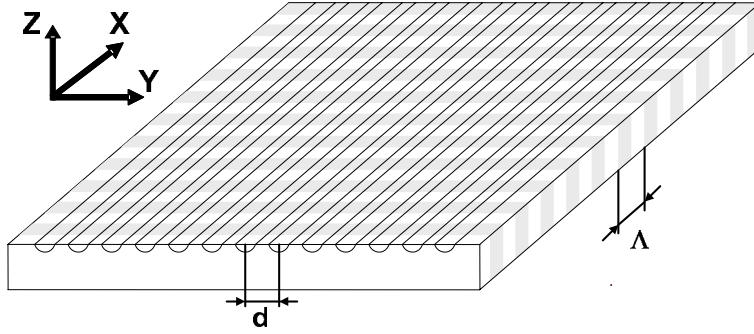


Figure 3.2 Geometry of the sample relative to the crystal axes.

The refractive index profile typical for in-diffused waveguides is shown in Figure 3.3 – the dark blue region at the top of the figure represents air. In the current case the maximum refractive index change due to Ti in-diffusion was $\Delta n < 8 \cdot 10^{-3}$.

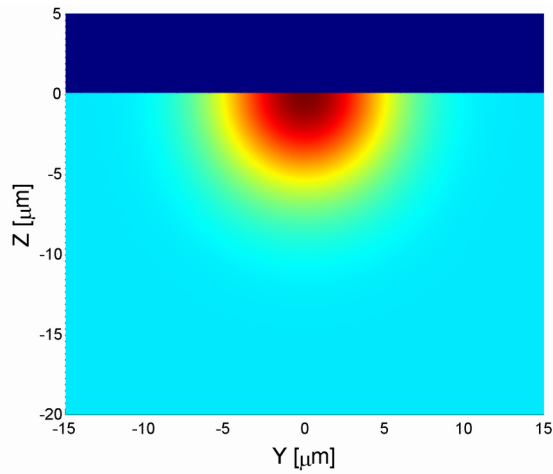


Figure 3.3 Typical refractive index distribution for a Ti in-diffused channel waveguide.

Only TM modes were considered in the design because only they can be quasi-phase-matched (QPM) using the nonlinear coefficient d_{33} . Such channels support, for TM polarization, single mode propagation for the FH and multi-mode (seven modes) for the SH. The finite

element method was used to calculate mode profiles. Figure 3.4 shows calculated the FH fundamental TM_{00} mode intensity.

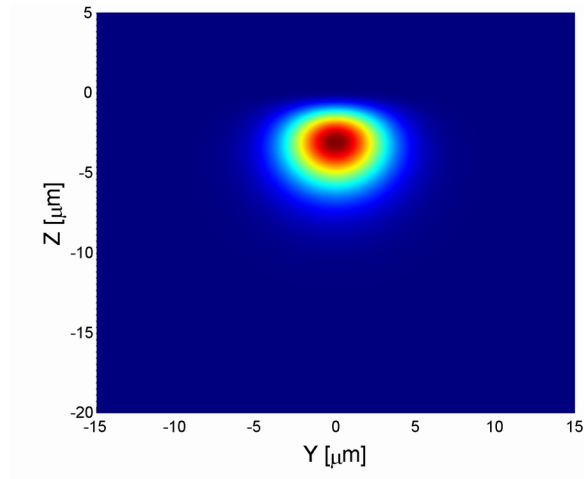


Figure 3.4 Calculated FH fundamental TM_{00} mode intensity.

Figure 3.5 shows selected calculated SH TM mode intensities. However not all of them are phase-matchable – i.e. SH TM_{10} because of the modal symmetry in horizontal plane cannot couple efficiently with FH TM_{00} – i.e. the field overlap integral of these modes is zero. Notice also the much tighter confinement of the SH fundamental mode in comparison with the FH fundamental mode, a consequence of the factor of two between the frequencies.

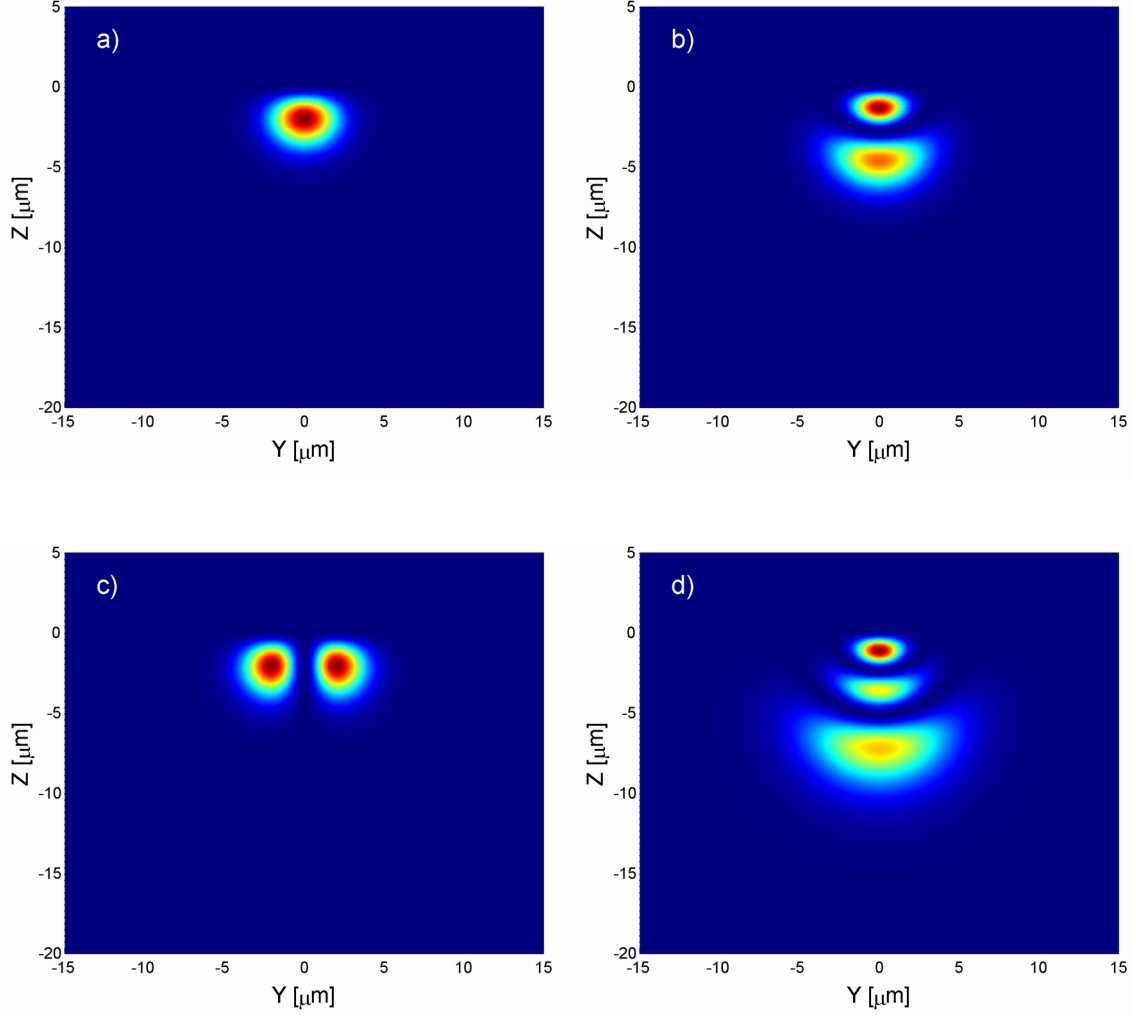


Figure 3.5 Calculated SH TM mode intensities: a) TM₀₀, b) TM₀₁, c) TM₁₀, d) TM₀₂.

The wavelength and temperature dependent effective mode indices are needed to determine the phase-matching conditions. They can be expanded in Taylor series

$$\begin{aligned}
 n_i(\lambda, T) = & n_i(\lambda_0, T_0) + \frac{\partial n_i}{\partial \lambda} (\lambda - \lambda_0) + \frac{1}{2} \frac{\partial^2 n_i}{\partial \lambda^2} (\lambda - \lambda_0)^2 + \\
 & + \frac{\partial n_i}{\partial T} (T - T_0) + \frac{1}{2} \frac{\partial^2 n_i}{\partial T^2} (T - T_0)^2
 \end{aligned} \tag{3.6}$$

where

$$\lambda_0 = 1550 \text{ nm for the FH}$$

$$\lambda_0 = 775 \text{ nm for the SH}$$

$$T_0 = 220^\circ\text{C}$$

Mixed second order and higher order derivatives can be neglected. Table 3.1 lists calculated effective indices of TM modes based on equation (3.6) for the fundamental FH and the four lowest orders SH modes.

Table 3.1 Effective mode indices at $T_0 = 220^\circ\text{C}$ for FH and SH modes.

	TM₀₀	TM₀₁	TM₀₂	TM₀₃
FH	2.149302			
SH	2.195426	2.193753	2.192568	2.192242

Table 3.2 lists the values of the Taylor expansion coefficients used in equation (3.6).

Table 3.2 Taylor series expansion coefficients for FH and SH TM₀₀ modes for $\lambda_0 = 1550 \text{ nm}$ for the FH and $\lambda_0 = 775 \text{ nm}$ for the SH at $T_0 = 220^\circ\text{C}$.

	$\frac{\partial n_i}{\partial \lambda} [\text{nm}^{-1}]$	$\frac{\partial^2 n_i}{\partial \lambda^2} [\text{nm}^{-2}]$	$\frac{\partial n_i}{\partial T} [\text{K}^{-1}]$	$\frac{\partial^2 n_i}{\partial \lambda^2} [\text{K}^{-2}]$
FH	-32.8x10⁻⁶	23x10⁻⁹	57.8x10⁻⁶	132x10⁻⁹
SH	-135.6x10⁻⁶	535x10⁻⁹	71.5x10⁻⁶	151x10⁻⁹

A vanishing wavevector mismatch between two modes, defined as

$$\Delta\beta = 2\beta_{FH}(\lambda_{FH}, T) - \beta\left(\frac{\lambda_{FH}}{2}, T\right) + \frac{2\pi}{\Lambda_{QPM}(T)}, \quad (3.7)$$

determines the phase-matching wavelength for a given temperature and waveguide profile. Here,

$$\Lambda_{QPM}(T) = \Lambda_{QPM@20^\circ C} \left[1 + 1.54 \cdot 10^{-5} \left(\frac{T}{^\circ C} - 20 \right) \right] \quad (3.8)$$

is the temperature dependent (due to the thermal expansion of the crystal) required QPM-grating period.

The QPM period was chosen to phase-match the TM_{00} modes of the FH and SH which have the highest mode overlap integral at the elevated temperature $T_0 = 220^\circ C$ (elevated to avoid photorefractive effects in the crystal). This is achieved for the QPM period of $\Lambda = 16.803 \mu m$ at $T_0 = 220^\circ C$, which corresponds to QPM period of $\Lambda = 16.751 \mu m$ at room temperature.

For this QPM grating period, a graphic solution of equation (3.8) for the resonances between the FH TM_{00} mode and three lowest order phase-matchable SH TM modes are shown in Figure 3.6 for a temperature of $220^\circ C$. For the dispersion of the higher order SH modes, the Taylor series coefficients of the SH TM_{00} as discussed above were used.

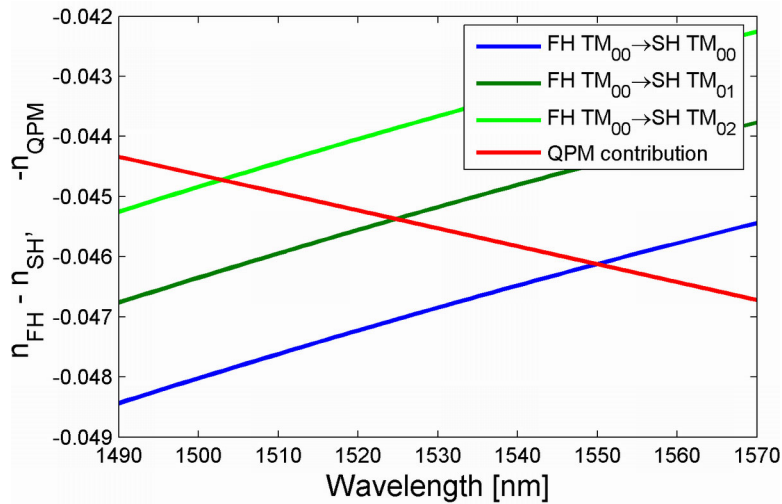


Figure 3.6 Wavelengths for phase-matching between the FH TM_{00} and different SH TM modes for a QPM grating with $\Lambda = 16.751 \mu m$ (at room temperature) for $T_0 = 220^\circ C$.

Figure 3.7 shows the expected wavevector mismatch versus temperature and wavelength for a $L = 5$ cm long sample. The theoretical data are limited in accuracy to ± 2 nm due to truncation of the Taylor expansion after the 2nd order. The calculated temperature-wavelength dependence is 4.47 °C/nm.

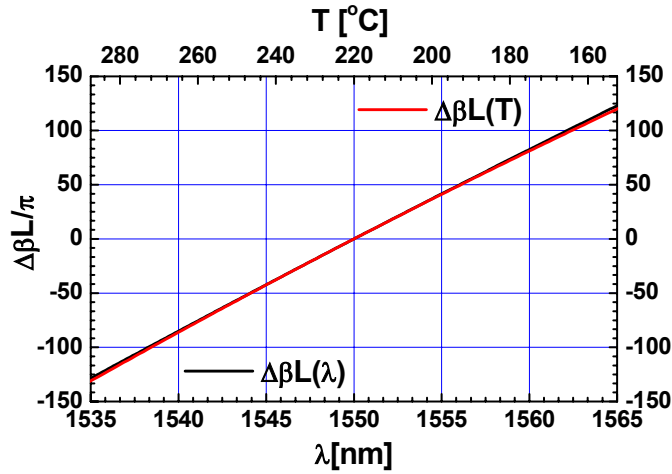


Figure 3.7 Phase-mismatch $\Delta\beta L$ between the FH and the SH TM_{00} modes for a QPM grating with $\Lambda = 16.751$ μm (at room temperature) versus temperature and wavelength for a 5 cm long sample.

From the mode profiles of the TM modes at the FH and SH wavelength the overlap integrals $K^{(2)}$ (see chapter 2.3) can be calculated (see Table 3.3). Neglecting losses and FH depletion, the SH output power in a uniform phase-matched waveguide can be expressed by

$$P_{SH} = \left(\frac{\omega_{FH} \chi_{eff}^{(2)} K^{(2)} L}{2} \right)^2 (P_{FH})^2 \quad (3.9)$$

where L is the crystal length and P_{FH} , P_{SH} are FH and SH powers in W and $\chi_{eff}^{(2)}$ is the effective second order nonlinear susceptibility.

The frequently quoted SHG efficiencies are

$$\eta_n = \frac{P_{SH}}{(P_{FH})^2} \quad (3.10)$$

$$\eta_{nl} = \frac{P_{SH}}{(P_{FH} L)^2} \quad (3.11)$$

Table 3.3 Coupling integrals $K^{(2)}$ and SHG efficiencies for different FH-SH resonances for a 5 cm long sample.

FH TM ₀₀ ⇒	SH TM ₀₀	SH TM ₀₁	SH TM ₀₂
$K^{(2)}$ [V ³ /m]	7.84x10⁸	4.26x10⁸	0.78x10⁸
η_n [%/W]	930	275	9.25
η_{nl} [%/W·cm ²]	37.2	11.0	0.37

Eight different waveguide arrays, with various channel-to-channel separation ranging from 12 to 16 μm , each consisting of 101 channels (some samples fabricated later had only 51 channels for 16 μm separation array) were designed. As discussed previously in Chapter 2, the fundamental building block of the arrays is a directional coupler consisting of two coupled channel waveguides. As it was also shown there, it is the coupling length that governs the response of the array. This coupling length is the distance required for light, initially injected into one channel, to emerge completely to the second. It was evaluated numerically by using the same finite element mode solver used for single channel waveguides to calculate the effective indices of the two “supermodes” of a directional coupler with variable separation between channels. It was assumed that the titanium concentration in the coupler structure is a

superposition of the concentration profiles of the two separate channels. The coupling length L_c of the coupler can be determined from the difference Δn of the effective indices of the two “supermodes”.

$$L_c = \frac{\lambda}{2\Delta n} \quad (3.12)$$

Because of the strongly confined nature of the SH fields, the coupling length for SH is very large relative to the sample length. Thus SH coupling between channels can be neglected. The coupling length for the FH depends on the center-to-center distance between channels (see Figure 3.8). For our samples the coupling length can be fitted with the formula

$$L_c = 2.64751 \cdot \exp\left(\frac{d - 11.94586}{2.11267}\right) \quad (3.13)$$

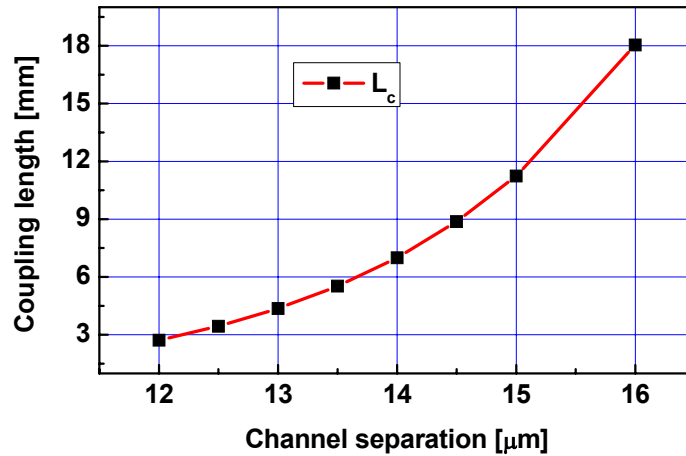


Figure 3.8 Calculated coupling length versus channel-to-channel separation.

For phase-matching exactly at the wavelength of $\lambda = 1.55 \mu\text{m}$ a QPM grating with a periodicity of $\Lambda = 16.751 \mu\text{m}$ at room temperature is needed. With the available technology (resolution of 20 nm) this grating cannot be fabricated. Therefore an averaging technique was

used where periods within the raster of the mask resolution were distributed such that the spatial average provides the desired periodicity [75]. For example, for $\Lambda = 16.751 \mu\text{m}$, this requires a mixture of periods containing 11 periods with $\Lambda = 16.760 \mu\text{m}$ and 9 periods with $\Lambda = 16.740 \mu\text{m}$.

3.3. Characterization

Eleven samples, each containing 4 different arrays, were delivered to CREOL and characterized over a period of three years. It was concluded that making the required samples to the necessary tolerances was a major technological problem. The actual parameters measured for the samples were different from the designed ones. The uncertainty in the diffusion constants [76] is believed to be a major reason for that. Also small variations in the fabrication procedure influenced the linear and nonlinear properties of the sample. They were characterized at room temperature as well as at an elevated temperature exceeding 180°C in order to avoid the photorefractive effect.

The detailed layout of the sample is sketched in Figure 3.9. Each sample contained four arrays and eight single “witness” channels distributed between the arrays for loss and SHG efficiency characterization purposes.

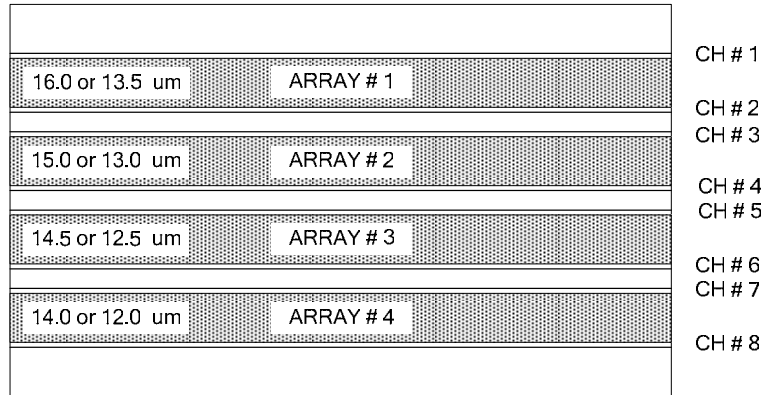


Figure 3.9 Typical sample layout.

Two of the best arrays, one strongly and one weakly coupled, were ultimately chosen as described below and used in the experiments. The total length of the weakly coupled (with channel-to-channel separation $14.0 \div 16.0 \mu\text{m}$) Pb381z sample was 71 mm and the strongly coupled ($12.0 \div 13.5 \mu\text{m}$) Pb344z was 51 mm.

For the characterization of the sample a tunable low power CW source HP81680A by Agilent was used. Linear properties were probed by exciting every single channel in the array and measuring the discrete diffraction pattern at the output. Only arrays with diffraction patterns resembling those in Chapter 2 were deemed acceptable. Later the data was fitted, using a Matlab program, to the equation (2.45) to determine a coupling constant C . This simple experiment was actually the best way of estimating the linear properties of the samples. First of all it gave direct information about the local coupling constant C (or coupling length L_c). Additional information can be extracted from: the uncertainty of the fitting – related to local transverse and longitudinal homogeneities, and variation of C across the whole array – related to overall homogeneity of the array. An example of the one of the best discrete diffraction patterns obtained by a single channel excitation is shown in Figure 3.10.

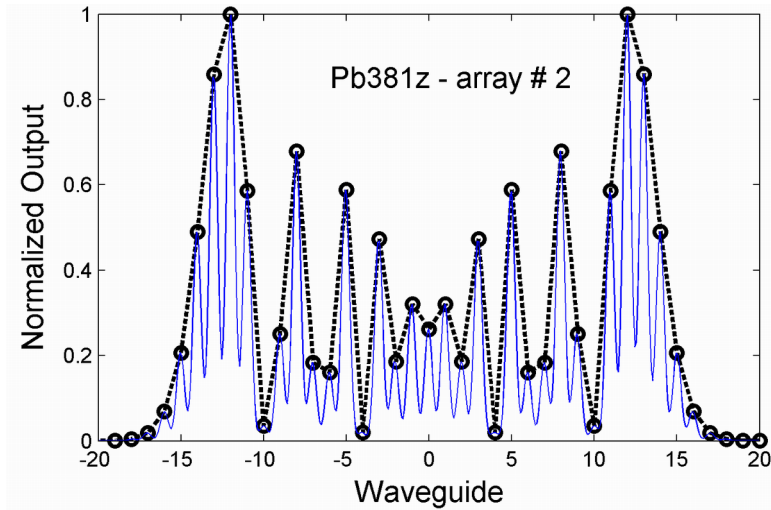


Figure 3.10 The measured discrete diffraction pattern (solid line) for array # 2 with coupling length $L_c = 15.74$ mm in the sample Pb381z for comparison with the best theoretical fit from which the coupling constants were obtained.

Measured values of coupling length for the two chosen arrays are shown in Figure 3.11 and compared with those calculated by the design process. The difference between them can be due to many causes, for example by the assumption of a linear superposition of the titanium concentration contributing from the two neighboring channels.

Dependence of the coupling constant in function of the FH wavelength was measured and results are shown in Figure 3.12. In contrast to AlGaAs arrays [77] where the dispersion was fairly flat, in the case of PPLN samples a significant coupling constant change with wavelength was observed.

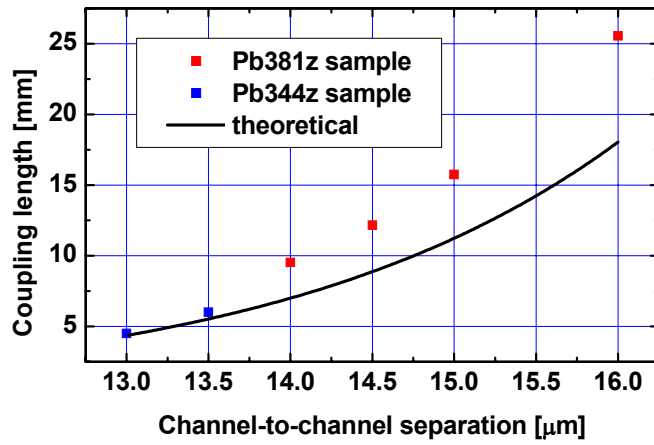


Figure 3.11 Comparison of the measured coupling lengths of the Pb344z and Pb381z samples with calculated ones based on design.

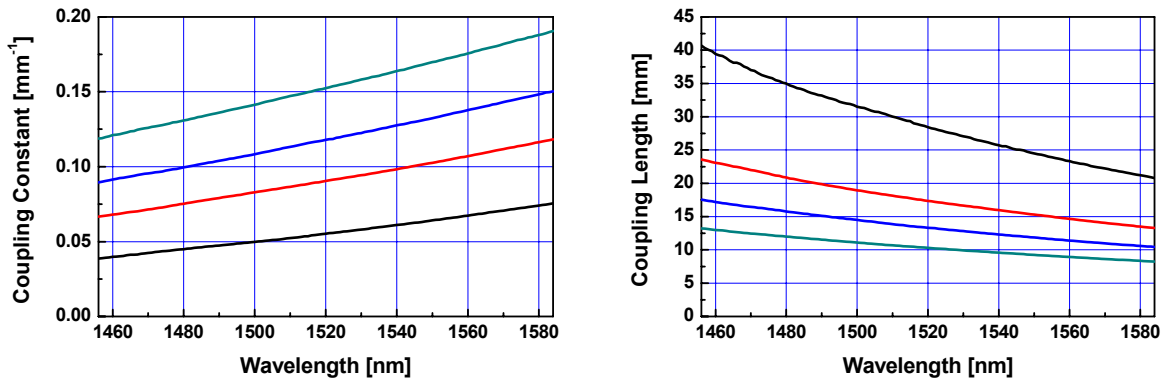


Figure 3.12 Measured coupling constants (on the left) and coupling lengths (on the right) for the Pb381z sample. Each curve represents one array on the sample.

In order to test an array's dispersion relation (see equation (2.43)) and hence the validity of CMT, a wide elliptical beam was launched into the sample. The input beam was then tilted away from the direction of the individual channels and the position at the array output was

recorded. This tilting changes the relative phase between adjacent channels at the input, the angle referred to in Figure 3.13. The variation in the output position with angle gives directly the dispersion relation which is clearly well-approximated by a sine function with good accuracy. However, at the high angles (see angles close to π and $-\pi$) a significant part of energy is coupled to the higher order bands of this periodic structure which indicates a restriction on the validity of CMT to angles just below π .

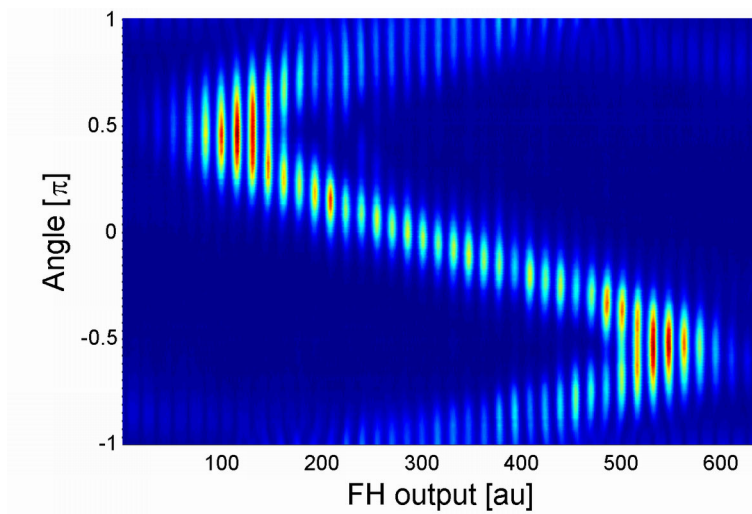


Figure 3.13 Measured dispersion relations for the lowest band for array # 2 in the sample Pb381z with a coupling length $L_c = 15.74$ mm.

The technique just described [78] is an indirect, band structure characterization method based on measuring the shape of the group velocity curve. However, for the PPLN samples in which SHG occurs, there is another method also available. It is based on SHG which requires phase-matching between the FH and the SH waves. Thus if one of the wavevectors is known, the other can be retrieved from the resonance condition. In the case of the PPLN samples, the SH propagation constant has only a longitudinal component (assuming no linear coupling of SH

between channels) and is constant, independent of the tilt angle. Again, an elliptical FH wide beam was launched in the sample and tilted from the direction of channels. For each excitation angle, the FH input wavelength was scanned from 1540 to 1550 nm and the SH tuning curve measured with a photodiode. As a result of the measurement a direct plot of the FH fundamental band was obtained (see Figure 3.14).

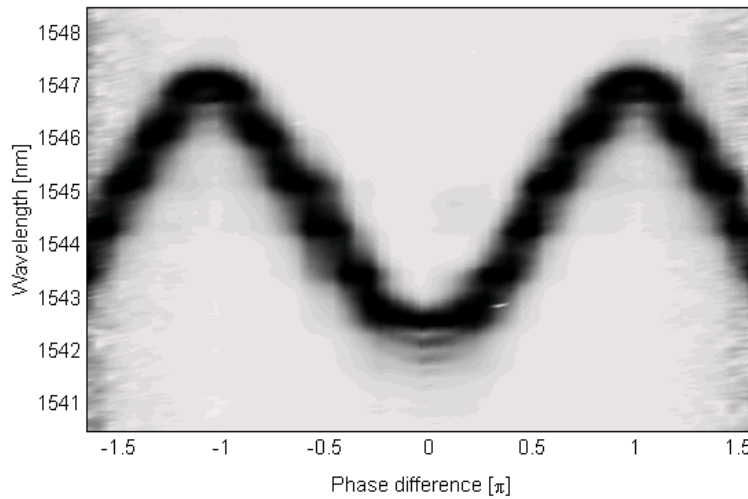


Figure 3.14 Dependence of the SH power versus the FH input wavelength and tilt of FH input beam for Pb344z sample.

The SHG efficiency was measured on the witness channels using the same HP tunable laser for internally controlled square-pulse modulation with a repetition rate of 1 kHz. A circular beam was launched into the witness channels and output measured separately on Ge (for the FH) and Si (for the SH) diodes working as current sources. Using lock-in techniques it was possible to detect SH powers at nW levels. In order to assure low depletion regime, low input powers were used and the FH wavelength was scanned around the resonance in order to register the total

shape of the SH tuning curve for comparison with a theoretical one. Finally power calibration was made at the peak of SHG using an Ophir power meter.

Figure 3.15 shows the edge channels (channels #'s 1 and 8, see Figure 3.9) SH tuning curves of the best samples Pb344z and Pb381z. The first one exhibits a nearly theoretical (sinc^2 -like) shape with multiple small secondary maxima on the low wavelength side which can be explained by the existence of a non-uniform wavevector mismatch condition along the waveguide [79]. There is a small shift (0.3 nm) in the positions of the main maxima and negligible SHG efficiency difference observed between the measurements in sample Pb344z. For the second, weakly coupled sample Pb381z, the SH tuning curves are not as good – clearly the sample has a serious problem with uniformity of the phase-matching profile. Also the shape and efficiency is significantly different for first and eight witness channels.

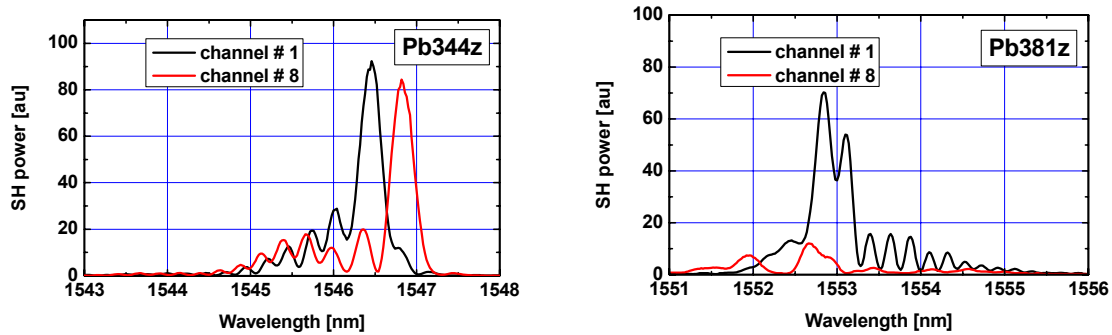


Figure 3.15 SH tuning curves for the edge witness channels for the two best samples: Pb344z and Pb381z at temperature of $T = 195^\circ\text{C}$.

To estimate the quality of the QPM grating a spatially resolved SHG experiment, which geometry and results shown in Figure 3.16, was performed. A narrow ($50\div 60 \mu\text{m}$ FWHM) FH beam was launched at an angle for which the beam experiences no spreading (diffraction, see

Chapter 2) as it crosses the array (relative phase angle $\pi/2$). The FH input wavelength was scanned around the SHG resonance and the SH output image was measured on a Si CCD camera. Because the SH is not coupled between channels and once generated in a given channel can only propagate straight along that channel, the registered picture (Figure 3.16 on the right) resembles the wavevector mismatch condition along the propagation direction. In the case of the Pb381z sample, for which results are shown in Figure 3.16, the QPM non-uniformity is quite severe (spreads in range of 3 nm), restricting the useful region of wavevector mismatch for investigation in the experiment.

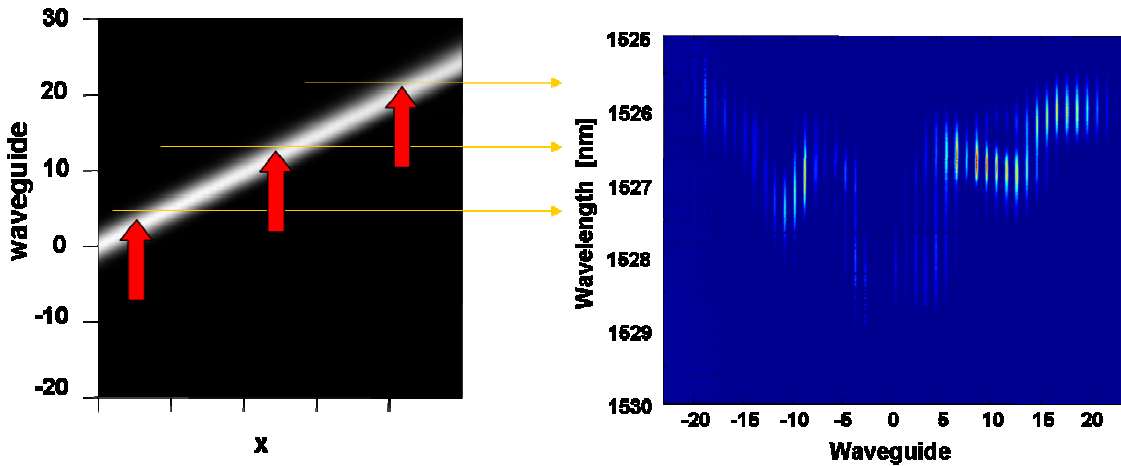


Figure 3.16 Geometry of the spatial resolved SHG experiment (on the left) and result of two measurements taken for two diffractionless angles ($-\pi/2$ and $\pi/2$) for the Pb381z sample at room temperature.

Table 3.4 and Table 3.5 list basic parameters of the Pb344z and Pb381z samples obtained during the characterization. Arrays # 3 and 4 from Pb344z sample were not fully characterized as their inter-channel linear coupling was too strong and they were never used in any experiment.

Table 3.4 Summary of the experimentally measured basic parameters for the Pb344z sample.

Pb344z sample	Array # 1	Array # 2	Array # 3	Array # 4
Length [mm]	51	51	51	51
Period [μm]	13.5	13.0	12.5	12.0
Loss @ $\lambda = 1550\text{nm}$ [$\text{dB}\cdot\text{cm}^{-1}$]	0.16	0.23	0.15	0.25
Coupling length @ $\lambda = 1550\text{nm}$ [mm]	6.08	4.74	–	–
Coupling constant @ $\lambda = 1550\text{nm}$ [m^{-1}]	260	330	–	–
PM wavelength @ $T = 20^\circ\text{C}$ [nm]	1521.3	1521.0	–	–
PM wavelength @ $T = 195^\circ\text{C}$ [nm]	1546.3	1546.2	1546.3	1546.4
SHG efficiency η_n [$\%\text{W}^{-1}$]	160	120	160	150
SHG efficiency η_l [$\%\text{W}^{-1}\text{cm}^{-2}$]	6.2	4.61	6.2	5.8

Table 3.5 Summary of the experimentally measured basic parameters for the Pb381z sample.

Pb381z sample	Array # 1	Array # 2	Array # 3	Array # 4
Length [mm]	71	71	71	71
Period [μm]	16.0	15.0	14.5	14.0
Loss @ $\lambda = 1550\text{nm}$ [$\text{dB}\cdot\text{cm}^{-1}$]	0.30	0.20	0.15	0.30
Coupling length @ $\lambda = 1550\text{nm}$ [mm]	25.56	15.74	12.16	9.53
Coupling constant @ $\lambda = 1550\text{nm}$ [m^{-1}]	61	100	129	165
PM wavelength @ $T = 20^\circ\text{C}$ [nm]	1527.6	1527.4	1527.1	1527.1
PM wavelength @ $T = 195^\circ\text{C}$ [nm]	1553.0	1553.1	1552.8	1552.7
SHG efficiency η_n [$\%\text{W}^{-1}$]	180	160	100	170
SHG efficiency η_l [$\%\text{W}^{-1}\text{cm}^{-2}$]	3.57	3.17	1.98	3.37

CHAPTER FOUR: EXPERIMENTAL SYSTEM

4.1. Sources

The transparency region of lithium niobate is wide, covering the range of 325-4500 nm [66]. Although experiments could have been performed at arbitrary sets of fundamental and second harmonic wavelengths lying in this region, the choice to work at the telecommunication wavelength is preferable because of possible future applications in this field. Four different laser systems were used in the experiments described in this dissertation, all of them covering the C communications wavelength band (1525-1565 nm).

4.1.1. Tunable Agilent HP81680A CW diode laser

This diode laser was mostly used for linear and nonlinear sample characterization at low fundamental depletion. It is an InGaAsP tunable laser with a built-in wavelength control loop to ensure high wavelength accuracy. Its narrow bandwidth and computer-based interface makes it perfect for the automated sample characterization. The internal amplitude modulation option, together with lock-in detection techniques, allows low-noise low-power measurements. Table 4.1 lists the most important parameters of the HP81680A diode laser [80].

Table 4.1 Main parameters of HP 81680A diode laser.

Wavelength range	1456-1584nm
Max. CW output power	≥ 5dBm (1520-1570nm)
Wavelength resolution	0.1pm (1550nm)
Absolute wavelength accuracy	0.01nm
Power flatness	0.3dB
Effective linewidth	50MHz

4.1.2. Burleigh FC-120 Color Center Laser

This laser, doubled externally with a PPKTP crystal, was used in parametric switching experiments. The Burleigh FC-120 is a $\text{NaCl:OH}^-(\text{F}^{2+}:\text{O}^{2-})$ Color Center Laser [81-83] synchronously pumped by a Coherent Antares 76 Nd:YAG laser. By varying the cavity length, this laser operates either in a mode-lock configuration, producing 7-9 ps pulses with up to 500 W peak power at 76 MHz repetition rate, or by destroying the mode-lock condition in a quasi-CW configuration. It is tunable from 1480 to 1660 nm. The CCL performance was monitored in real time using a scanning Burleigh TL series Fabry-Perot etalon. In the pulsed regime, the pulse duration was measured with a Femtochrome FR-103 SHG autocorrelator and the spectrum was monitored with a fiber-coupled Instrument System SPECTRO 320 spectrometer.

Table 4.2 Main parameters of Burleigh FC-120 color center laser.

Wavelength range	1480÷1660nm
Repetition rate	76MHz
Pulse duration	7-9ps
Spectral bandwidth	transform limited 0.30-035nm
Peak power	500W

4.1.3. Fiber-based system

Unfortunately the CCL alone could not deliver enough peak power for soliton experiments in the PPLN samples described in Chapter 3. The prospective replacement of the CCL had to fulfill a few key parameters restricted by the sample properties. The length of the samples determined from the SHG acceptance bandwidth of the device was calculated to be $0.2\div 0.3$ nm theoretically. Because efficient SHG is desired over the full channel length, the bandwidth of the source should be comparable with the SHG bandwidth. For the optimum case of transform limited pulses, a 0.25 nm bandwidth corresponds to 10 ps long pulses. Another consideration determining the pulse width is the walk-off between the FH and the SH over the sample length due to their different group velocities. Theoretically the pulses walk-off by 13 ps for a 7 cm long single channel. Thus ideally pulses of minimum 10 ps (preferable 20 ps) are desired. Also the peak power was an important issue – theoretical calculations showed that the minimum required power for the soliton excitation on phase-match is of order of few hundreds Watts. Off phase-match, the required power scales approximately linearly with the phase-mismatch. Given the losses in a typical beam shaping system, the target was to achieve 4 kW peak power. Secondary but still important requirements were the pulse-to-pulse stability and the source's repetition rate. The first relates to the reproducibility of the results and the second to the signal-to-noise ratio of the detection system. Based on previous experience, these parameters were set at a minimum of 1 MHz repetition rate and pulse-to-pulse stability better than 5%. No commercial system, fulfilling all requirements, was available on the market. That is why a home-built fiber based system was designed, built and characterized for these experiments.

Originally the fiber system was proposed to consist of 2 parts, a picosecond fiber laser and large-core Erbium doped fiber amplifier (EDFA). A commercial large-core EDFA was purchased from Keopsys. It consisted of two amplifier stages: preamplifier with the average output of 10 mW and a booster with the maximum average power output of 500 mW. The CCL was used to test the amplifier (see Figure 4.1). A bulk electro-optic Conoptics M360-3 modulator was set up in the path of the laser beam in order to reduce the repetition rate of the laser, by an arbitrary integer factor N .

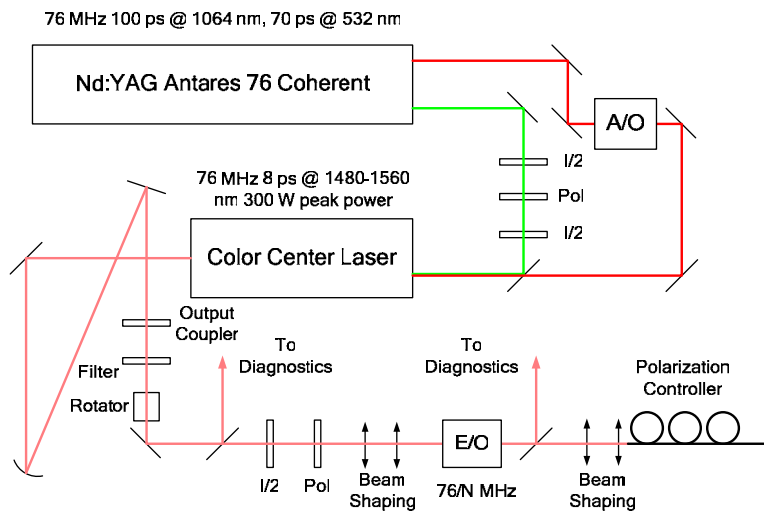


Figure 4.1 Large core Erbium doped fiber amplifier characterization setup.

At the repetition rate of 19 MHz (the closest value to the planned 20 MHz) a significant spectral broadening at the output from large core amplifier (see Figure 4.2 on the left) was observed starting at power levels of a few hundreds Watts, resulting from self phase modulation (SPM) in both the 1 m long SMF-28 fiber at the amplifier output and the Erbium doped fiber in the amplifier itself. The output fiber was cut to 15 cm. This improved but did not solve the problem as SPM persisted (see Figure 4.2 on the right). It was decided to use a pulse stretcher

before the amplifier to reduce the peak power intensity (and hence the spectral broadening due to SPM). The amplifier then amplified the pulse energy and a pulse compressor was used in the last stage to recover the peak power. This is basically the well known Chirped Pulse Amplification (CPA) technique [84]. Although the stretcher could be fiber-based because the input peak power of a few Watts is insufficient to produce spectral broadening, the pulse compressor outputs intensity levels which would produce significant spectral broadening in a compression fiber. Thus the compression stage requires a bulk system involving bulk gratings. Figure 4.3 shows the designed CPA system consisting of four discrete elements: picosecond fiber laser, chirped fiber Bragg grating (CFBG), large-core EDFA and bulk grating compressor.

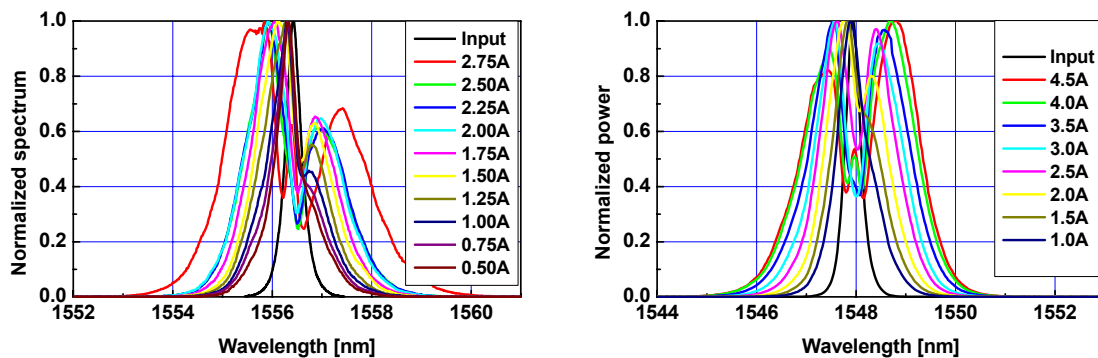


Figure 4.2 Spectral broadening at the output of the amplifier due to self phase modulation: before (on the left) and after (on the right) shortening the output fiber as a function of pumping diode current. 2.75 A corresponds to 2.5 kW optical peak power at the output.

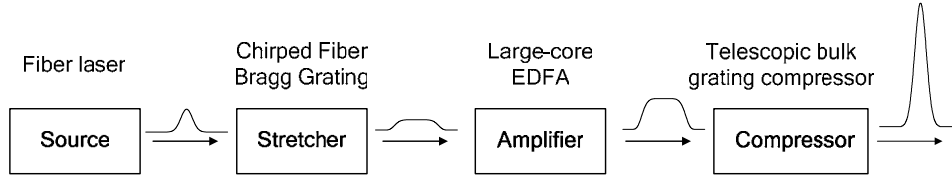


Figure 4.3 Application of Chirped Pulse Amplification technique to the fiber based system.

A number of custom-made chirped fiber gratings for the pulse stretching phase were fabricated using the photosensitive-laser writing method by Dr. Ian Bennion’s group at Aston University in the UK and characterized. The reflection properties were measured using the setup shown in Figure 4.4 on the left and the results are presented on the right. These are typical reflection results showing that the output from the long wavelength input end of the fiber exhibits a slope due to the wavelength-dependent coupling into the cladding modes. It is this spectral bandwidth of the grating which limits the tuning range of whole system to 7 nm.

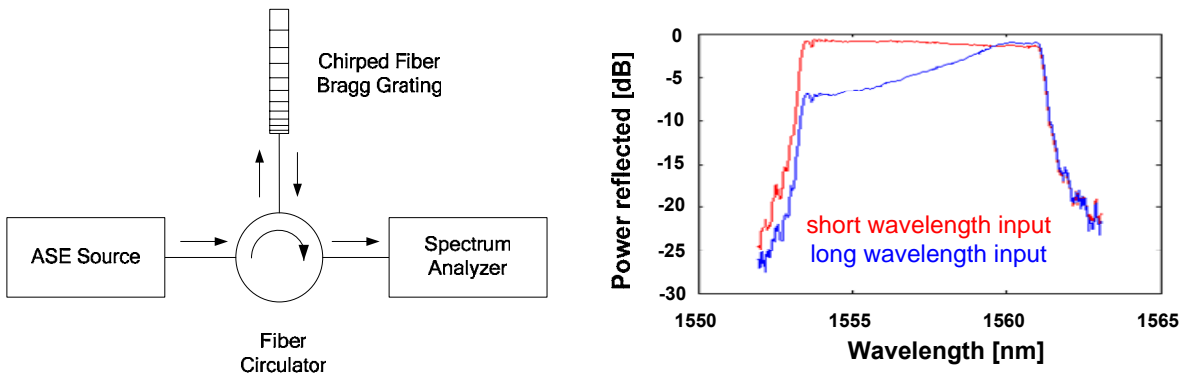


Figure 4.4 Characterization of reflection of chirped fiber Bragg grating: setup (on the left) and results for inputs into both ends (on the right).

Second order dispersion of the fiber grating was measured, using the broad-band interferometric setup [85, 86] shown in Figure 4.5, to be 120 ps/nm, which limits the stretched pulse to 45÷50 ps.

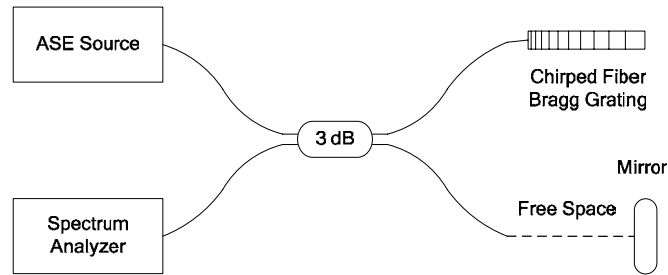


Figure 4.5 Second order dispersion characterization setup.

The previously tested large-core EDFA was used to amplify the stretched pulses. Different repetition rates were tested and, based on output peak power, spectral broadening and the amplified spontaneous emission content, an optimum 4.75 MHz repetition rate was chosen. The estimated peak output power of 2 kW (intensity of 3 GW/cm^2 assuming a mode diameter of $9.2 \text{ }\mu\text{m}$) was too low to produce a significant spectral broadening in the amplifier. In fact, depending on which input end of the fiber Bragg grating was used, the output spectrum was a bit wider (for input at the long wavelength end) or a bit narrower (for input at the short wavelength end) than the input spectrum. This variation is indicative of a small amount of residual SPM in the amplifier. If the input pulse is positively chirped, the spectrum broadens during propagation in the amplifier due to SPM. On the other hand, a negative chirp causes initially a spectral narrowing near the input and some distance down the fiber a subsequent spectral broadening as in the previous case. The second case matched better the requirements of the desired source because it produced marginally longer pulses. Figure 4.6 shows experimentally measured input and output spectra for a negatively chirped input pulse.

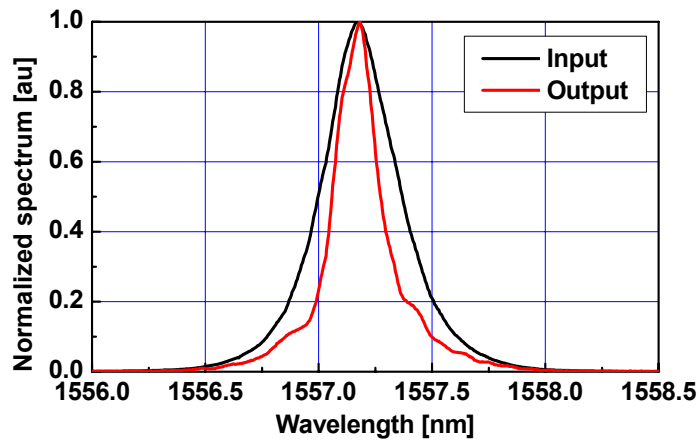


Figure 4.6 Input and output spectra for an initially negatively chirped pulse.

The last stage of the system, the bulk grating compressor [87], was based on the design of the stretcher in the Spitfire – regenerative amplifier by Spectra-Physics (see Figure 4.7).

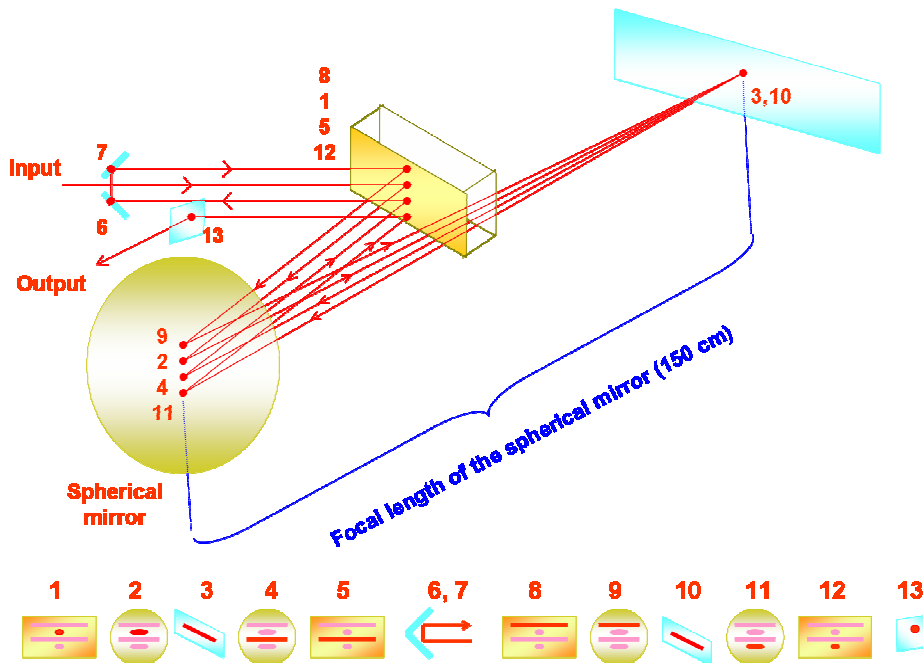


Figure 4.7 Compressor layout based on the Spectra-Physics design with the beam output at various positions shown.

It is a folded version design of the telescopic version proposed first by Martinez [88] in which a negative chirp can be compensated. A high modulation holographic reflective grating with 1100 grooves/mm was purchased from Thermo Richardson Grating Laboratory. Figure 4.8 shows the variation in efficiency of coupling to the first diffracted order with deviation from the Littrow angle of 58° . Although the angles have to be adjusted for wavelength changes, the grating efficiency is $> 90\%$ over hundreds of nm.

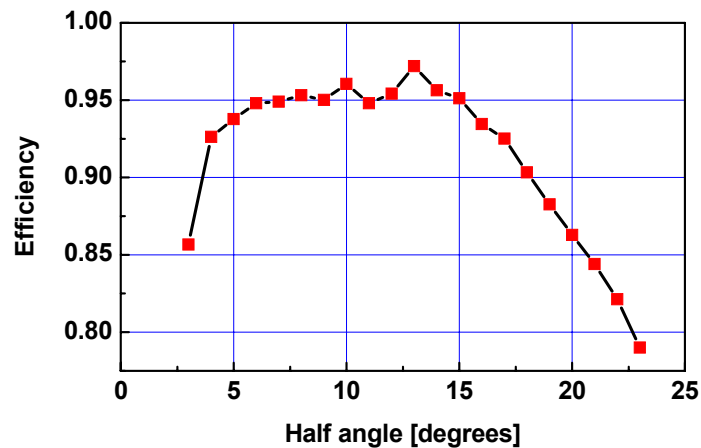


Figure 4.8 Efficiency of coupling to the first diffracted order as a function of the angular deviation from the Littrow angle.

A 2 inch diameter silver coated concave mirror with 3 m radius of curvature was used in the setup as the focusing element. The distance between the concave mirror and grating was 50 cm, which yields an effective grating separation (for a standard non-folded design) of 2 m. After achieving successful compression (autocorrelation indicated 13 ps FWHM) based on the CCL input, that laser reached the end of its useful life and died.

Next a custom designed fiber laser, with the parameters shown in Table 4.3, was purchased from Pritel. It is a linear cavity, passively mode-locked laser producing nearly transform-limited 9-11 ps long pulses.

Table 4.3 Main parameters of the Pritel picosecond fiber laser.

Wavelength range	1535-1565nm
Repetition rate	5MHz
FWHM pulse duration	9-11ps depending on wavelength
FWHM spectral bandwidth	0.28-0.38nm, close to transform limit
Average power	3-5mW

It was expected that small differences in seeding pulse parameters, between the CCL and Pritel fiber laser, would result in different amplified pulses because of weak but still present nonlinear effects. A non-collinear SHG Frequency Resolved Optical Gating (FROG) [89, 90] setup (see Figure 4.9) was built and used to characterize the pulse quality after compression. To control the relative delay of the pulses in two arms, a prism in one of the arms was placed on motorized stage. A high resolution fiber coupled ANDO AQ-6315E spectrum analyzer was used to collect the spectral data. A LabVIEW program was developed to synchronize these two pieces of equipment to ensure good quality of the data.

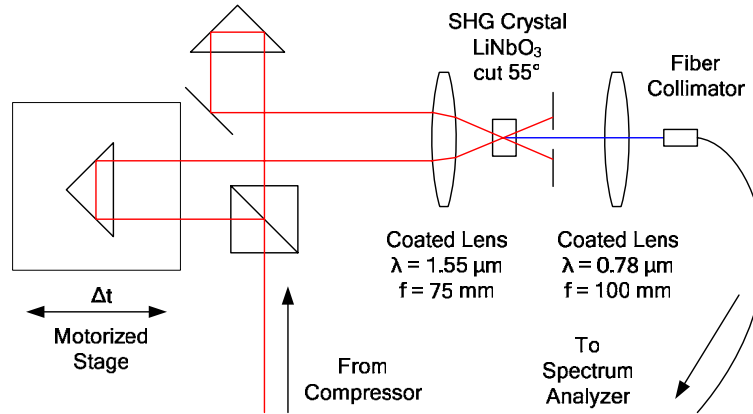


Figure 4.9 SHG frequency resolved optical gating setup used to characterize pulses from the fiber based system.

A comparison of the FROG traces (see Figure 4.10), taken for two different values of pumping currents of the diode in the booster stage of the amplifier: $I_{d2} = 1.0$ A and $I_{d2} = 5.0$ A, confirms that there is still some SPM present in the amplification process at the higher current settings. As there was no commercial software available for pulses longer than 1ps, a pulse retrieval program was developed in Matlab based on a generalized projection method [91-93].

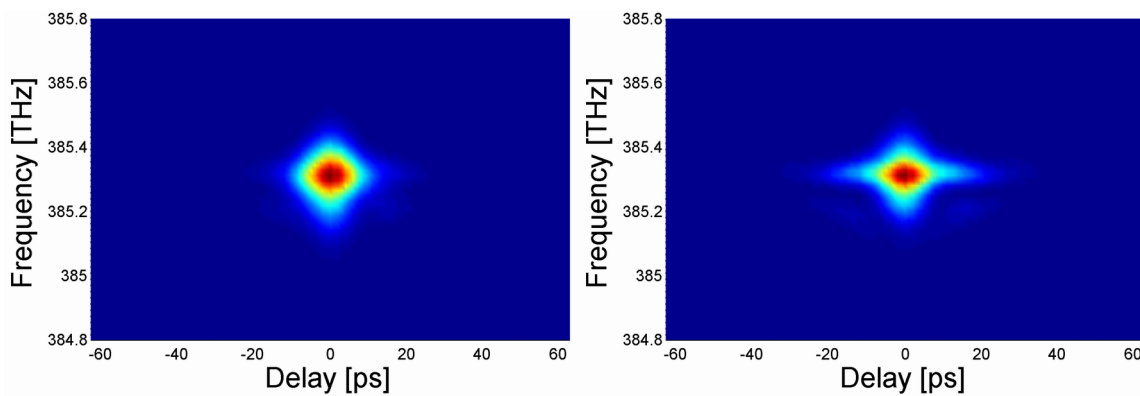


Figure 4.10 SHG frequency resolved optical gating traces for two different settings of pumping currents of booster stage diode: $I_{d2} = 1.0$ A on the left and $I_{d2} = 5.0$ A on the right.

The pulse amplitudes and phases retrieved from the FROG for different pump diode currents are shown in Figure 4.11. The pulses are a slightly asymmetric and the best fit to a sech function gives a FWHM of 7.65 ps for a pumping diode current of $I_{d2} = 5.0$ A. To check the reliability of the FROG measurements the autocorrelation and the power spectrum were calculated from the retrieved pulses, for the two different pumping currents, and compared with the measured ones (see Figure 4.12). The agreement is excellent and small differences come from the resolution of the equipment used.

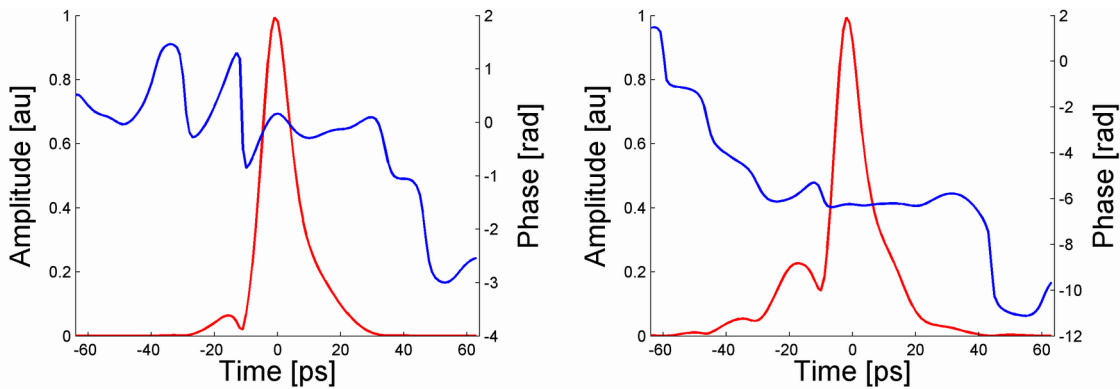


Figure 4.11 The retrieved pulse amplitudes and phases for two different settings of the diode's pumping current (booster stage diode): $I_{d2} = 1.0$ A on the left and $I_{d2} = 5.0$ A on the right.

It would be an interesting problem to investigate the nonlinear dynamics during amplification and its influence on the pulse shape but this was not the topic of this dissertation and further improvements were not necessary to perform nonlinear experiments in the waveguide array samples. Table 4.4 lists the most important output parameters of fiber based system.

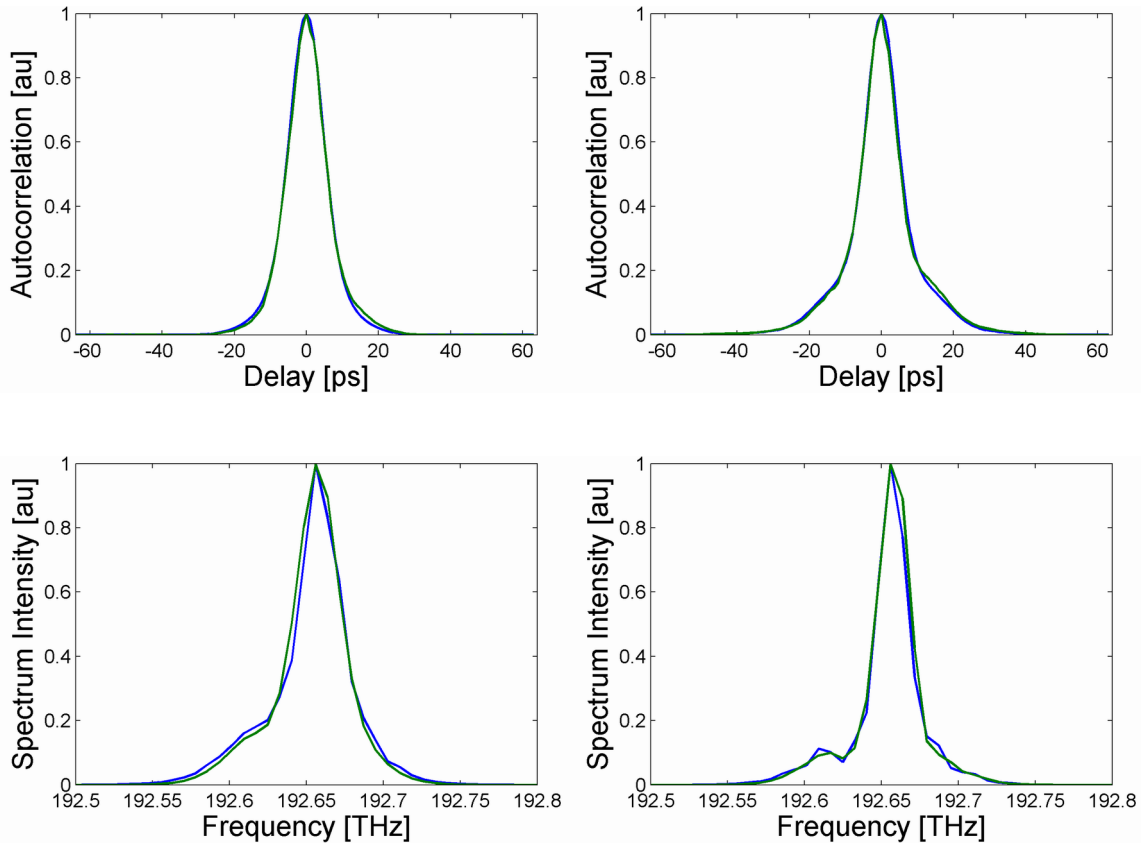


Figure 4.12 Comparison of measured (green) with calculated from the retrieved pulses (blue) autocorrelation (first row) and power spectrum (second row) for two different settings of the pumping currents of the booster stage diode $I_{d2} = 1.0$ A (on the left) and $I_{d2} = 5.0$ A (on the right).

Table 4.4 Main parameters of fiber based system.

Wavelength range	1554±1561nm
Repetition rate	5MHz
FWHM pulse duration	7.65ps
FWHM spectral bandwidth	0.22nm
Peak power	4.5kW

4.1.4. Ekspla PG501VIR OPG-OPA system

This system was used in the modulational instability experiment. It is a commercial system consisting of two modules: a passively mode-locked picosecond Nd:YAG laser (Ekspla PL2143A) as a pump source and a OPG-OPA unit (Ekspla PG501VIR) [94, 95]. The Nd:YAG laser has two outputs: 1064 nm fundamental output with maximum pulse energy of 25 mJ and extra-cavity doubled 532 nm output with energy up to 11 mJ – both delivering 25 ps long pulses at repetition rate of 10 Hz. The green 532 nm output is used to pump the OPG-OPA unit which is tunable from 680-2300 nm. The average output energy is wavelength dependent and higher than 0.2 mJ. The output energy stability of the unit (usually around 10% rms) is mainly influenced by the pump laser stability (usually below 1.5%). The bandwidth of the source is around 0.5 nm at wavelength 1550 nm. Thus the time-bandwidth product, for measured 15 ps long pulses, is four times the transform limit. The spatial quality, in comparison with the previously described system, is not very good. Moreover there are some problems related with beam pointing stability due to nonlinear instabilities in the parametric interaction.

Table 4.5 Main parameters for the Ekspla OPG-OPA system.

Wavelength range	680÷2300nm
Repetition rate	10Hz
FWHM pulse duration	15ps
FWHM spectral bandwidth	0.5nm
Pulse energy	> 0.2mJ

4.2. Power Measurements

The laser sources described in this chapter can be divided, with respect to different methods of power detection, into two groups: CW or quasi-CW sources (when the response of the detector is much slower than the repetition rate of the source) for which an average power is measured, and low repetition rate sources where pulse energy is measured. The average power and pulse energy detection methods used in the experiments described in this thesis are discussed below separately.

4.2.1. CW and high repetition rate systems

Two commercial, calibrated power meters for measuring power were available. A Coherent LaserMate thermal detector with digital readout was used to measure average power levels between 1 mW and 10 W. An Ophir InGaAs detector PD-300-IRG (power range 1 pW-300 mW for the FH) and a Silicon detector PD-300 (power range 1 nW-300 mW for SH) were used with digital LaserStar readout to measure low average output powers.

In order to increase the number of points at which the power is monitored in the experiment, Ge (for FH) and Si (for SH) photodiodes connected to EG&G 5209 lock-in amplifiers were used. The detected current from the photodiodes was read out by a computer and (after calibration against the Ophir power meter) converted directly to optical power. Care has been taken to ensure that these detectors do not work in the saturation regime due to high peak powers. Silicon polished plates were placed in front of the Ge photodiodes (for the FH detection) and KG3 filters in front of the Si photodiodes (for the SH detection) to prevent cross-talk between the FH and SH wavelengths. When working with a CW HP81680A diode laser an internal modulation of 1 kHz was used as the reference frequency for the lock-in amplifier. For

high repetition rate systems, a mechanical chopper with a duty cycle of 1:10 was placed in the path of the beam and rotated at 60 Hz frequency in order to avoid frequency beating phenomena on cameras.

4.2.2. Low repetition rate system

A Laser Precision Corporation pyro-electric PjP-735 head was used with a digital Rj7100 readout to measure pulse energy when using the low repetition Ekspla system. Additional power measuring points were setup with the help of Ge (for the FH) and Si (for the SH) photodiodes, calibrated against the Laser Precision Corporation energy meter, and commercial Stanford Research boxcar integrator system. On-demand data transfer was available through the GPIB bus. Again Si plates and KG3 filters were used to avoid the cross-talk between the FH and the SH.

4.3. Cameras

Observation of the spatial power distribution at the sample output required cameras responding to the FH and SH wavelengths. For the FH, a Hamamatsu C2070 Vidicon camera was used. A silicon plate was placed in front of the camera to block SH radiation as its sensitivity also covers the SH wavelength. For the SH a Pulnix TM-745 CCD Silicon camera was used, gen-locked to the horizontal synchronization signal of the Hamamatsu camera. Pictures from both cameras were acquired at 30 frames-per-second by a computer program written in LabVIEW. In the “highly localized” soliton experiment, a third camera, an ElectroPhysics MicronViewer 7290A Vidicon camera, was used to measure the relative phase changes of the SH seed.

For the modulational instability experiment when the average FH power was very low and the Hamamatsu camera was not sensitive enough, a Roper Scientific OMA V InGaAs line camera (512x1 pixels) was used.

CHAPTER FIVE: DISCRETE TALBOT EFFECT

The repeated self-imaging in space of a diffraction grating on propagation in a continuous medium was first observed by Talbot [96] in 1836. A few decades later Lord Rayleigh explained this remarkable effect by showing that any periodic one-dimensional field pattern reappears, upon propagation, at even integer multiples of the so-called Talbot distance $x_T = L^2 / \lambda$, where L represents the spatial period of the pattern and λ the light wavelength [97]. The question arises as to whether the Talbot effect is also possible in discrete systems. Unlike in continuous media where the dispersion relation (of the paraxial Fresnel or Schrödinger equation) is parabolic, in discrete systems the dispersion curve has a cosine-like character (see Figure 2.7). Does this difference affect the Talbot effect in discrete media?

In this chapter the theory and experimental observation of discrete Talbot effects in weakly coupled waveguide arrays will be presented [32].

5.1. Overview of Talbot effect in continuous media

The phenomenon of Talbot self-imaging is caused by Fresnel diffraction of a grating in its near field [98-100]. Because there are interesting differences in diffraction between continuous and discrete media, the well-known continuous case will be briefly reviewed first. It can easily be derived using the 1D wave propagation equation for a wave propagating along x , and diffracting in the y direction

$$i \frac{\partial \varphi}{\partial x} + \frac{1}{2k} \frac{\partial^2 \varphi}{\partial y^2} = 0 \quad (5.1)$$

where φ represents the complex field amplitude. There is a corresponding equation in the Fourier domain,

$$i \frac{\partial \Phi}{\partial x} - \frac{\zeta^2}{2k} \Phi = 0, \quad (5.2)$$

where the amplitudes in the space and Fourier domains are related by the following transformations

$$\begin{aligned} \Phi(\zeta) &= \int \varphi(y) e^{-i\zeta y} dy \\ \varphi(y) &= \frac{1}{2\pi} \int \Phi(\zeta) e^{i\zeta y} d\zeta \end{aligned} \quad (5.3)$$

In general a periodic input pattern can be represented by a Fourier series in the space domain

$$\varphi_0(y) = \sum_{n=-\infty}^{\infty} c_n e^{i \frac{2\pi}{L} y} \quad (5.4)$$

which in Fourier space corresponds to

$$\Phi_0(\zeta) = F\{\varphi_0(y)\} = \sum_{n=-\infty}^{\infty} \int_{-\infty}^{\infty} c_n e^{i \left(\frac{2n\pi}{L} - \zeta \right) y} dy = 2\pi \sum_{n=-\infty}^{\infty} c_n \delta \left(\zeta - \frac{2n\pi}{L} \right). \quad (5.5)$$

For a propagation distance x in Fourier space using the paraxial approximation

$$\Phi(\zeta, x) = e^{-i \frac{\zeta^2}{2k} x} \Phi_0(\zeta) = e^{-i \frac{\zeta^2}{2k} x} 2\pi \sum_{n=-\infty}^{\infty} c_n \delta \left(\zeta - \frac{2n\pi}{L} \right), \quad (5.6)$$

the inverse Fourier transform results in a final output pattern of the form

$$\varphi(y, x) = F^{-1}\{\Phi(\zeta, x)\} = \sum_{n=-\infty}^{\infty} c_n \int_{-\infty}^{\infty} e^{-i \frac{\zeta^2}{2k} x} \delta \left(\zeta - \frac{2n\pi}{L} \right) e^{i\zeta y} d\zeta = \sum_{n=-\infty}^{\infty} c_n e^{i \frac{2n\pi}{L} y} e^{-i \left(\frac{2n\pi}{L} \right)^2 \frac{x}{2k}}, \quad (5.7)$$

which can be compared with the input distribution $\varphi_0(y)$. Perfect re-imaging requires that the second exponential term be equal to 1. This results in the following condition for the Talbot distance

$$x_T = m \frac{L^2}{\lambda} \quad (5.8)$$

where m is an integer.

In addition to the integer Talbot effect, fractional revivals are also known to occur at distances that are rational multiples of x_T , i.e., $x/x_T = p/q$ where p and q are relatively prime integers. In fact, as shown in several studies, these fractional Talbot images consist of q coherently superimposed and equally spaced copies of the initial image with a complex phase relation [98, 101]. In Figure 5.1 some fractional 1D intensity images are shown for multiples of a quarter of the Talbot distance for a 50% duty cycle amplitude grating. The initial pattern with most of the power centered at $y/L = 0$ undergoes diffraction and at the distance $x = x_T$ is centered at $y/L = 0.5$. This cycle continues and at $x = 2x_T$ the pattern looks exactly like the input one.

On the other hand, if x/x_T happens to be irrational, the resulting image is fractal in nature, i.e. the structure of the image is very complex as the number of superimposed copies creating the image is infinite. This interesting relationship between the Talbot effect and number theoretic issues has been recently suggested as a possible way to factorize integers [102].

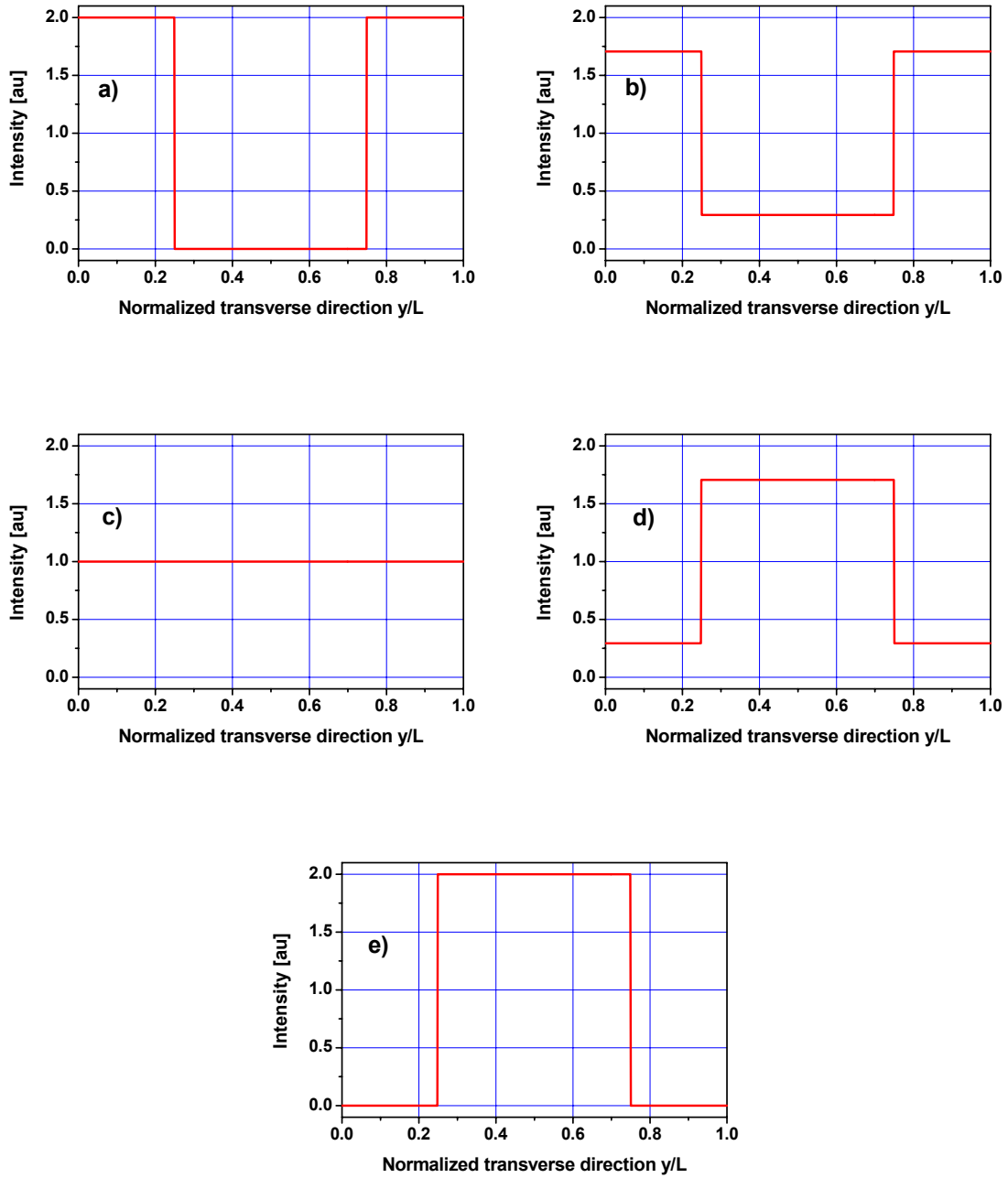


Figure 5.1 One-dimensional fractional Talbot patterns for: a) $x = 0$ or $2x_T$, b) $x = x_T/4$ or $7/4x_T$, c) $x = x_T/2$ or $3/2x_T$, d) $x = 3/4x_T$ or $5/4x_T$, e) $x = x_T$.

In the last few years, there has been a renewed interest in optical Talbot effects because of possible applications, not only in the spatial [103, 104] but also in the temporal domain (in

optically dispersive fibers) [105]. In addition to optics, Talbot recurrences have been encountered in many other areas of physics such as in atom optics [106], Bose-Einstein condensates [107], and in the interferometry of large C_{70} fullerene molecules [108]. Generally speaking, the Talbot process belongs to a broader family of phenomena exhibiting wave packet revivals [109]. Revivals of this sort can occur for example in the generation and detection of atomic Rydberg electron wave packets [110], in molecular systems [111], in quantum billiards and carpets [109, 112], during Bloch oscillations [113, 114], and in systems described by the Jaynes-Cummings model [109] just to mention a few. Yet, so far, the Talbot process has only been investigated in continuous systems using either the Fresnel equation in optics or its mathematically equivalent Schrödinger equation in atom optics.

5.2. Theory of discrete Talbot effect

The theoretical analysis which follows indicates that Talbot recurrences only occur when the period N of the initial pattern belongs to the set $N \in \{1,2,3,4,6\}$. This is unlike to what occurs in the continuous Talbot process where the revivals are period independent.

To analyze the discrete Talbot effect, the wave propagation in an infinite array of weakly coupled discrete waveguides is described by the array's coupled wave equation [17]

$$i \frac{du_n}{dx} + C(u_{n-1} + u_{n+1}) = 0 \quad (5.9)$$

where u_n is complex field amplitude in the n -th channel and C is complex constant. As discussed in Chapter 2, Equation (5.9) is known to admit solutions of the form $u_n = u_0 e^{i(\Delta k_x x + n k_y d)}$ where $k_y d$ is a phase shift between successive sites and Δk_x is an eigenvalue given by

$\Delta k_x = 2C \cos(k_y d)$. For the Talbot effect to take place, the input field distribution should be periodic, and thus in general $u_{n+N} = u_n$ where N represents the spatial period of the input. Because of this periodic condition, $k_y d$ can only take values from the discrete set $k_y^m d = m\theta$ where $\theta = 2\pi/N$ and $m = 0, 1, 2, \dots, N-1$. Therefore as a result of this periodicity, the field evolution at site n can be in general described by expansion into a set of orthogonal functions $a_n^{(m)} = N^{-1/2} \exp(ink_y^m d) \exp(i\Delta k_x^m x)$, i.e. $u_n = \sum_{m=0}^{N-1} c_m a_n^{(m)}$. It is therefore clear that field revivals are possible at intervals x if $\Delta k_x^j x = 2\nu\pi$ (where ν is an integer) and hence the ratio of any two eigenvalues must be a rational number, i.e. $\Delta k_x^i / \Delta k_x^j = p/q$ where, p and q are relatively prime integers. From the ratio $\Delta k_x^1 / \Delta k_x^0$ one arrives at the conclusion that $\cos(2\pi/N)$ must also be rational for field revivals to occur. In addition, one can also directly show that the intensity patterns will repeat if the ratio $(\Delta k_x^\mu - \Delta k_x^\nu) / (\Delta k_x^i - \Delta k_x^j) = p/q$ is also rational, where the eigenvalue indices $\mu, \nu, i, j \in \{0, 1, \dots, N-1\}$ and are taken at least three at a time. By considering the ratio $(\Delta k_x^2 - \Delta k_x^0) / (\Delta k_x^1 - \Delta k_x^0)$ one can then reestablish the fact that $\cos(2\pi/N)$ should be rational. Therefore, for discrete Talbot revivals (field or intensity) to occur it is necessary that $\cos(2\pi/N) = p/q$, i.e. it is a rational number.

The question now is: for which values of N , is $\cos(2\pi/N)$ a rational number? This issue is addressed by observing the fact that all higher-order eigenvalues can be obtained from the first one using Chebyshev polynomials $T_m(\zeta)$, that is $\cos(m\theta) = T_m(\cos(\theta))$, where $\theta = 2\pi/N$, and $T_m(\zeta) = \sum_{k=0}^{[m]} c_k^{(m)} \zeta^{m-2k}$ where $[m]$ represents the integer part of m . All the Chebyshev coefficients $c_k^{(m)}$ are integer numbers and of importance to this discussion is the fact that the first

Chebyshev coefficient is given by $c_0^{(m)} = 2^{m-1}$. Given that $c_k^{(m)}$ are integers, then $\cos(2m\pi/N)$ is rational if and only if $\cos(2\pi/N)$ is rational. To find all possible N 's that will permit Talbot recurrences it is first assumed that N is odd. From the relation $T_N(\cos(\theta)) = \cos(N\theta) = 1$, one obtains the following polynomial in $\cos(\theta)$, $2^{N-1}(\cos(\theta))^N + \dots + c_{\lfloor N/2 \rfloor}^N \cos(\theta) - 1 = 0$. By applying the rational root theorem, the possible rational roots of this polynomial, if any, should belong to the set $\pm \{1, 1/2, 1/2^2, \dots, 1/2^{N-1}\}$. It turns out that these are indeed roots only if $N = 1, 3$. For $N = 5$, $\cos(2\pi/5) = (\sqrt{5} - 1)/4$ is irrational and in addition for any odd integer N greater than 6, it is expected that $1/2 < \cos(2\pi/N) < 1$. Since from the previous discussion this is impossible, then $\cos(2\pi/N)$ is rational for only $N = 1, 3$. By using similar techniques and a fundamental theorem of arithmetic (unique factorization theorem), one can then show that for even N , $\cos(2\pi/N)$ is rational only if $N = 2, 4, 6$. Thus one can formally show that discrete Talbot revivals are only possible for a finite set of periodicities. These belong to the set $N \in \{1, 2, 3, 4, 6\}$ where $N = 1$ represents the trivial case of a discrete plane-wave solution. For any other periodicity in general, the field evolution is non-periodic. This is in contrast to what happens in the continuous Talbot case where the recurrences happen to be period independent. Of course, for specific periodic inputs, it is also possible to have revivals even when N does not belong to the above mentioned set. This may happen in cases where only a subset of eigenvalues is involved (because of the input pattern) that happen to be rational with respect to each other.

Now some of the aspects associated with the discrete Talbot effect are going to be illustrated by means of relevant examples. Let us first assume a binary pattern at the input. More specifically, let $u_n = a_0 \exp(in\phi)$ for even n sites and $u_n = b_0 \exp(in\phi)$ for odd. In this case, one can show that the field in the even/odd elements evolves according to

$u_n = [(a_0, b_0) \cos(2Cx \cos(\phi)) + i(b_0, a_0) \sin(2Cx \cos(\phi))] \exp(in\phi)$. Figure 5.2 depicts periodic intensity revivals when the binary input is $[1, 0, 1, 0, \dots]$. The intensity Talbot “carpet” corresponding to this case is shown in units of coupling lengths $L_c = \pi/2C$. For this example where $b_0 = \phi = 0$ (shown in Figure 5.2a), the patterns reappear every L_c , i.e. the discrete Talbot distance is $x_T = L_c/2$. An interesting case arises when the array is excited at an angle (at a finite Bloch momentum) and thus the binary input is phase shifted according to $[e^{i\phi}, 0, e^{3i\phi}, 0, \dots]$ ($a_0 = 1, b_0 = 0$). From the previous discussion, one then finds that the discrete Talbot period is given by $x_T = L_c/(2 \cos(\phi))$. Figure 5.2b shows the same pattern but with a Bloch momentum equal to $\pi/4$. Indeed the Talbot x_T distance got shorter. It is interesting to note that as ϕ approaches $\pi/2$, the Talbot revivals slow down and totally disappear at $\phi = \pi/2$ as shown in Figure 5.2c. One may interpret this effect from the fact that the diffraction/dispersion of the array is zero in the middle of the Brillouin zone (at $\pi/2$) and so the Talbot process that derives from these effects vanishes.

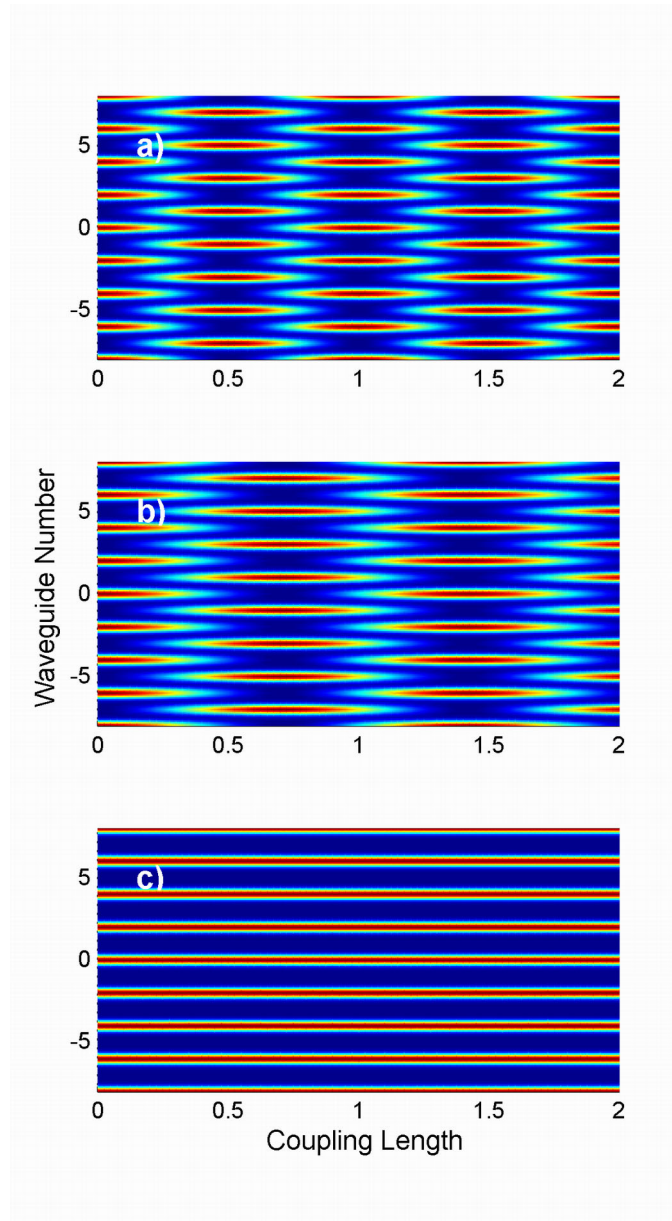


Figure 5.2 Talbot intensity "carpets" for input field pattern $[1, 0, 1, 0, \dots]$ and different Bloch momentum ϕ : a) 0 , b) $\pi/4$, c) $\pi/2$.

Figure 5.3 shows additional Talbot intensity "carpets" for the input periodic patterns $[1, 0, 0, 1, 0, 0, \dots]$ which has a period $N = 3$ and $[1, 0, 0, 0, 1, 0, 0, 0, \dots]$ with a period $N = 4$, both excited in-phase. In the first case the intensity in the initially excited channels evolves according

to $(5+4\cos(3Cx))/9$ whereas in the channels that were not excited at the input it varies like $(2/9)(1-\cos(3Cx))$. For this pattern the Talbot period is given by $x_T = 4L_c/6$. In general for $N \in \{1,2,3,4,6\}$ and for in phase excitations, the Talbot recurrence distance is given by the largest period $x_T = \pi/(\Delta k_x^i - \Delta k_x^j)$ that results from the eigenvalues involved in the initial pattern.

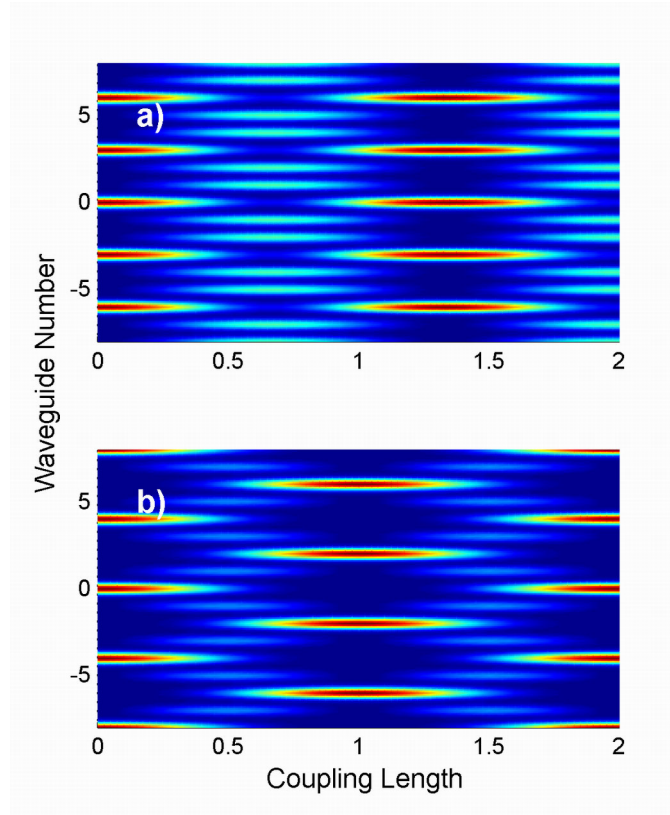


Figure 5.3 Talbot intensity "carpets" for different in-phase input field patterns: a) [1, 0, 0, 1, 0, 0, ...] and b) [1, 0, 0, 0, 1, 0, 0, 0, ...].

5.3. Setup and experimental results

For an experimental demonstration of discrete Talbot effects, array # 2 of the Pb381z sample with coupling length of 15.74 mm at $\lambda = 1550$ nm was used (see Table 3.5 for details).

The inter-channel coupling length was measured experimentally as a function of wavelength (results shown in Figure 3.12 in green). In the experimental setup (see Figure 5.4) a HP81680 tunable diode laser was used as the source. The laser output beam was shaped, using a telescope based on two cylindrical lenses C1 and C2 to be highly elliptical and was focused by a 10X microscope objective to a size of $500 \times 3.5 \mu\text{m}$ FWHM on the input facet of the array sample. Amplitude transmission masks, with periodicities that are multiples of the array inter-channel spacing and exhibiting different patterns, were fabricated using laser writing and etching techniques. The masks were then put in contact with the sample for clean in-phase mode excitation.

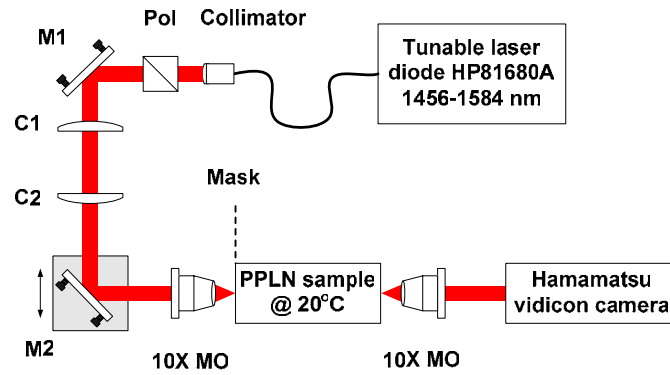


Figure 5.4 Experimental setup.

To control the tilt of the input beam and hence the initial phase difference between adjacent channels, a mirror M2 was placed on a motorized stage between the telescope and the microscope objective. The horizontal displacement of the beam from the center of the microscope objective caused a beam tilt at the input facet of the sample. Because of the sample's excellent linear properties (low scattering) it was not possible to observe the Talbot revivals when looking from the top. Instead, an indirect observation of the Talbot process at the output of

the array was achieved by varying the wavelength (and hence the coupling length) over the full spectral range of the laser (1456-1584 nm). This change in coupling strength with wavelength is essentially equivalent to varying the effective sample length. This in turn allows one to observe the Talbot effect without affecting the diffraction properties of the beam.

The experimental results corresponding to the periodic [1, 0, 1, 0, ...] excitation conditions with different Bloch momentum (simulated in Figure 5.2) are shown in Figure 5.5a-c respectively. These figures depict the intensity at the output of the array as a function of wavelength, in good agreement with theory. In Figure 5.5a, a Talbot recurrence and an intermediate state (at $(1,3)L_c/4$) where all elements are equally excited, was observed. On the other hand, as per our previous discussion, in Figure 5.5c this periodic recursion disappears since the phase difference between successive waveguides is $\pi/2$. Similarly, Figure 5.6 demonstrates Talbot revivals when the initial patterns have a period $N = 3$ and $N = 4$. Both sets of results are in very good agreement with simulations presented in Figure 5.3. The “wavy” nature of the observed patterns is a consequence of the wavelength tuning. This introduces wavefront aberrations at the input facet due to the chromatic dispersion in the optical elements that leads to focal point shifts with wavelength. This results in a very weak excitation of higher order bands which interfere with the lowest order band of interest.

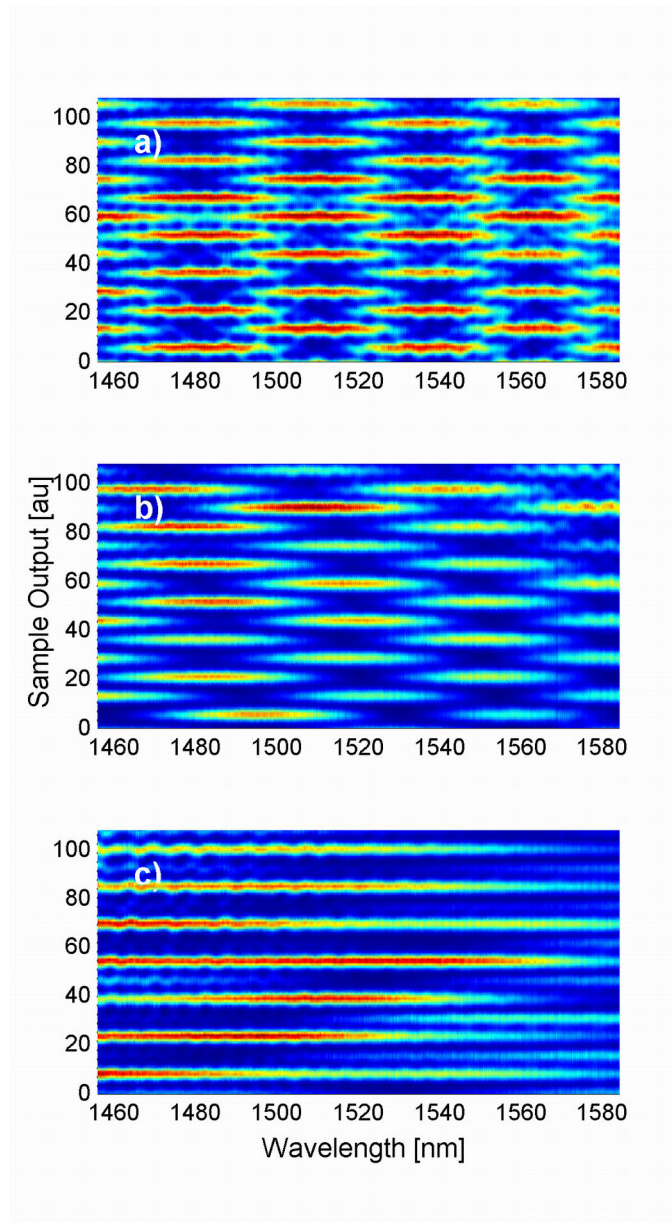


Figure 5.5 Experimentally observed Talbot revivals for the input field pattern $[1, 0, 1, 0, \dots]$ and different Bloch momentum ϕ : a) 0 , b) $\pi/4$, c) $\pi/2$. a).

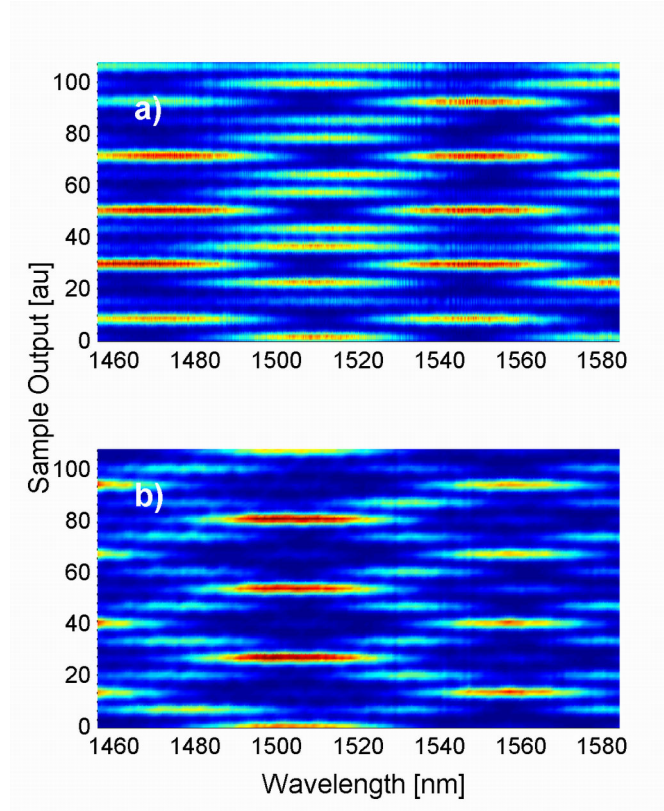


Figure 5.6 Experimentally observed Talbot revivals for in-phase input field patterns: a) $[1, 0, 0, 1, 0, 0, \dots]$ and b) $[1, 0, 0, 0, 1, 0, 0, 0, \dots]$ excitations.

In conclusion, discrete Talbot revivals in one-dimensional waveguide arrays were experimentally observed. Unlike continuous systems where the Talbot self-imaging effect always occurs irrespective of the pattern period, in discrete configurations this process is only possible for a specific set of periodicities. Moreover, the Talbot distance is dependent on the Bloch momentum of the excited beam. The results may be relevant to other areas of physics where such Talbot recurrences may be observed. These include, for example, optical wave propagation in photonic crystal structures and Bose-Einstein condensates in optically induced periodic potentials [109].

CHAPTER SIX: QUADRATIC SOLITONS

The experiments on the excitation of discrete quadratic solitons in PPLN waveguide arrays for two different confinement cases are presented in this chapter. Weakly-localized solitons were excited by the FH only beam. Relatively wide, stable solitons were formed on propagation due to the balance between diffraction and cascading [33]. On the other hand, the excitation of strongly-localized solitons required both the FH and SH fields to be launched in-phase. The formation of the solitons for different relative phase differences between the FH and SH was studied and a close relation between the highly-localized solitons and the nonlinear eigenmodes of the single channel was discussed [34].

6.1. Introduction

Different kinds of quadratic discrete solitons have been theoretically predicted to exist in waveguide arrays [22, 23, 115]. Their continuous media counterparts, i.e. multi-colored or quadratic spatial solitons, had already been experimentally demonstrated previously [116, 117]. It was shown that the wavevector mismatch $\Delta\beta = 2\beta(\omega) - \beta(2\omega)$ between the participating waves is a crucial parameter which determines the features of the respective soliton families [118]. The size and the sign of this mismatch govern the character and strength of nonlinear phase modulation [42, 119]. It is now well-known that this cascading nonlinear phase shift can also lead to a self focusing of both the FH and the SH [120]. In fact, the inhibition of transfer of

between the two channels of a dual directional coupler has been observed at high intensities due to this $\chi^{(2)}$ effect [58]. Thus it is not surprising that discrete quadratic solitons were subsequently predicted theoretically to exist in weakly coupled arrays of channel waveguides tuned close to their phase-matching condition for second harmonic generation.

For the experimental investigation of quadratic discrete solitons, the fiber-based laser system producing a 5 MHz train of bandwidth limited 7.65 ps long pulses at 1557.3 nm was used (see detailed parameters in Table 4.4). All experiments were performed with the weakly coupled sample Pb381z (see detailed parameters in Table 3.5). The phase-matching temperature was 234°C. The required wavevector mismatch $\Delta\beta L$ was adjusted by varying the sample temperature T according to the formula

$$\Delta\beta L = 8.1 \times (234 - T [^{\circ}C]) \quad (6.1)$$

which is based on the known temperature dispersion in the refractive indices and detailed modeling of the waveguide channels.

6.2. Weakly localized solitons

The experimental setup used in the excitation of weakly localized solitons is shown in Figure 6.1. The laser output beam was shaped spatially, with a cylindrical lens C, into an elliptical shape 62 μm wide (FWHM) and 3.5 μm high, and focused by a 10X FL-10B microscope objective onto the polished front facet of the waveguide array. In this way the FH was launched into TM_{00} modes of the array waveguides with an overlap efficiency of 50÷60%. No SH was inputted and the SH soliton component was generated near the input facet during propagation. A half-waveplate in a motorized mount was placed in front of the polarizer to

control the input power. Another motorized stage controlled the tilt of an antireflection coated 3 mm thick window W. It resulted in a tilt-dependent transverse beam translation of the beam incident onto the in-coupling MO and consequently in a tilt relative to the channel direction of the input beam at the input facet of the sample, i.e. a controlled relative phase between adjacent channels was generated. To reduce the average power in the waveguides a mechanical chopper with duty cycle 1:10 was used. The sample was heated in an oven both to minimize photorefractive effects and to adjust the wavevector mismatch. The output of the array was observed with the separate cameras for the FH and the SH, and quantified by measuring the temporally averaged output intensities using calibrated diodes and lock-in techniques.

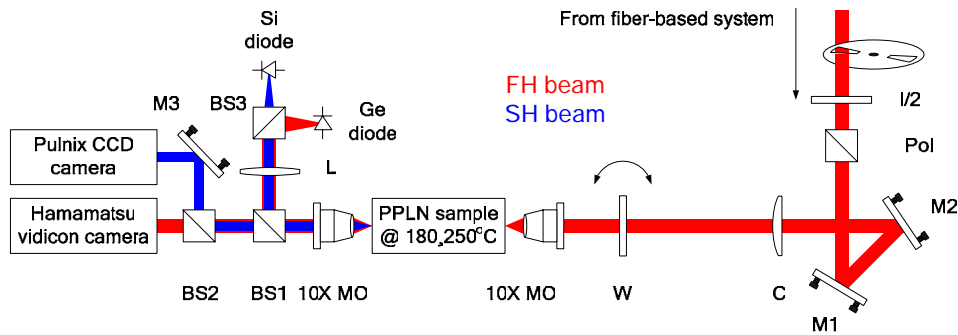


Figure 6.1 Experimental setup for the excitation of weakly localized solitons.

First measurements were taken for a positive wavevector mismatch $\Delta\beta L$ and normal diffraction – the combination of parameters for which an unstaggered soliton was expected to exist. Hence we focused the FH input beam untilted onto the sample, i.e., with a phase front parallel to the input facet, and the beam maximum centered on the guide. A narrowing of the FH and the SH at the output was observed with increasing input power until the width of the FH output equaled the width of the input beam. A typical output FH energy distribution as a function of the input FH peak power is shown in Figure 6.2. At input power levels ($>800\text{W}$) exceeding

twice the soliton threshold power (400W) the beam broadens. This is not predicted by the simple theoretical model used for simulating the experiment. Residual photorefraction, nonlinearly induced absorption and longitudinal inhomogeneities in the channels are believed to be the principal reasons for this discrepancy. These effects are all expected to come into play for high input powers and are not included in theoretical modeling. Figure 6.3 shows typical measured and simulated output intensities for both wavelength components for an odd, unstaggered soliton. The low power diffraction patterns are also shown for comparison.

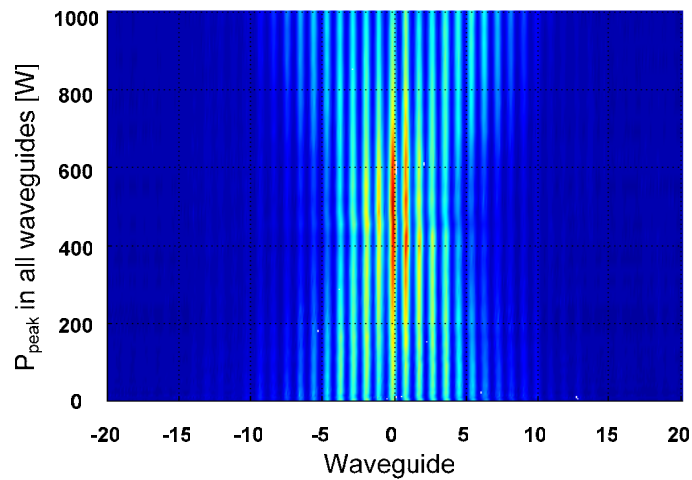


Figure 6.2 The FH energy distribution output from the array as a function of the input peak power for an array with the coupling length $L_c = 9.53$ mm for a positive wavevector mismatch.

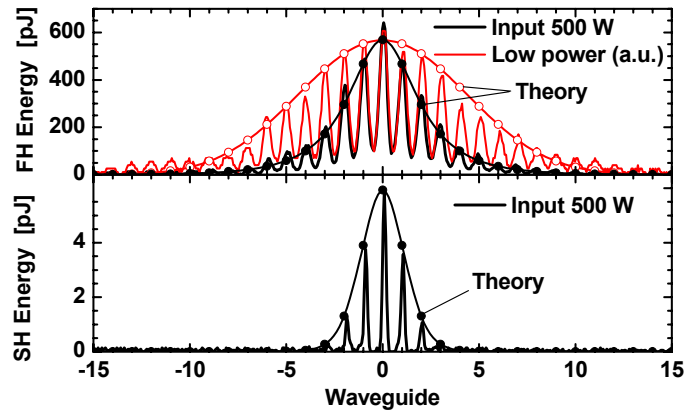


Figure 6.3 Spatial pulsed energy profile of the two nonlinearly coupled frequency components of an unstaggered odd discrete soliton ($\Delta\beta L = 140\pi$, $L_c = 15.74$ mm, FH input peak power of 500 W). Dotted lines and open circles show the low power FH diffracted beam, solid lines and circles show the soliton. Circles identify theoretical data.

In order to obtain a more complete insight into the physics of soliton formation the experiments were repeated for a several positive values of $\Delta\beta L$ (and thus positive nonlinear phase shift) and in different arrays with varying coupling lengths. As expected from theoretical predictions, Figure 6.4 (on the positive side of phase-matching) confirms the powers needed for soliton formation increased with the coupling strength and $\Delta\beta L$. The latter result is a clear indication of the quadratic nature of the nonlinear process, i.e. nonlinear phase modulation decreases with increasing $\Delta\beta L$.

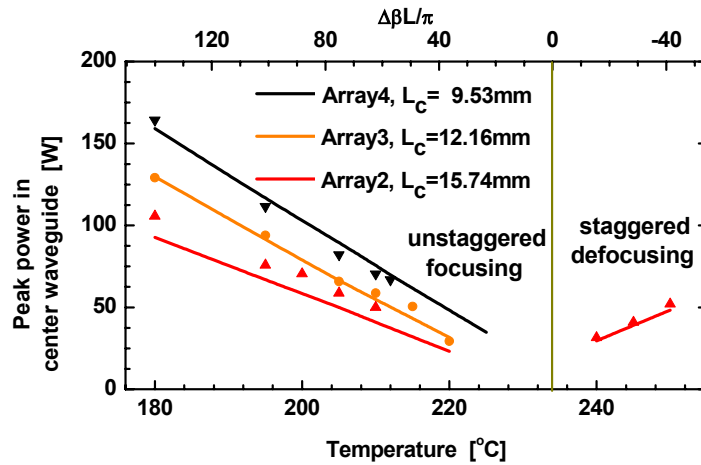


Figure 6.4 Soliton peak power versus $\Delta\beta L$ for arrays with different coupling lengths L_c .

In Figure 6.5a the calculated evolution with distance of the FH and the SH energy distribution for a single pulse clearly indicates soliton behavior since the energy profile does not change significantly during the propagation. Moreover, the generation of the SH part of the soliton shortly after the input can be observed. The waveguide losses, although very small, are responsible for the power loss during the propagation over 7 cm. Furthermore, the simulations help to interpret the measured temporally averaged SH profiles, which in principle developed a complex temporal structure due to walk-off effects caused by the unequal FH and SH group velocities. In general, most of the SH temporally overlaps the FH and represents the soliton's SH component. A second SH (radiation) pulse, decoupled from the soliton, trails the soliton by the 24 ps walk-off time in a 7 cm long sample.

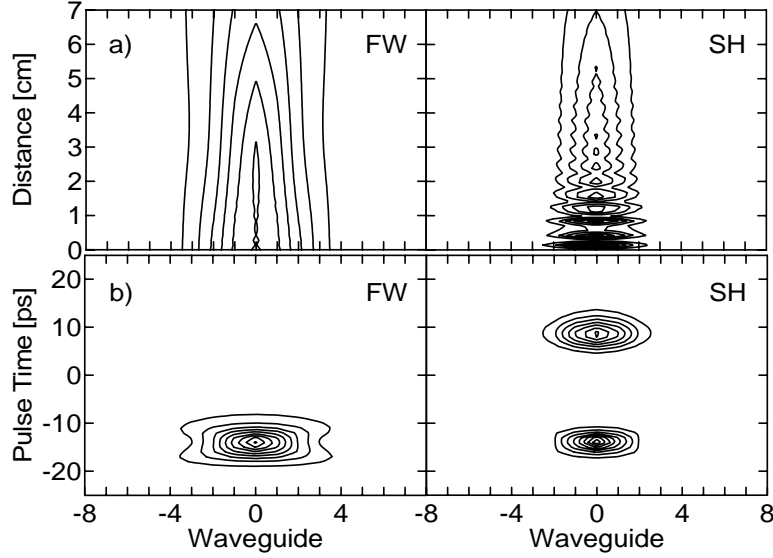


Figure 6.5 (a) Simulated evolution of the transverse energy (time integrated) spatial profile of beams excited by a FH input ($\Delta\beta L = 140\pi$, $L_c = 15.74$ mm, FH input peak power of 442 W). (b) Spatio-temporal output distribution of the simulation in (a).

The calculated spatiotemporal distribution at the output, shown in Figure 6.5b, indicates soliton propagation for the mutually locked FH and SH. The spatial narrowing of the FH in the pulse center is evident. Although the soliton's SH component increases closer to phase-matching, the SH radiation that has temporally walked away from the soliton increases even faster. Therefore an increasing part of the measured, temporally averaged, SH output no longer belongs to the soliton and a reliable SH soliton profile measurement is not possible for $|\Delta\beta L < 20\pi|$ with 7.65 ps long pulses in the sample.

Next an experiment for a negative wavevector mismatch and in-phase (unstaggered) as well as anti-phase (staggered) excitation was performed. As theory predicts for unstaggered excitation, delocalization additional to that caused by discrete diffraction was observed due the

negative cascading nonlinearity (see Figure 6.6), i.e. the output beam broadens with increasing power because negative phase modulation reinforces normal diffraction.

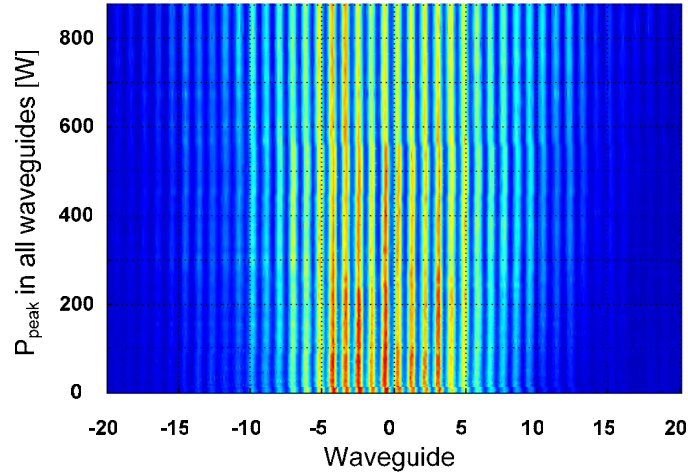


Figure 6.6 FH output energy distribution as a function of input peak power for an array with the coupling length $L_c = 9.53$ mm, negative wavevector mismatch and unstaggered excitation.

Bright soliton formation can be expected only for a staggered excitation under these conditions of wavevector mismatch at the edges of the Brillouin zone where diffraction is anomalous. Excitation with the required phase difference of π between modes in adjacent waveguides was realized by appropriately tilting the input beam by ~ 3 degrees. Figure 6.7 shows a typical measured output energy distribution of the FH as a function of the input peak power for negative wavevector mismatch and staggered excitation. Similarly to the case of the unstaggered soliton for a positive wavevector mismatch, the beam initially narrows down to the input beam width with increasing input power. At the input powers exceeding about twice the soliton threshold power, the output broadens again.

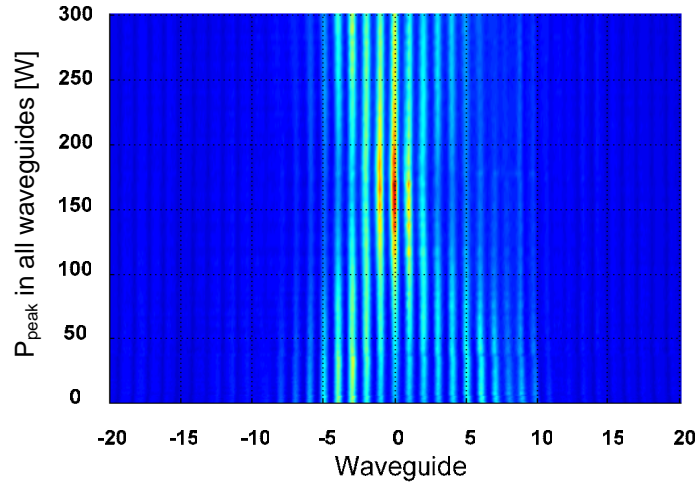


Figure 6.7 FH output energy distribution as a function of input peak power for an array with the coupling length $L_c = 15.74$ mm, for a negative wavevector mismatch and for staggered excitation.

The profiles of the nonlinearly broadened beam and staggered soliton for the cases just described are shown in Figure 6.8. The low power diffraction pattern is also shown for comparison. The non-ideal low power linear diffraction pattern observed for staggered excitation is caused by the approximate method of anti-phase excitation used in the experiment and the corresponding aberrations introduced. Specifically, tilting of the input beam results in a non-planar but rather curved wavefront at the input facet as well as strong excitation of the higher order bands of the periodic array. Note, however, that soliton formation results in a very clean output signal. Again the quadratic nature of the nonlinear process was confirmed (see Figure 6.4 for negative values of phase-matching), as soliton power decreases with decreasing wavevector mismatch.

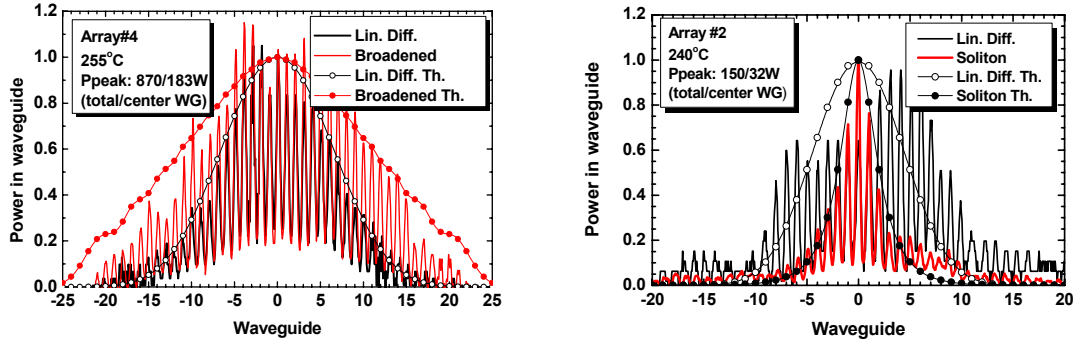


Figure 6.8 Nonlinearly reinforced beam broadening for in-phase excitation for $\Delta\beta L = -50\pi$, $L_c = 12.16$ mm, FH input peak power of 870 kW) (on the left); Staggered soliton profile ($\Delta\beta L = -16\pi$, $L_c = 15.74$ mm, input peak power of 150 W) (on the right). Solid and empty circles identify the high and low power theoretical data, respectively.

Finally, the stability of the excited discrete solitons was also investigated experimentally. Odd solitons are centered on a channel and even solitons are centered between channels. As predicted by theory and explained in chapter 2.5.2, odd solitons are stable, whereas the even ones are unstable. In agreement with this prediction, it was found that very careful transverse beam alignment, with the input beam maximum centered as precisely as possible on a channel, was necessary to obtain stationary in time output pictures of the soliton profiles. For example, different time frames in Figure 6.9a show stable powers in the three central waveguides of an odd unstaggered soliton ($\Delta\beta L > 0$). When the input maximum was centered between the waveguides, a strongly flickering output as documented in the time frames of Figure 6.9b was observed. The output profile's maximum jumped between the two waveguides adjacent to the input beam's maximum; i.e. the excitation tried to evolve into a beam profile centered on either one of the two neighboring channels. The observed instability was presumably seeded by small

fluctuations in the pointing direction of the input beam due to vibrations in the optical mounts, etc.

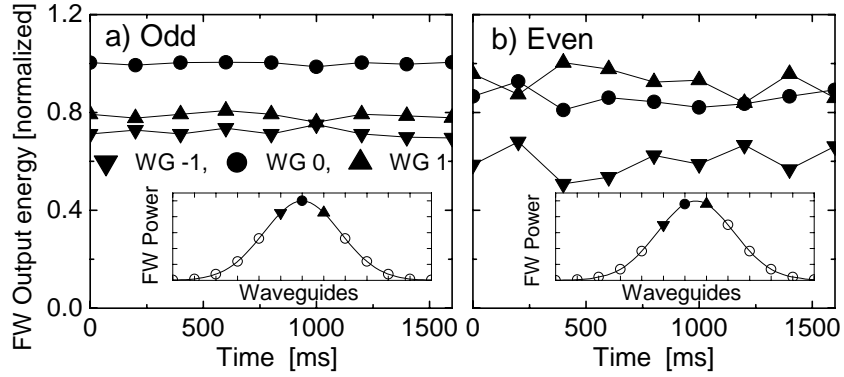


Figure 6.9 Time sequence of FH output energies, sampled at intervals of 200 ms, from waveguides in the soliton center as indicated in the insets ($L_c = 15.7$ mm, $\Delta\beta L = 140\pi$). (a) Stable output for odd soliton excitation. b) Unstable output for even excitation.

In summary, the first experimental proof of the existence of both staggered and unstaggered stable discrete quadratic solitons was presented in this chapter. Both solitons were excited in the same sample by merely changing the excitation conditions, namely as the input beam tilt and the wavevector mismatch. Increased beam broadening was also measured when the wavevector mismatch and thus the sign of phase modulation were chosen to reinforce instead of to cancel discrete diffraction.

6.3. Strongly localized solitons

Calculations have shown that the excitation of quadratic strongly localized solitons (solitons for which most of the power is guided in one channel) requires both the FH and the SH to be present in-phase at the input. This is in contrast to their counterparts in continuous media [116], slab waveguide [117] or even weakly localized discrete solitons in waveguide arrays [33], where a only FH field can be launched and it will evolve into a stable quadratic soliton on propagation. In that case, the interplay between SHG, diffraction and self-focusing leads to soliton formation and the excess electromagnetic energy is radiated away into the diffracting dimensions. However this is not the case for highly localized discrete quadratic solitons since the excess SH radiation is not able to escape into the bounding media. For high FH input powers launched into the sample, no stationary mode is obtained and periodic power exchange between FH and SH occurs with a period equal to the coherence length for SHG (see simulation in Figure 6.10). Similar results were obtained over a large range of input conditions. These results resemble the energy oscillations during SHG, for non-zero wavevector mismatch in an isolated waveguide when the ratio of FH to SH at the input differs from that for the steady state case [119]. A balanced case (steady state), where there is no net energy exchange between the FH and the SH on propagation, corresponds to the nonlinear eigenmode of the waveguide. Two species of these nonlinear eigenmodes exist with FH and SH fields either in-phase or out-of-phase, and with a specific amplitude ratio which depends on the wavevector mismatch and the total power [121, 122].

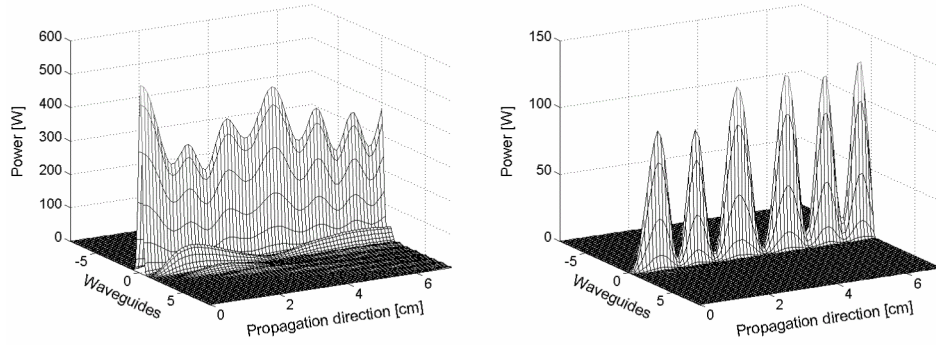


Figure 6.10 Numerical simulations for CW propagation of the FH (on the left) and SH (on the right) with input conditions of $P_{FH} = 560$ W, $P_{SH} = 0$ W, and $\Delta\beta L = 106\pi$. Only the FH is input.

The fact that there is a close relation between the in-phase eigenmodes and quadratic solitons in continuous media is well known. Numerical modeling of propagation in waveguide arrays was performed for initial values of the FH and the SH fields equal to the isolated channel eigenmode solutions. It confirmed that a stable propagating soliton was indeed formed after initial small oscillations. Furthermore, the final powers of the soliton's FH and SH components are essentially the powers associated with an eigenmode of the isolated channel. Figure 6.11 shows numerical simulation of FH and SH beam propagation in the array when the in-phase eigenmode of an isolated channel was launched with the same total power as in Figure 6.10.

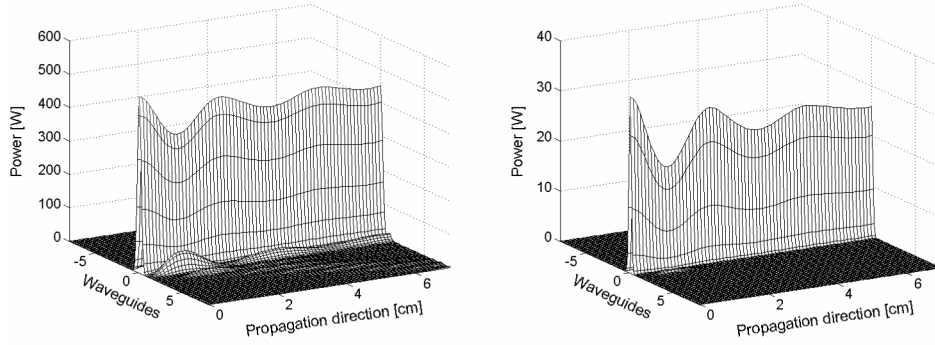


Figure 6.11 Numerical simulations of the CW propagation in an array of the FH (on the left) and SH (on the right) with input conditions associated with an in-phase eigenmode of an isolated channel. Here $P_{FH} = 525$ W, $P_{SH} = 35$ W, and $\Delta\beta L = 106\pi$.

Next, the dependence of the output from the array on the input relative phase between the FH and SH fields in the seeded case was investigated numerically. For comparison with the experimental results, all experimental details were taken into account, including also losses, pulsed excitation and the measured longitudinal non-uniformities in the wavevector mismatch. Shown in Figure 6.12 is the dependence of the array's output FH and SH on the relative input phase between them for pulsed single channel excitation. The input peak power levels were chosen for the best soliton formation which differed from the powers used in the idealized CW simulations. Note that for the in-phase case, the FH beam at the output is primarily localized to the central (excitation) channel and the SH, although also localized, is weak. For the out-of-phase case, the FH output resembles a discrete diffracted beam spreading through the array, and it is the SH that is strongly localized in the central channel. In fact as shown in Figure 6.12, inputs over the full range of relative phases evolve always into essentially two well-defined output states. The one centered at zero relative phase difference corresponds to a stable, highly localized discrete quadratic soliton closely related to the in-phase single channel eigenmode,

whereas the second is centered on a relative phase difference of π and corresponds to the out-of-phase eigenmode because of the lack of coupling in SH. In the second case part of the initial FH power is up-converted to the SH and the excess is diffracted.

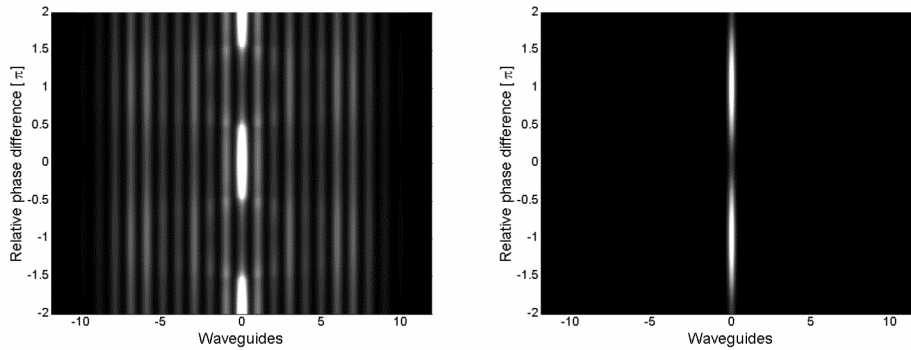


Figure 6.12 Numerical simulations of the array output versus relative phase difference between FH (on the left) and SH seed (on the right) pulses, assumed to be 7.65 ps. Input powers for FH and SH are 400 W and 7 W, mismatch $\Delta\beta L = 90\pi$.

Experiments were performed, because of power restrictions, only with the weakest coupled array on the Pb381z sample, with a coupling length of 25.6 mm for the FH. The experimental setup, shown in Figure 6.13, is a modification of setup used for the excitation of weakly localized solitons. The FH beam was split into two arms. One beam was frequency doubled in a PPKTP crystal. Both, the FH and the SH beams were shaped to match the waveguide mode profiles, combined with help of a dichroic beam combiner BC and launched into a single channel of the array. A high suppression ratio filter was used in the SH arm to remove any existing FH content and prevent it from coupling to the sample. A pulse delay line was used to ensure optimum pulse overlap. An active control of the relative phase difference between the FH and the SH with was realized with a mirror attached to a piezo element in the SH

arm. In order to measure the phase difference changes dynamically a He-Ne laser beam was beam-split with one part transmitted in the FH arm of the input and the second part in the SH arm of the apparatus. Changes in the interference fringes from the two He-Ne beams were monitored by a vidicon camera, translated into phase changes at 775 nm and applied to evaluate changes in the relative phase between the FH and SH. The output of the sample was observed with cameras for the FH and the SH separately and with power detectors.

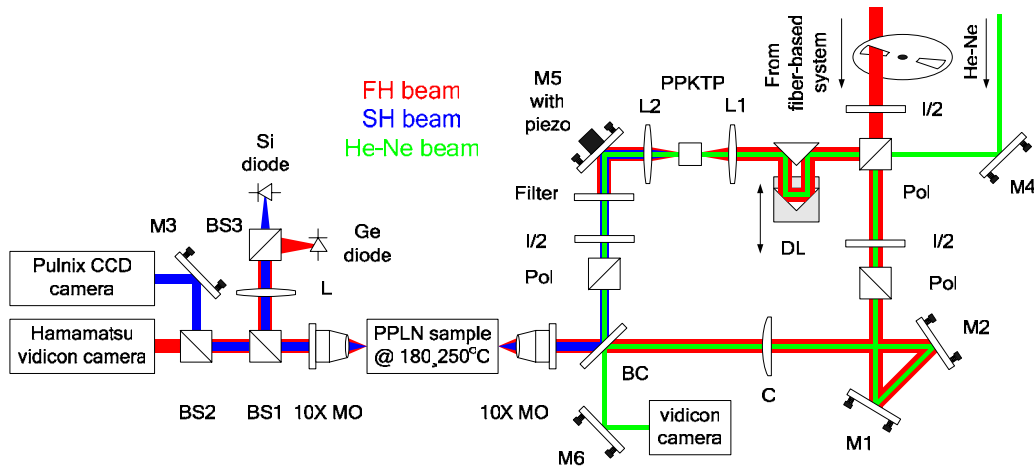


Figure 6.13 Experimental setup for the excitation of strongly localized discrete quadratic solitons.

The experimental results for the FH and SH output from the array are shown in Figure 6.14. The data for both the array output and the relative input phase were taken at 30 frames per second and then processed to produce the plots of the FH and SH intensities. Note that there is either a strong or a weak output in the central channel for both cases and essentially no intermediate states, as predicted theoretically in Figure 6.12. For the case with in-phase FH and SH, a strong central channel FH confinement occurs together with a weak SH component

forming the stable propagating highly localized quadratic array soliton. Due to the pulsed excitation the soliton is accompanied by weak remnants of linear diffraction peaks far from the input waveguide due to the weak wings of the pulses. In the out-of-phase case a strong SH is very tightly localized to the central channel accompanied by only a weak FH. All of these results are in good quantitative and qualitative agreement with the theoretical discussion above. The remaining small differences between theory and experiment, for example smaller contrast and poorer localization of the experimental FH, are due to effects like residual photorefraction and nonlinear absorption not included in the model.

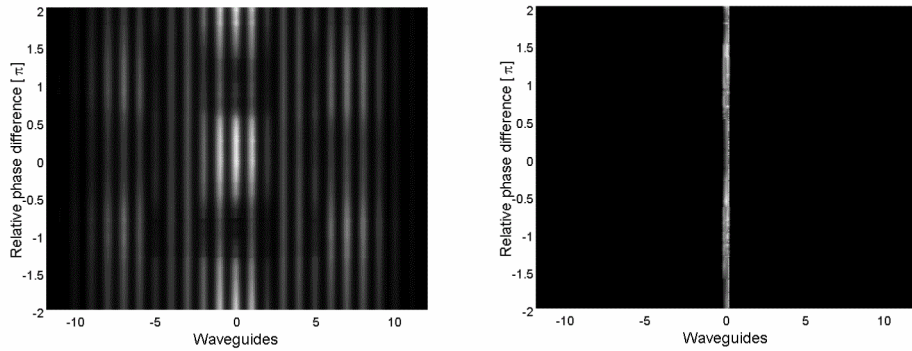


Figure 6.14 Experimental FH (on the left side) and SH (on the right side) output power distribution vs. input relative phase difference, for the following input conditions: $P_{FH} = 400$ W, $P_{SH} = 7$ W, $\Delta\beta L = 90\pi$.

In summary, it was found that single channel discrete solitons in weakly coupled quadratically nonlinear waveguide arrays are much richer phenomenon than in their counterpart Kerr waveguide arrays. This is a direct consequence of the dual frequency nature of the solitons, coupled to the fact that only the FH fields can undergo discrete diffraction. This has led to the existence of two output states for a single excited channel, one in which the FH dominates and

the second in which the SH dominates. Modeling based on the discrete coupled wave equations predicts this behavior and indicates that the relative phase between the FH and SH at the input determines the output state.

CHAPTER SEVEN: MODULATION INSTABILITY

One of the most fundamental consequences of propagating high intensity, plane wave beams in media with an effective self-focusing nonlinearity is that filamentation due to modulational instabilities (MI) occurs because of any amplitude or phase noise present on the beam [123, 124]. For finite, but still very broad input beams, these filaments can evolve with distance into spatial solitons for appropriate conditions on the dimensionality of the medium, and the detailed form of the nonlinearity. Such phenomena have been observed in a variety of continuous nonlinear systems including hydrodynamics [125, 126], plasma physics [127], and Bose-Einstein condensates [128]. In nonlinear optics, MI has been observed in both the temporal [129] and spatial domains [130-132]. The spatial behavior shares many universal properties independent of the origin of the nonlinearity because diffraction has only one sign in continuous media.

However in a discrete system, because of its unique diffraction properties, modulational instability exists only for correct combination of signs of diffraction and nonlinearity [21]. In quadratically nonlinear media, this diversity is even larger because the nonlinearity can be either self-focusing or self-defocusing, depending on the sign of the wavevector mismatch. In this chapter, experimental results of an investigation of discrete modulational instability in quadratically nonlinear waveguide arrays are presented [35].

7.1. Introduction

The nonlinear behavior of beams in discrete media consisting of arrays of weakly coupled channel waveguides has been of intense interest recently in cubic, quadratic and photorefractive media [27, 30, 33]. One of the reasons for the proliferation of spatial discrete solitons when compared to that found in continuous media is the sinusoidal shape of the wavevector dispersion relation (see Figure 2.7). Thus the diffraction coefficient D can be either normal (negative as in continuous media) or anomalous (positive with no analog in continuous media). For a self-focusing nonlinearity, filamentation due to MI is expected to occur for regions of normal diffraction and to be absent for regions of anomalous diffraction [21, 133]. This diversity of behavior forbidden in continuous media has been reported recently in 1D arrays of AlGaAs channel waveguides which exhibit self-focusing Kerr nonlinearities [134].

Quadratically nonlinear media play a unique role in soliton science because their solitons consist of two or three frequency components, which are strongly coupled in a parametric interaction based on the quadratic nonlinearity $\chi^{(2)}$. Moreover, in quadratic arrays, not only can the sign of diffraction for the fundamental beam be changed by varying the propagation direction across the array, but also the sign of the effective nonlinearity by varying the wavevector mismatch condition for the parametric interaction [120]. Therefore in terms of MI, filamentation can occur for the combinations of positive wavevector mismatch and normal diffraction ($D < 0$), and also for negative wavevector mismatch and anomalous diffraction ($D > 0$). For the remaining two combinations of diffraction and sign of wavevector mismatch, no filamentation is expected.

7.2. Setup and experimental results

A layout of experimental setup is shown in Figure 7.1. The broad input fundamental beam was obtained from an Ekspla OPG/OPA system (see Table 4.5 for details) producing 15 ps pulses with energies up to 200 μJ with energy stability of $\pm 15\%$. A telescope, consisting of two cylindrical lenses C1 and C2, was used to produce a highly elliptical beam (350 x 3.5 μm FWHM) approximately Gaussian in shape in two dimensions with a planar wavefront at the sample's input facet. The beam covered approximately 23 channels. Array # 2 of Pb381z sample (see Table 3.5 for details) with a coupling length of 15.74 mm was used in the experiment. The sample was housed in an oven and heated to temperatures of 200°C in order to minimize photorefractive damage. The phase-matching condition was tuned by varying the OPG/OPA wavelength from 1547 to 1565 nm. An anti-reflection coated, 3 mm thick window W, placed on a motorized rotational stage was used to control the angle of incidence of the beam. It produced a tilt-dependent horizontal translation of the beam incident onto the in-coupling microscope objective and consequently in a beam tilt relative to the channel direction at the input facet of the sample, i.e. a controlled relative phase between adjacent channels ($k_y d$) was generated. The output facet of the sample was imaged, using a 10X MO onto the Roper Scientific OMA V InGaAs line camera. For alignment purposes a Hamamatsu vidicon camera was used. An additional Si CCD camera was used for imaging of SH.

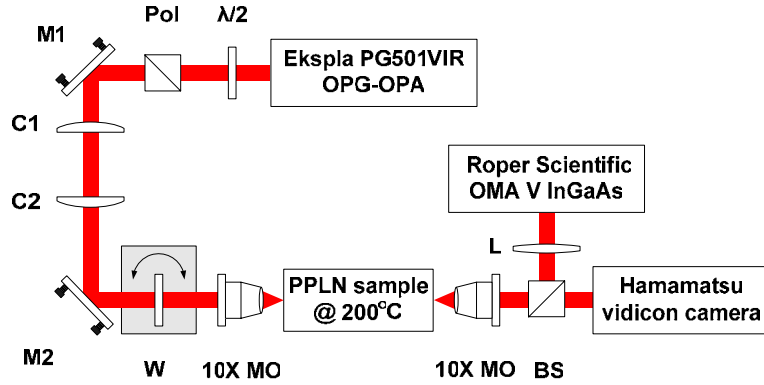


Figure 7.1 Experimental setup.

The first nonlinear experiments consisted of directing the input fundamental beam at normal incidence ($k_y d = 0$) for which the array exhibits normal diffraction onto the array for both positive and negative wavevector mismatch. The beam observed emerging from the output facet was measured as a function of increasing fundamental input energy of the pulse and is shown in Figure 7.2. As the input intensity is increased for positive wavevector mismatch, self-focused filaments form and narrow with increasing power. Here waveguide imperfections play the role of an amplitude “seed”. Collapse becomes more pronounced with increasing input energy indicating MI. On the other hand, for negative wavevector mismatch the cascading nonlinearity is defocusing and indeed no filaments are formed. Note that moving from one limit to the other just involved a change in the input wavelength. The small linear modulation observed at low powers is due to interference with modes associated with higher order bands.

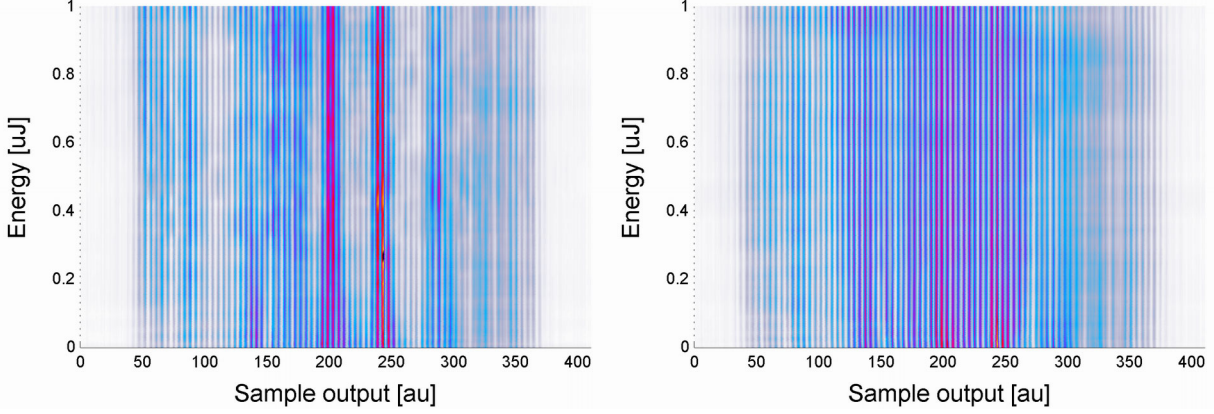


Figure 7.2 Distribution across the array of the fundamental beam output power from the array for normal incidence as a function of the input pulse energy: positive wavevector mismatch $\Delta\beta L = 170\pi$ (on the left) and negative wavevector mismatch $\Delta\beta L = -40\pi$ (on the right). Note the different behavior of the two defect-created “hot spots” at the positions 200 and 250.

The effect of varying the relative input phase $k_y d$ through the zero diffraction point was also investigated. These measurements were limited primarily by the large sample lengths and the total number of channels in an array because reflections occur at the array boundaries for $k_y d \geq 0.75\pi$. Nevertheless, it is clear from the high input power pictures in Figure 7.3 that for positive wavevector mismatch filamentation only occurs for $k_y d < 0.5\pi$ (i.e. normal diffraction) and disappears for $k_y d > 0.5\pi$ (anomalous diffraction). In contrast to this, for negative wavevector mismatch, no filamentation occurs for $k_y d < 0.5\pi$ but does occur for $k_y d > 0.5\pi$. All of these results are consistent with filamentation when the product of the diffraction coefficient D and the wavevector mismatch $\Delta\beta L$ is negative, and no filamentation when the product is positive. These results are in agreement with the previous experiments on MI

observed due to the Kerr nonlinearity in AlGaAs arrays [134]. In the present case, MI for self-defocusing nonlinearities by working at negative wavevector mismatch was also demonstrated.

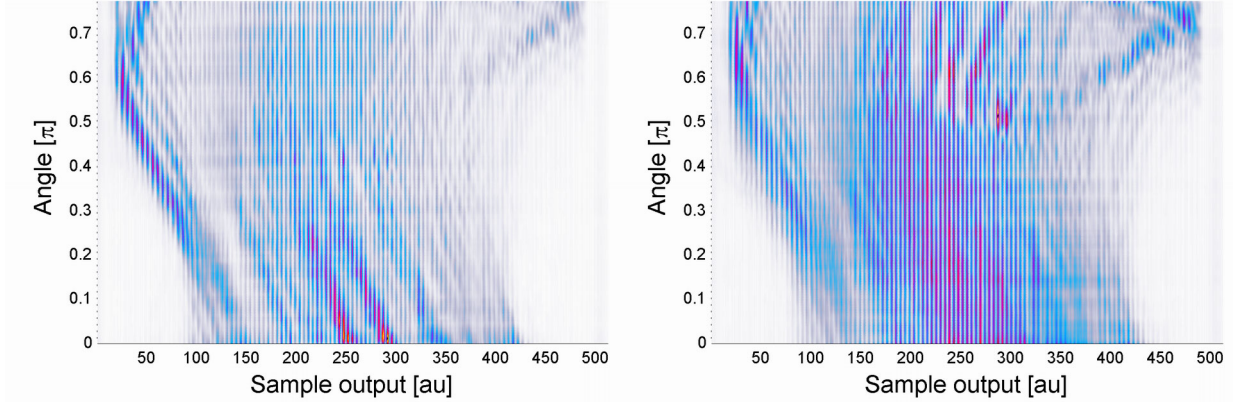


Figure 7.3 Distribution across the array of the fundamental beam output power from the array as a function of the relative input phase between adjacent channels: positive wavevector mismatch $\Delta\beta L = 170\pi$ (on the left) and negative wavevector mismatch $\Delta\beta L = -40\pi$ (on the right). The input pulse energy was $0.27 \mu\text{J}$.

In summary, MI gain due to discrete modulation instability in arrays with quadratic nonlinearities was observed. Whether filamentation occurs or not depends on the sign of the product of the diffraction coefficient D and the cascading nonlinearity $n_{2\text{eff}}$ as given in the Table 7.1 below.

Table 7.1 Conditions for existence of the modulational instability in the quadratic discrete system.

Filamentation	$D < 0$	$D > 0$
$n_{2\text{eff}} < 0$	No	Yes
$n_{2\text{eff}} > 0$	Yes	No

CHAPTER EIGHT: PARAMETRIC SWITCHING

There are a variety of guided-wave devices based on ultrafast second and third order optical nonlinearities by which information can be split into different output paths on-demand via optical control beams. Nonlinear directional couplers, X switches, and nonlinear loop mirrors inherently have two spatially separated output ports [135-138]. Other options that involve nonlinearly induced changes in the polarization, wavelength, or arrival time of signals require additional elements such as polarizers and etalons for separating out the desired signal [135]. Despite their impressive processing speed all these procedures suffered from small values of fast off-resonance optical nonlinearities that result in either high required peak powers or long device dwell times. Active semiconductor optical amplifiers based on complex pumping schemes have offered a drastic reduction of the control powers to some milliwatts with tens of picoseconds response times [136, 137]. In parallel, different all-optical devices have been developed to shift signal wavelengths, an important function in wavelength-division multiplexing communications systems [136, 139-142]. Second-order nonlinear devices that rely on sum- and (or) difference-frequency generation have been developed for this purpose [140-142]. To date, both of these functions, spatial routing and wavelength shifting have been implemented in separate devices. Many previously suggested spatial second-order switching designs were based primarily on quadratic solitons effects that require high signal power levels [143].

In this chapter an efficient switching and routing of low power signals in second-order nonlinear waveguide arrays is demonstrated [36, 37]. The signal can be switched to different

spatial output positions by a control beam and can be simultaneously converted to another wavelength with a low cross-talk. This approach utilizes a combination of the nonlinear processes of parametric amplification and difference-frequency generation and the linear characteristics of wave propagation in arrays of weakly coupled channel waveguides.

8.1. Introduction

The main idea of the novel switching scheme investigated in this chapter is to collide two low power beams consisting of a signal with wavelength $\lambda_s = \lambda_0 + \Delta$, where Δ represents a relatively small wavelength shift, and a control (pump) beam whose wavelength is half of the signal $\lambda_p = \lambda_0 / 2$. As described in Chapter 2.5.1, diffraction (beam spreading) of optical beams in waveguide arrays occurs by light coupling from channel to channel. The strength of discrete diffraction depends on the phase difference between the excited modes in adjacent waveguides of the array which can be simply adjusted by a slight tilt of the input beam with respect to waveguide direction. Additionally, there is a strong chromatic dispersion of the inter-channel coupling, due to different confinement of the FH and SH mode profile. For example, beams with a shorter wavelength (SH) are strongly confined in the waveguide and consequently couple to neighboring channels very weakly, i.e. with typical coupling distances many times the sample length. Thus depending on the angle of incidence and the wavelength, beams with completely different diffraction properties can co-exist in the same waveguide array. This property is used in this scheme to confine the pump beam (shorter wavelength) in a single channel, whereas the signal beam (longer wavelength) can slide across the array. The few-channel-wide signal beam is launched at a diffractionless angle (Bloch momentum $k_y d = \frac{\pi}{2}$) and crosses the array (see Figure

8.1). It experiences only weak higher order diffraction. At the same time, one channel is excited by the control beam, which propagates straight down the array. At the crossing, the intersecting straight propagating pump and the tilted diffractionless signal beam interact in a $\chi^{(2)}$ parametric mixing process.

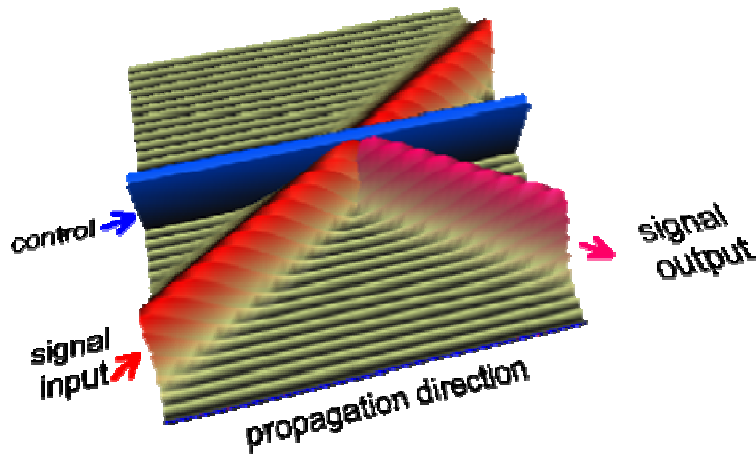


Figure 8.1 Geometry of the all-optical switching and frequency conversion scheme.

Because the interaction occurs in a single guide, the newly generated fields at the signal frequency spread symmetrically from this waveguide on both sides while the original channel-to-channel phase relation and therefore the directions of diffractionless propagation are maintained. Hence the process results in the amplification of the original signal beam and in the emission of an additional signal beam (see Figure 8.2c), which crosses the array without diffraction at the mirror angle. In addition, two more beams at the idler wavelength $\lambda_i = \lambda_0 - \Delta$ are generated (see Figure 8.2d) in the parametric mixing process, approximately following the path of the signal. For a small wavelength difference 2Δ between signal and idler (near degeneracy), the idler's propagation is also diffractionless. Because the output position and the powers of the new signal

and idler beams are controlled by the input position and power of the pump beam, this beam can be called the control beam.

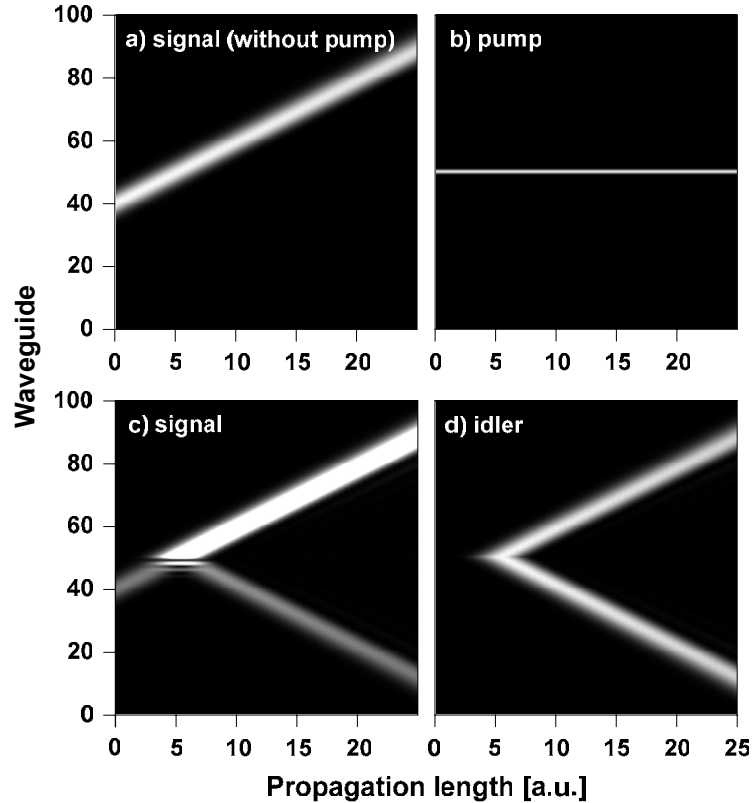


Figure 8.2 Simulated propagation of the signal and idler beams for the all-optical switching and frequency conversion scheme.

Owing to the non-degeneracy of the parametric process, the switching is phase insensitive. It is important to note that in this switching scheme the nonlinearity is used only to transfer light between individual light beams of different frequencies, and the spatial switching is accomplished by the wavelength-dependent discrete diffraction phenomena of linear waves in the array. Furthermore, because the device operates in the low depletion of the control beam regime, spectral broadening and pulse breakup of the signal are negligible. Because $\chi^{(2)}$ can be

considered an instantaneous nonlinearity, the bandwidth of the switching process is limited only by the chromatic dispersion of the wavevector mismatch, which is the source of temporal walk-off between signal and control. However because of the short interaction lengths involved, this is not a crucial limit. Time-resolved simulations predict a switching capability of the device up to a data rate of 100 GHz.

8.2. Setup and experimental results

The experiment was performed in array # 1 of the Pb344z sample (see Table 3.4 for detailed data) with a center-to-center channel spacing of 13.5 μm and a linear coupling length between adjacent waveguides of ~ 6 mm for the signal and idler. The sample was heated to a temperature of 215 $^{\circ}\text{C}$ which corresponds to a phase-matching wavelength of $\lambda_{PM} = 1548.7$ nm.

The experimental setup is shown in Figure 8.3. The control (pump) beam, whose wavelength $\lambda_p = 774.35$ nm was half the phase-matching wavelength, was generated by frequency doubling the color center laser, giving 5 ps long, transform limited pulses with a repetition rate of 76 MHz. A 10 mm long periodically poled KTP (PPKTP) crystal was used as the doubling crystal. In order to verify the phase-insensitivity of the switching concept, a different laser (tunable CW HP81680A laser diode) was used for the signal with a wavelength $\lambda_s = 1548.7 + \Delta$ nm. Although using a pulsed and a CW source avoided the problem of synchronizing two pulsed lasers, it also reduced dramatically the measured efficiency of the interaction due to the color center's small duty cycle (3.8×10^{-4}).

The output of the laser diode was shaped into an elliptical beam using a cylindrical telescope (cylindrical lenses C1 and C2), and was subsequently focused onto the entrance facet of the array to form a spot 3.5 μm high and 61 μm wide (FWHM) using a 10X microscope

objective FL-10B. The input beam tilt (and hence the relative phase between adjacent channels) was adjusted by moving horizontally a beam combiner BC which in turn displaced the beam from the center of the microscope objective and caused a tunable beam tilt. This tilt was adjusted to 1.6° , which corresponds to a phase difference of $\pi/2$ between the adjacent channels and hence zero diffraction in the array. With this simple setup the excitation efficiency of the ~ 4 waveguide wide signal beam was 36%. To control independently the relative position of the pump beam an afocal system, consisting of lenses L4, L5 and 10X MO and mirror M2, was built. The horizontal movement of the mirror which was placed on a translation stage together with lens L4 gave full control over the horizontal beam position, and at the same time did not affect the tilt and coupling efficiency. An additional mode matching lens L3 was used to bring both beams into focus at the input facet. It resulted in 20% coupling efficiency into the desired SH TM_{00} mode.

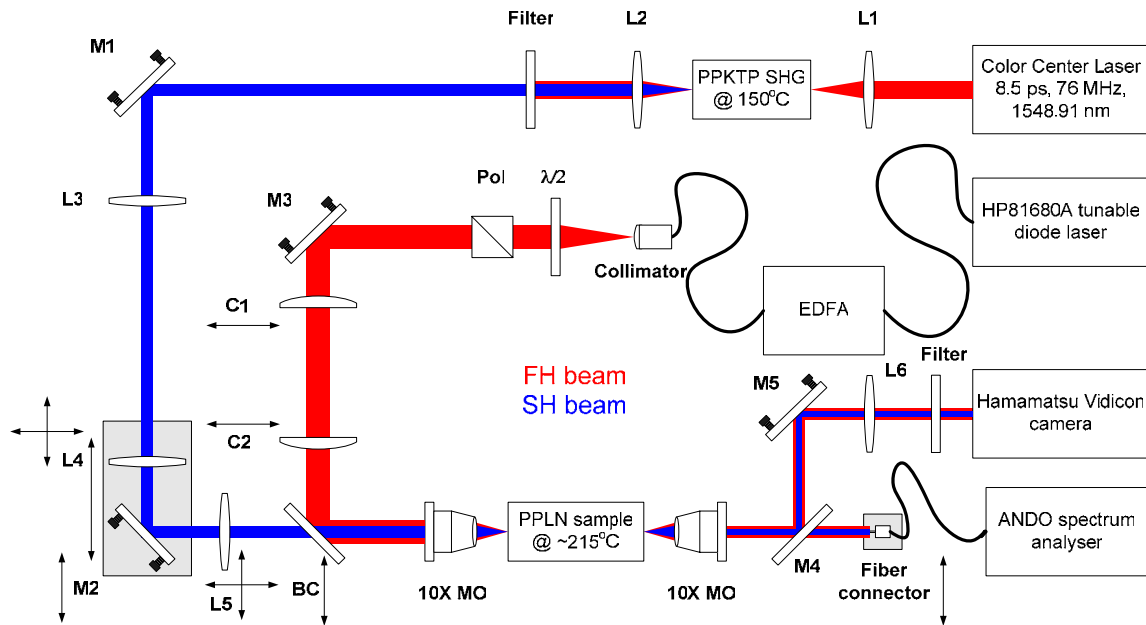


Figure 8.3 Experimental layout.

The output from the array was characterized by spatially resolved scanning of the spectrum. The output facet of the sample was imaged, with help of a 10X FL-10B microscope objective (MO), in a plane approximately 15 cm from the MO. A bare fiber on a motorized translation stage, was placed at the image plane to collect data and deliver it to a computerized spectrum analyzer ANDO AQ-6315E. A LabVIEW program was developed to synchronize the data acquisition. A typical result, plotted on a logarithmic scale, is shown in Figure 8.4.

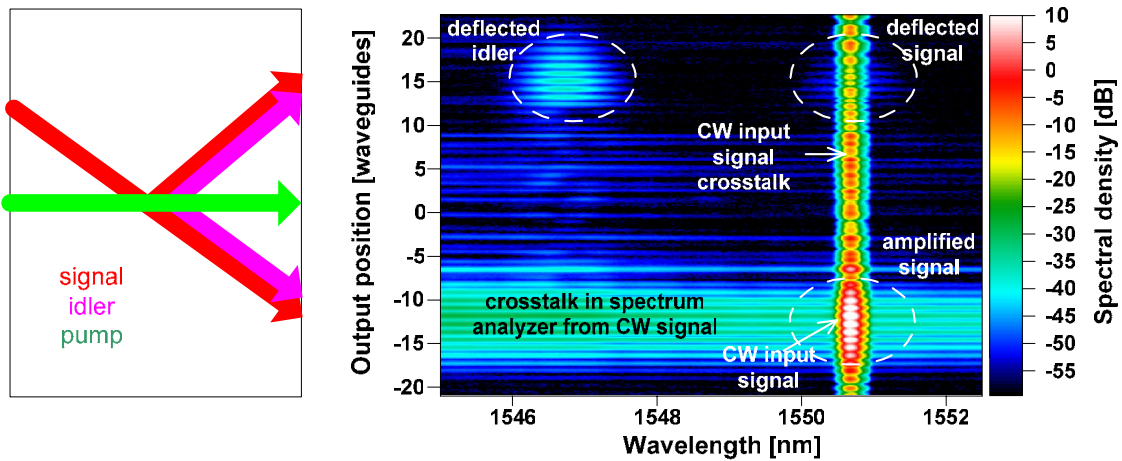


Figure 8.4 Geometry of the experiment (on the left) and spatial-spectral scan of the output of a waveguide array after parametric interaction of a signal beam ($\lambda_s = 1550.7$ nm, $P_s = 13$ mW, input centered at guide 12) and a control beam ($\lambda_p = 1550.7$ nm, $P_{peak} = 10.7$ W, input centered at guide 1) which generates an idler ($\lambda_i = 1546.7$ nm).

The signal beam was injected centered on guide 12 and exits the array centered on guide -13. With the injection of the control in guide 1, the parametrically deflected signal and idler exited the array centered on guide 15 at the output face. There are two strong cross-talks present in the scan, due to the small duty cycle associated with the signal-pump interaction. That is the

CW signal beams are acquired continuously by the detectors where-as the parametrically created beams only appear at the detectors 3.8×10^{-4} of the time. The first one is due to stray scattering of the CW signal by imperfections in the array as represented by narrow-bandwidth line at 1550.7 nm. The second cross-talk appears because of low finesse noise rejection of the spectrum analyzer – channel from -9 to -16. However, the deflected generated signal and idler can be distinguished from CW signal due to their different spectral widths because of the pulsed nature of the control beam, i.e. they are spectrally wider than the noise due to the CW signal. Scans for specific output channels versus wavelength are shown in Figure 8.5. Spectra of the deflected idler and signal in waveguide 15 are shown in Figure 8.5a for two different control power levels. The results verify the linear dependence of the peak power of the generated idler on the power of injected control pulse (in the low-depletion limit). Because of the duty cycle of the control and the limited suppression of the spectral cross-talk in the spectrum analyzer it was impossible to detect the parametrically amplified signal and idler pulses with a CW detector near guide -13, where both of them spatially overlap the strong CW signal output beam. Hence a lock-in technique was used together with spectral filtering to measure the idler's distribution, as shown in Figure 8.5b.

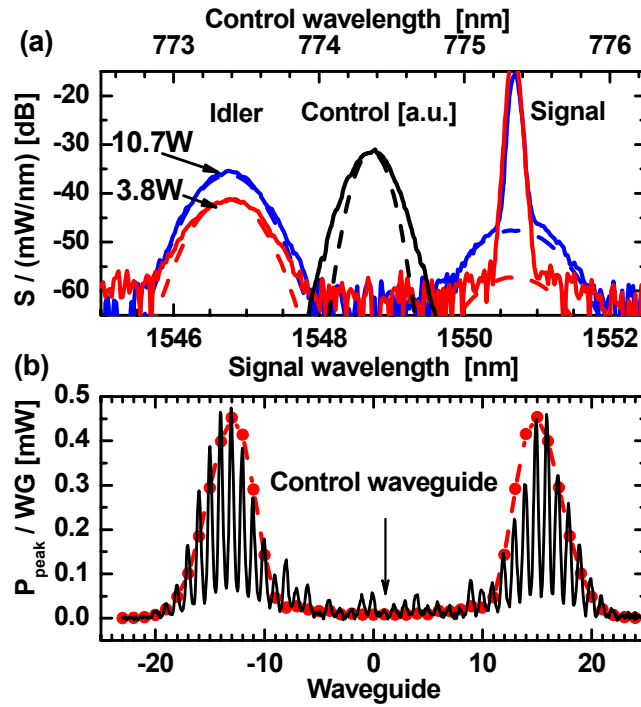


Figure 8.5 a) Output spectral density from waveguide 15 for a control input with $P_{P_{peak}} = 3.8$ (red) and 10.7 W (blue), $P_S = 19$ mW. The control spectrum is also shown (black). b) Peak power of the idler ($\lambda_I = 1546.7$ nm) at the output for $P_{P_{peak}} = 10.7$ W, $P_S = 19$ mW. Dashed lines and circles show theory.

For the maximum available control peak power of $P_{P_{peak}} = 10.7$ W in our experiment, a $P_S = 4$ mW CW input signal (power in the center waveguide of the beam) was converted to idler pulses having $P_{I_{peak}} = 0.45$ mW peak power (in the waveguide at the beam center). Simulations have shown that 38 W of control peak power would yield transparent switching with idler pulses with also 4 mW peak power. For higher control powers the device would provide parametric gain. The all-optical control of the output position and wavelength was also verified. Figure 8.6a shows the spatial output distribution of the idler for four different control beam input channels.

Furthermore, the simultaneous wavelength conversion to the idler, for five different signal wavelengths, is verified in Figure 8.6b with a bandwidth exceeding 10nm.

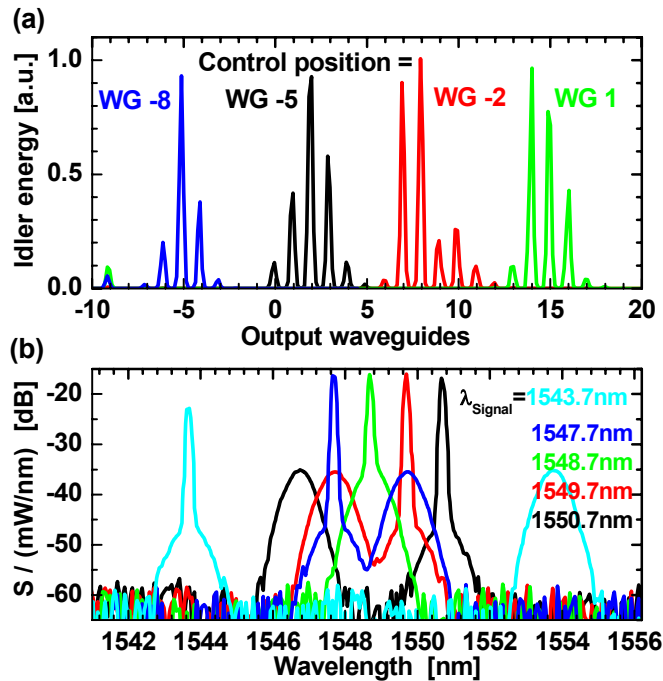


Figure 8.6 a) Spatial output distribution of the deflected idler for different positions of the control beam. b) Spectral density of the deflected signal and idler in waveguide 15 for a number of different signal wavelengths, $P_{peak} = 10.7$ W, $P_s = 19$ mW.

In summary, a powerful concept which can be used to build a versatile transparent device with a complex functionality, based on a quadratically nonlinear waveguide array was demonstrated in this chapter. Ultrafast, phase-insensitive all-optical spatial switching, amplification, and wavelength conversion was implemented in a single device. It can process a milliwatt signal with low cross-talk and negligible pulse distortion at 100 GHz data rate.

CHAPTER NINE: CONCLUSIONS

The common link to all of the experiments presented in this dissertation was titanium indiffused lithium niobate waveguide array samples with tunable cascaded quadratic nonlinearity – the sign and strength of the effective nonlinearity could be adjusted by changing the wavevector mismatch for second harmonic generation. Their realization with state-of-the-art technology resulted in linear (low losses and perfect uniformity) and nonlinear properties which allowed very demanding experiments involving integrating optics structures to be performed.

First of all was the observation of linear discrete Talbot revivals in waveguide arrays. Major differences between continuous systems, where the Talbot self-imaging effect always occurs irrespective of the pattern's period, and discrete configurations, where this process is only possible for a specific set of periodicities $N \in \{1,2,3,4,6\}$, were predicted. It was also observed that the Talbot distance is dependent on the Bloch momentum of the excited beam.

The major part of the dissertation was devoted to the formation of discrete quadratic solitons. Two different confinement cases were investigated. Weakly-localized solitons were excited by the FH beam only. Relatively wide, stable solitons were formed on propagation due to the balance between diffraction and cascading nonlinearity. Staggered and unstaggered solitons were observed for appropriate combinations of the signs of diffraction and nonlinearity (when their product was negative), for complimentary combinations nonlinearly enhanced diffraction occurred. On the other hand, the excitation of strongly-localized solitons required both the FH and SH fields to be launched in-phase. This was a consequence of the reduced degrees of

freedom in quadratic arrays in which the second harmonic field was not coupled between neighboring waveguides. The formation of the solitons for different relative phase differences between the FH and SH was studied and a close relation between the highly-localized solitons and the nonlinear eigenmodes of the single channel was observed.

The natural connection between soliton formation and modulational instability of discrete plane waves was investigated experimentally. Whenever conditions appropriate to the formation of stable solitons occurs, filamentation due to modulational instability was found in arrays with quadratic nonlinearities for a negative product of diffraction and nonlinearity. For a positive product the plane wave propagates in quadratically nonlinear medium without modulational instability, i.e. without beam filamentation.

It is amazing how fast fundamental research can lead to applications these days. The last experiment demonstrated a phase-insensitive, ultrafast, all-optical spatial switching and frequency conversion device based on a quadratically nonlinear waveguide array. Routing of milliwatt signals with wavelengths in the communication band (1550 nm) was achieved without pulse distortions by parametric interaction with a control beam with 10 W power and wavelengths near 775 nm. Numerical simulations confirmed the ultrafast switching capability of the device up to a data rate of 100 GHz.

This thesis by no means exhausts the interesting science that can be performed in such quadratically nonlinear arrays. For example, spatial solitons guided by the interface between a continuous slab waveguide and the discrete array are expected to exist. There has been a great deal of interest in waves guided by an interface due to the existence of nonlinearity have been of interest since the late 1970s. Because of the tenability in the strength and sign of the cascading nonlinearity, a richer variety of such solitons should be present in the PPLN arrays.

Contributions from higher bands of this periodic structure were observed frequently in the experiments discussed here. In principle it should be possible to excite these bands cleanly and study their linear and nonlinear properties. The fields of such higher order bands are no longer centered in the channels and it may be possible to introduce coupling of the second harmonic between channels in this way.

Weakly coupled nonlinear waveguides have proven to be an excellent, controlled way to probe the effects of discreteness in nature and one should expect this field to flourish for years to come.

LIST OF REFERENCES

1. D. K. Campbell, "Fresh breather," *Nature* **432**, 455 (2004).
2. J. Frenkel and T. Kontorova, "On the theory of plastic deformation and twinning," *J. Phys.* **1**, 137 (1939).
3. E. Fermi, J. Pasta and S. Ulam, *Studies of nonlinear problems - Report No. LA1940*, (Los Alamos National Laboratory, Los Alamos, 1955).
4. M. Toda, "Vibration of a chain with nonlinear interaction," *J. Phys. Soc. Jap.* **22**, 431 (1967).
5. M. Toda, "Mechanics and statistical mechanics of nonlinear chains," *J. Phys. Soc. Jap.* **S 26**, 235 (1969).
6. S. Aubry, "Unified approach to interpretation of displacive and order-disorder systems. 2. Displacive systems," *J. Chem. Phys.* **64**, 3392 (1976).
7. A. S. Davydov and N. I. Kislukha, "Solitary excitons in one-dimensional molecular chains," *Physica Status Solidi B* **59**, 465 (1973).
8. M. A. Collins, "Solitons in chemical physics," *Adv. Chem. Phys.* **53**, 225 (1983).
9. M. A. Collins and D. P. Craig, "A model of localization, soliton propagation, and self-trapping in an electronically excited atomic lattices," *Chem. Phys.* **75**, 191 (1983).
10. G. Kopidakis and S. Aubry, "Discrete breathers in realistic models: hydrocarbon structures," *Physica B* **296**, 237 (2001).
11. S. Aubry, G. Kopidakis, A. Morgante and G. Tsironis, "Analytic conditions for targeted energy transfer between nonlinear oscillators or discrete breathers," *Physica B* **296**, 222 (2001).
12. L. Floria, J. Marin, P. Martinez, F. Falo and S. Aubry, "Intrinsic localisation in the dynamics of a Josephson-Junction ladder," *Europhys. Lett.* **36**, 539 (1996).

13. L. Floria, J. Marin, S. Aubry, P. Martinez, F. Falo and J. Mazo, "Josephson-junction ladder: A benchmark for nonlinear concepts," *Physica D* **113**, 387 (1998).
14. A. C. Scott, *Active and Nonlinear Wave Propagation in Electronics*, (Wiley Interscience, New York, 1970).
15. F. K. Abdullaev, B. B. Baizakov, S. A. Darmanyan, V. V. Konotop and M. Salerno, "Nonlinear excitations in arrays of Bose-Einstein condensates," *Phys. Rev. A* **64**, 043606 (2001).
16. A. Trombettoni and A. Smerzi, "Discrete solitons and breathers with dilute Bose-Einstein condensates," *Phys. Rev. Lett.* **86**, 2353 (2001).
17. S. Somekh, E. Garmire, A. Yariv, H. L. Garvin and Hunsperg, "Channel optical waveguide directional couplers," *Appl. Phys. Lett.* **22**, 46 (1973).
18. A. Yariv, Y. Xu, R. Lee and A. Scherer, "Coupled-resonator optical waveguide: a proposal and analysis," *Opt. Lett.* **24**, 711 (1999).
19. E. Yablonovitch, "Inhibited spontaneous emission in solid state physics and electronics," *Phys. Rev. Lett.* **58**, 2059 (1987).
20. A. L. Jones, "Coupling of optical fibers and scattering in fibers," *Journal of the Optical Society of America* **55**, 261 (1965).
21. D. N. Christodoulides and R. I. Joseph, "Discrete self-focusing in nonlinear arrays of coupled waveguides," *Opt. Lett.* **13**, 794 (1988).
22. S. Darmanyan, A. Kobayakov and F. Lederer, "Strongly localized modes in discrete systems with quadratic nonlinearity," *Phys. Rev. E* **57**, 2344 (1998).
23. T. Peschel, U. Peschel and F. Lederer, "Discrete bright solitary waves in quadratically nonlinear media," *Phys. Rev. E* **57**, 1127 (1998).
24. N. K. Efremidis, S. Sears, D. N. Christodoulides, J. W. Fleischer and M. Segev, "Discrete solitons in photorefractive optically induced photonic lattices," *Phys. Rev. E* **66**, art. no. (2002).
25. N. Efremidis and D. Christodoulides, "Discrete Ginzburg-Landau solitons," *Phys. Rev. E* **67**, (2003).
26. E. Ultanir, G. Stegeman and D. Christodoulides, "Dissipative photonic lattice solitons," *Opt. Lett.* **29**, 845 (2004).

27. H. S. Eisenberg, Y. Silberberg, R. Morandotti, A. R. Boyd and J. S. Aitchison, "Discrete spatial optical solitons in waveguide arrays," *Phys. Rev. Lett.* **81**, 3383 (1998).
28. R. Morandotti, H. S. Eisenberg, Y. Silberberg, M. Sorel and J. S. Aitchison, "Self-focusing and defocusing in waveguide arrays," *Phys. Rev. Lett.* **86**, 3296 (2001).
29. J. W. Fleischer, T. Carmon, M. Segev, N. K. Efremidis and D. N. Christodoulides, "Observation of discrete solitons in optically induced real time waveguide arrays," *Phys. Rev. Lett.* **90**, (2003).
30. J. W. Fleischer, M. Segev, N. K. Efremidis and D. N. Christodoulides, "Observation of two-dimensional discrete solitons in optically induced nonlinear photonic lattices," *Nature* **422**, 147 (2003).
31. A. Fratalocchi, G. Assanto, K. Brzdakiewicz and M. Karpierz, "Discrete propagation and spatial solitons in nematic liquid crystals," *Opt. Lett.* **29**, 1530 (2004).
32. R. Iwanow, D. A. May-Arrioja, D. N. Christodoulides, G. I. Stegeman, Y. Min and W. Sohler, "Discrete Talbot effect," submitted to *Physical Review Letters* (2005).
33. R. Iwanow, R. Schiek, G. I. Stegeman, T. Pertsch, F. Lederer, Y. Min and W. Sohler, "Observation of discrete quadratic solitons," *Phys. Rev. Lett.* **93**, 113902 (2004).
34. R. Iwanow, G. Stegeman, R. Schiek, T. Pertsch, F. Lederer, Y. Min and W. Sohler, "Highly localized discrete quadratic solitons," *Opt. Lett.* **30**, (2005).
35. R. Iwanow, R. Schiek, G. I. Stegeman, Y. Min and W. Sohler, "Discrete modulational instability in periodically poled lithium niobate arrays," submitted to *Optics Letters* (2005).
36. T. Pertsch, U. Peschel and F. Lederer, "All-optical switching in quadratically nonlinear waveguide arrays," *Opt. Lett.* **28**, 102 (2003).
37. T. Pertsch, R. Iwanow, R. Schiek, G. Stegeman, U. Peschel, F. Lederer, Y. Min and W. Sohler, "Spatial ultrafast switching and frequency conversion in lithium niobate waveguide arrays," *Opt. Lett.* **30**, 177 (2005).
38. F. A. Hopf and G. I. Stegeman, *Applied Classical Electrodynamics*, (John Wiley & Sons, New York, 1986).
39. R. W. Boyd, *Nonlinear Optics*, (Academic Press, Boston, 1992).

40. J. C. Maxwell, "A dynamical theory of the electromagnetic field," *Phil. Trans. R. Soc. Lon.* **155**, 459 (1865).
41. J. E. Midwinter and J. Warner, "Effects of phase matching method of uniaxial crystal symmetry on polar distribution of second order nonlinear optical polarization," *Brit. J. Appl. Phys.* **16**, 1135 (1965).
42. G. I. Stegeman, M. Sheik-Bahae, E. Van Stryland and G. Assanto, "Large nonlinear phase-shifts in 2nd-order nonlinear optical processes," *Opt. Lett.* **18**, 13 (1993).
43. G. P. Agrawal, *Nonlinear Fiber Optics*, (Academic Press, San Diego, 1995).
44. M. V. Hobden, "Phase matched 2nd harmonic generation in biaxial crystals," *J. Appl. Phys.* **38**, 4365 (1967).
45. J. A. Armstrong, N. Bloembergen, J. Ducuing and P. S. Pershan, "Interaction between light waves in a nonlinear dielectric," *Phys. Rev. A* **127**, 1918 (1962).
46. M. M. Fejer, G. A. Magel, D. H. Jundt and R. L. Byer, "Quasi phase matched 2nd harmonic generation - tuning and tolerances," *IEEE J. Quant. Elect.* **28**, 2631 (1992).
47. K. R. Parameswaran, "Highly efficient optical frequency mixers," (Stanford University, 2002).
48. T. Tamir, *Guided Wave Optoelectronics*, (Springer-Verlag, New York, 1988).
49. A. Yariv, "Coupled mode theory for guided wave optics," *IEEE J. Quant. Elect.* **9**, 919 (1973).
50. E. A. Marcatili, "Dielectric rectangular waveguide and directional coupler for integrated optics," *AT&T Tech. J.* **48**, 2071 (1969).
51. K. Okamoto, *Fundamentals of Optical Waveguides*, (Academic Press, San Diego, 2000).
52. S. M. Jensen, "The nonlinear coherent coupler," *IEEE J. Quant. Elect.* **18**, 1580 (1982).
53. S. Trillo, S. Wabnitz, E. M. Wright and G. I. Stegeman, "Soliton switching in fiber nonlinear directional couplers," *Opt. Lett.* **13**, 672 (1988).
54. S. Trillo and S. Wabnitz, "Nonlinear nonreciprocity in a coherent mismatched directional coupler," *Appl. Phys. Lett.* **49**, 752 (1986).

55. R. Schiek, "All-optical switching in the directional coupler caused by nonlinear refraction due to cascaded 2nd order nonlinearity," *Opt. Quant. Electron.* **26**, 415 (1994).
56. S. R. Friberg, Y. Silberberg, M. K. Oliver, M. J. Andrejco, M. A. Saifi and P. W. Smith, "Ultrafast all-optical switching in a dual-core fiber nonlinear coupler," *Appl. Phys. Lett.* **51**, 1135 (1987).
57. J. Aitchison, A. Villeneuve and G. Stegeman, "Nonlinear directional couplers in AlGaAs," *J. Nonlin. Opt. Phys.* **4**, 871 (1995).
58. R. Schiek, Y. Baek, G. Krijnen, G. I. Stegeman, I. Baumann and W. Sohler, "All-optical switching in lithium niobate directional couplers with cascaded nonlinearity," *Opt. Lett.* **21**, 940 (1996).
59. P. S. Russell, "Optics of Floquet-Bloch waves in dielectric gratings," *Appl. Phys. B* **39**, 231 (1986).
60. D. Mandelik, H. S. Eisenberg, Y. Silberberg, R. Morandotti and J. S. Aitchison, "Band-gap structure of waveguide arrays and excitation of Floquet-Bloch solitons," *Phys. Rev. Lett.* **90**, art. no. (2003).
61. J. Meier, J. Hudock, D. Christodoulides, G. Stegeman, Y. Silberberg, R. Morandotti and J. Aitchison, "Discrete vector solitons in Kerr nonlinear waveguide arrays," *Phys. Rev. Lett.* **91**, (2003).
62. D. Neshev, E. Ostrovskaya, Y. Kivshar and W. Krolikowski, "Spatial solitons in optically induced gratings," *Opt. Lett.* **28**, 710 (2003).
63. A. V. Buryak, P. Di Trapani, D. V. Skryabin and S. Trillo, "Optical solitons due to quadratic nonlinearities: from basic physics to futuristic applications," *Phys. Rep.* **370**, 63 (2002).
64. J. G. Gualtieri, J. A. Kosinski and A. Ballato, "Piezoelectric materials for acoustic-wave applications," *IEEE Trans. Ultrason. Ferroelec. Freq. Cont.* **41**, 53 (1994).
65. E. Wooten, K. Kissa, A. Yi-Yan, E. Murphy, D. Lafaw, P. Hallemeier, D. Maack, D. Attanasio, D. Fritz, G. McBrien and D. Bossi, "A review of lithium niobate modulators for fiber-optic communications systems," *IEEE J. Sel. Top. Quant. Elect.* **6**, 69 (2000).
66. V. G. Dmitriev, G. G. Gurzadyan and D. N. Nikogosyan, *Handbook of Nonlinear Optical Crystals*, 3rd, Springer Series in Optical Sciences (Springer, 1999).

67. R. V. Schmidt and I. P. Kaminow, "Metal diffused optical waveguides in LiNbO₃," *Appl. Phys. Lett.* **25**, 458 (1974).
68. W. K. Burns, P. H. Klein, E. J. West and L. E. Plew, "Ti diffusion in Ti:LiNbO₃ planar and channel optical waveguides," *J. Appl. Phys.* **50**, 6175 (1979).
69. F. Schiller, B. Herreros and G. Lifante, "Optical characterization of vapor Zn-diffused waveguides in lithium niobate," *J. Opt. Soc. Am. A* **14**, 425 (1997).
70. J. L. Jackel, C. E. Rice and J. J. Veselka, "Proton-exchange for high-index waveguides in LiNbO₃," *Appl. Phys. Lett.* **41**, 607 (1982).
71. G. J. Edwards and M. Lawrence, "A temperature-dependent dispersion-equation for congruently grown lithium niobate," *Opt. Quant. Electron.* **16**, 373 (1984).
72. G. P. Bava, I. Montrosset, W. Sohler and H. Suche, "Numerical modeling of Ti:LiNbO₃ integrated optical parametric oscillators," *IEEE J. Quant. Elect.* **23**, 42 (1987).
73. E. Strake, G. P. Bava and I. Montrosset, "Guided modes of Ti:LiNbO₃ channel waveguides - a novel quasi-analytical technique in comparison with the scalar finite element method," *J. Lightwave Technol.* **6**, 1126 (1988).
74. R. Schiek and T. Pertsch, Regensburg (personal communication, 2001).
75. R. Schiek, "QPM gratings for Ti:indiffused LiNbO₃ film waveguides for the experimental investigation of spatial solitons", internal report, (Munich, 2000)
76. R. Schiek, "Diffusionskonstanten in Ti:LiNbO₃", internal report, (Munich, 2001)
77. J. Meier, "Discrete nonlinear wave propagation in Kerr nonlinear media," (University of Central Florida, Orlando, 2004).
78. T. Pertsch, T. Zentgraf, U. Peschel, A. Brauer and F. Lederer, "Anomalous refraction and diffraction in discrete optical systems," *Phys. Rev. Lett.* **88**, art. no. (2002).
79. S. Helmfrid, G. Arvidsson and J. Webjorn, "Influence of various imperfections on the conversion efficiency of 2nd harmonic generation in quasi phase matching lithium niobate waveguides," *J. Opt. Soc. Am. B* **10**, 222 (1993).
80. "Agilent 81480A and Agilent 81680A, 81640A, 81682A, 81642A & 81689A Tunable Laser Module Modules - User's Guide," Agilent Technologies (2001).

81. J. F. Pinto, E. Georgiou and C. R. Pollock, "Stable color center laser in OH⁻ doped NaCl operating in the 1.41 μm to 1.81 μm region," *Opt. Lett.* **11**, 519 (1986).
82. E. Georgiou, J. F. Pinto and C. R. Pollock, "Optical properties and formation of oxygen perturbed F²⁺ color center in NaCl," *Phys. Rev. B* **35**, 7636 (1987).
83. Reviewed in "Color Center Lasers," by C. Pollock in "Encyclopedia of Lasers and Optical Technology", ed. R. A. Meyers, (Academic Press, 1991).
84. P. Maine, D. Strickland, P. Bado, M. Pessot and G. Mourou, "Generation of ultrahigh peak power pulses by chirped pulse amplification," *IEEE J. Quant. Elect.* **24**, 398 (1988).
85. J. Stone and D. Marcuse, "Direct measurement of 2nd order dispersion in short optical fibers using white light interferometry," *Electron. Lett.* **20**, 751 (1984).
86. B. C. Collings, K. Bergman, S. T. Cundiff, S. Tsuda, J. N. Kutz, J. E. Cunningham, W. Y. Jan, M. Koch and W. H. Knox, "Short cavity erbium/ytterbium fiber lasers mode-locked with a saturable Bragg reflector," *IEEE J. Sel. Top. Quant. Elect.* **3**, 1065 (1997).
87. E. B. Treacy, "Optical pulse compression with diffraction gratings," *IEEE J. Quant. Elect.* **QE 5**, 454 (1969).
88. O. E. Martinez, "3000 times grating compressor with positive group velocity dispersion - application to fiber compensation in 1.3-1.6 μm Region," *IEEE J. Quant. Elect.* **23**, 59 (1987).
89. R. Trebino and D. J. Kane, "Using phase retrieval to measure the intensity and phase of ultrashort pulses - frequency resolved optical gating," *J. Opt. Soc. Am. A* **10**, 1101 (1993).
90. K. W. Delong, R. Trebino, J. Hunter and W. E. White, "Frequency resolved optical gating with the use of 2nd harmonic generation," *J. Opt. Soc. Am. B* **11**, 2206 (1994).
91. R. Trebino, *Frequency-Resolved Optical Gating: The Measurement of Ultrashort Laser Pulses*, (Kluwer Academic Publishers, 2000).
92. K. W. Delong and R. Trebino, "Improved ultrashort pulse retrieval algorithm for frequency-resolved optical gating," *J. Opt. Soc. Am. A* **11**, 2429 (1994).
93. K. W. Delong, D. N. Fittinghoff, R. Trebino, B. Kohler and K. Wilson, "Pulse retrieval in frequency-resolved optical gating based on the method of generalized projections," *Opt. Lett.* **19**, 2152 (1994).

94. "Optical parametric oscillator PG501VIR - Technical description & User's manual," Ekspla (2000).
95. "Laser PL2143A - Technical description & User's manual," Ekspla (2000).
96. H. F. Talbot, "Facts related to optical science," *Philos. Mag.* **9**, 401 (1836).
97. L. Rayleigh, "On copying diffraction gratings and on some phenomena connected therewith," *Philos. Mag.* **11**, 196 (1881).
98. J. T. Winthrop and C. R. Worthington, "Theory of Fresnel images I. Plane periodic objects in monochromatic light," *J. Opt. Soc. Am.* **55**, 373 (1965).
99. W. D. Montgomery, "Self imaging objects of infinite aperture," *Journal of the Optical Society of America* **57**, 772 (1967).
100. P. Szwaykowski and V. Arrizon, "Talbot array illuminator with multilevel phase gratings," *Appl. Opt.* **32**, 1109 (1993).
101. M. Berry and S. Klein, "Integer, fractional and fractal Talbot effects," *J. Mod. Opt.* **43**, 2139 (1996).
102. J. Clauser and J. Dowling, "Factoring integers with Young's N-slit interferometer," *Phys. Rev. A* **53**, 4587 (1996).
103. A. W. Lohmann, "An array illuminator based on the Talbot effect," *Optik* **79**, 41 (1988).
104. D. Mehuys, W. Streifer, R. G. Waarts and D. F. Welch, "Modal analysis of linear Talbot cavity semiconductor lasers," *Opt. Lett.* **16**, 823 (1991).
105. T. Jansson and J. Jansson, "Temporal self-imaging effect in single mode fibers," *J. Opt. Soc. Am.* **71**, 1373 (1981).
106. M. S. Chapman, C. R. Ekstrom, T. D. Hammond, J. Schmiedmayer, B. E. Tannian, S. Wehinger and D. E. Pritchard, "Near field imaging of atom diffraction gratings - the atomic Talbot effect," *Phys. Rev. A* **51**, R14 (1995).
107. L. Deng, E. Hagley, J. Denschlag, J. Simsarian, M. Edwards, C. Clark, K. Helmerson, S. Rolston and W. Phillips, "Temporal, matter-wave-dispersion Talbot effect," *Phys. Rev. Lett.* **83**, 5407 (1999).

108. B. Brezger, L. Hackermuller, S. Uttenthaler, J. Petschinka, M. Arndt and A. Zeilinger, "Matter-wave interferometer for large molecules," *Phys. Rev. Lett.* **88**, (2002).
109. R. Robinett, "Quantum wave packet revivals," *Phys. Rep.* **392**, 1 (2004).
110. J. H. Eberly, N. B. Narozhny and J. J. Sanchezmondragon, "Periodic spontaneous collapse and revival in a simple quantum model," *Phys. Rev. Lett.* **44**, 1323 (1980).
111. I. S. Averbukh and N. F. Perelman, "Fractional revivals of wave packets in the course of long term evolution of highly excited quantum systems," *Zhurnal Eksperimentalnoi i Teoreticheskoi Fiziki* **96**, 818 (1989).
112. O. Friesch, I. Marzoli and W. Schleich, "Quantum carpets woven by Wigner functions," *New. J. Phys.* **2**, 1 (2000).
113. R. Morandotti, U. Peschel, J. Aitchison, H. Eisenberg and K. Silberberg, "Experimental observation of linear and nonlinear optical Bloch oscillations," *Phys. Rev. Lett.* **83**, 4756 (1999).
114. T. Pertsch, P. Dannberg, W. Elflein, A. Brauer and F. Lederer, "Optical Bloch oscillations in temperature tuned waveguide arrays," *Phys. Rev. Lett.* **83**, 4752 (1999).
115. Reviewed in "Discrete Solitons," by F. Lederer, S. Darmanyan and A. Kobayakov in "Spatial Optical Solitons", ed. S. Trillo and W. E. Torruellas, (Springer, New York, 2001).
116. W. E. Torruellas, Z. Wang, D. J. Hagan, E. W. Van Stryland, G. I. Stegeman, L. Torner and C. R. Menyuk, "Observation of 2-dimensional spatial solitary waves in a quadratic medium," *Phys. Rev. Lett.* **74**, 5036 (1995).
117. R. Schiek, Y. Baek and G. I. Stegeman, "One-dimensional spatial solitary waves due to cascaded second-order nonlinearities in planar waveguides," *Phys. Rev. E* **53**, 1138 (1996).
118. R. Schiek, R. Iwanow, T. Pertsch, G. I. Stegeman, G. Schreiber and W. Sohler, "One-dimensional spatial soliton families in optimally engineered quasi-phase-matched lithium niobate waveguides," *Opt. Lett.* **29**, 596 (2004).
119. A. Kobayakov and F. Lederer, "Cascading of quadratic nonlinearities: An analytical study," *Phys. Rev. A* **54**, 3455 (1996).

120. G. I. Stegeman, D. J. Hagan and L. Torner, " $\chi^{(2)}$ cascading phenomena and their applications to all-optical signal processing, mode-locking, pulse compression and solitons," *Opt. Quant. Electron.* **28**, 1691 (1996).
121. S. A. Akhmanov and R. V. Khokhlov, *Problems of Nonlinear Optics*, (Gordon and Breach, New York, 1972).
122. A. E. Kaplan, "Eigenmodes of $\chi^{(2)}$ wave mixings - cross-induced 2nd order nonlinear refraction," *Opt. Lett.* **18**, 1223 (1993).
123. N. N. Akhmediev and A. Ankiewicz, *Solitons: Nonlinear Pulses and Beams*, (Chapman and Hall, London, 1997).
124. E. Enfield and G. Rowlands, *Nonlinear Waves, Solitons and Chaos*, (Cambridge University Press, Cambridge, 1990).
125. G. B. Whitham, "Non-linear dispersive waves," *Proc. R. Soc. Lon. Ser. A* **283**, 238 (1965).
126. T. B. Benjamin and J. E. Feir, "Disintegration of wave trains on deep water. 1. Theory," *J. Fluid Mech.* **27**, 417 (1967).
127. T. Taniuti and H. Washimi, "Self-trapping and instability of hydromagnetic waves along magnetic field in a cold plasma," *Phys. Rev. Lett.* **21**, 209 (1968).
128. L. Salasnich, A. Parola and L. Reatto, "Modulational instability and complex dynamics of confined matter-wave solitons," *Phys. Rev. Lett.* **91**, 080405 (2003).
129. A. Hasegawa and W. F. Brinkman, "Tunable coherent IR and FIR sources utilizing modulational instability," *IEEE J. Quant. Elect.* **16**, 694 (1980).
130. R. Fuerst, D. Baboiu, B. Lawrence, W. Torruellas, G. Stegeman, S. Trillo and S. Wabnitz, "Spatial modulational instability and multisoliton-like generation in a quadratically nonlinear optical medium," *Phys. Rev. Lett.* **78**, 2756 (1997).
131. R. Malendevich, L. Jankovic, G. Stegeman and J. S. Aitchison, "Spatial modulation instability in a Kerr slab waveguide," *Opt. Lett.* **26**, 1879 (2001).
132. D. Kip, M. Soljagic, M. Segev, E. Eugenieva and D. Christodoulides, "Modulation instability and pattern formation in spatially incoherent light beams," *Science* **290**, 495 (2000).

133. Y. S. Kivshar and M. Peyrard, "Modulational instabilities in discrete lattices," *Phys. Rev. A* **46**, 3198 (1992).
134. J. Meier, G. Stegeman, D. Christodoulides, Y. Silberberg, R. Morandotti, H. Yang, G. Salamo, M. Sorel and J. Aitchison, "Experimental observation of discrete modulational instability," *Phys. Rev. Lett.* **92**, (2004).
135. Reviewed in "Physics of all-optical switching devices," by G. I. Stegeman and A. Miller in "Photonics in Switching", ed. J. Midwinter, (Academic Press, Orlando, 1993).
136. M. J. Adams, D. A. O. Davies, M. C. Tatham and M. A. Fisher, "Nonlinearities in semiconductor laser amplifiers," *Opt. Quant. Electron.* **27**, 1 (1995).
137. D. Cotter, R. J. Manning, K. J. Blow, A. D. Ellis, A. E. Kelly, D. Nasset, I. D. Phillips, A. J. Poustie and D. C. Rogers, "Nonlinear optics for high-speed digital information processing," *Science* **286**, 1523 (1999).
138. C. Schubert, J. Berger, S. Diez, H. Ehrke, R. Ludwig, U. Feiste, C. Schmidt, H. Weber, G. Toptchiyski, S. Randel and K. Petermann, "Comparison of interferometric all-optical switches for demultiplexing applications in high-speed OTDM systems," *J. Lightwave Technol.* **20**, 618 (2002).
139. A. D'Ottavi, F. Martelli, P. Spano, A. Mecozzi, S. Scotti, R. Dall'Ara, J. Eckner and G. Guekos, "Very high efficiency four-wave mixing in a single semiconductor traveling-wave amplifier," *Appl. Phys. Lett.* **68**, 2186 (1996).
140. M. H. Chou, K. R. Parameswaran, M. M. Fejer and I. Brener, "Multiple-channel wavelength conversion by use of engineered quasi-phase-matching structures in LiNbO₃ waveguides," *Opt. Lett.* **24**, 1157 (1999).
141. G. Schreiber, H. Suche, Y. L. Lee, W. Grundkotter, V. Quiring, R. Ricken and W. Sohler, "Efficient cascaded difference frequency conversion in periodically poled Ti: LiNbO₃ waveguides using pulsed and cw pumping," *Applied Physics B* **73**, 501 (2001).
142. I. Brener, B. Mikkelsen, G. Raybon, R. Harel, K. Parameswaran, J. Kurz and M. Fejer, "160Gbit/s wavelength shifting and phase conjugation using periodically poled LiNbO₃ waveguide parametric converter," *Electron. Lett.* **36**, 1788 (2000).
143. P. Pioger, F. Baronio, V. Couderc, A. Barthelemy, C. De Angelis, Y. Min, V. Quiring and W. Sohler, "Spatial routing at 125 Gbit/s based on noncollinear generation of self-trapped beams in Ti: PPLN film waveguides," *IEEE Phot. Tech. Lett.* **16**, 560 (2004).